Ammonium fluoride: transition metal ion purification

Litha Yapi

April 2017

Ammonium fluoride: transition metal ion purification

A dissertation submitted in partial fulfillment of the degree

Master of Engineering

(Chemical Engineering)

by

Litha Yapi

In the Faculty of Engineering, Built Environment, and Information Technology

University of Pretoria

April 2017

Ammonium fluoride: transition metal ion purification

Student: Litha Yapi

Supervisor: Prof Philip Crouse

Co-supervisor: Dr Salmon Lubbe

Department of Chemical Engineering

Executive Summary

The Pelchem NF_3 plant produces an ammonium acid fluoride waste stream. The material of construction for the piping and stirrer fabrication in the plant is Monel. As a predominantly nickel-copper alloy, with minute quantities of carbon, manganese, silicon, sulfur and iron, these may leach into process fluids involved. The two biggest constituents of Monel contaminate the ammonium acid fluoride waste stream.

Despite being the lesser of the two in terms of the composition of the Monel, copper is higher in concentration than nickel in the waste stream: the solubility of copper (II) cation in ammonium fluoride is higher than that of nickel (II) cation. Additionally, the ammonium acid fluoride is stored in steel barrels because of the relatively high process temperature that preclude the use of polymeric drums. This results in the leaching of iron from the steel drum to the solution.

Pelchem expressed an interest in a suitable method of purification of ammonium fluoride, with specific interest of removing nickel (II) cation, copper (II) cation as well as iron (II) cation. The constraints to consider when selecting the appropriate methods are operating costs as well as the capital costs, but the most important factor to consider is the effectiveness of the method in removing the contaminant. In this regard, cationic exchange resins are very suitable, and they are very practical for industrial applications.

In its simplest form, ammonium fluoride solutions are prepared by bubbling ammonia gas through solutions of hydrofluoric acid. Quite a few interesting uses of ammonium fluoride are available, these include as a chemical modifier in lead analysis, synthesis of beta zeolites, etc. The most prominent use is as a technical grade etchant in the electronics industry.

The main aim of this research was to investigate ion exchange as a method of removing contaminants from Pelchem ammonium acid fluoride. Static equilibrium/selectivity experiments reveal that Purolite S930 Plus and Lewatit TP207 show a great affinity for the copper cation. For the limiting step of the reaction, the analysis includes apparent kinetics modelling contrasted with mass transfer modelling. In the case of reaction kinetics, Arrhenius and Van't hoff equations were used to determine reaction parameters: the activation energies are 14 368 $J \cdot mol^{-1}$ and 24 116 $J \cdot mol^{-1}$, for Purolite and Lewatit respectively. The pre-exponential constants are 2 213 and 269 682 $L^2 \cdot min^{-1} \cdot mol^{-2}$ for Purolite and Lewatit in that order.

The heats of reaction are -26 555 and -4 696 $J \cdot mol^{-1}$ for Purolite and Lewatit respectively. Whilst the equilibrium pre-exponential constants are 75 057and 150 for Purolite and Lewatit respectively. Diffusivities for the two resins were found to be in reasonable agreement with those recorded in literature. They follow a temperature dependency trajectory. Weisz-Prater analysis of the observed reaction rate and the diffusion rate, in the two resins, reveals that intraparticle diffusion is the limiting step in the reaction.

Breakthrough curve modelling is only possible with a high degree of empiricism. Treating breakthrough curves as a characteristic concentration profile in the cases where mass transfer limitations are eliminated, is a more fruitful exercise. In the case of the Lewatit resin, it takes 13 hours per litre of resin, to reach breakthrough if the flowrate is 5 Bed Volumes/hour (BV/hr) and the concentration is 370 ppm of the cations in the ammonium fluoride.

The average contaminant load on the ammonium acid fluoride from the Pelchem NF_3 process, is 197 ppm Fe^{2+}(aq), 5 422 ppm Ni^{2+}(aq) and 5 835 ppm Cu^{2+}(aq). Ammonia is quite effective in reducing these cations in solution. In fact, when the acid fluoride is neutralised, only trace quantities of the metal cations remain. The precipitate formed

is predominantly ammonium bifluoride, together with a copper-nickel fluoride hydrate type of compound.

For the NF_3 process, the neutralisation reaction of the acid fluoride is a violently exothermic process. To reduce the heat output, cold shots of ammonia gas ought to be used rather than charging all the ammonia at once. Moreover, the storage of the acid fluoride in steel drums, is to be avoided as the $Fe^{2+}(aq)$ cannot be completely removed by the resins. Instead, a continuous neutralisation process is proposed.

For the separation of the ammonium bifluoride solid from the metal fluoride salts precipitated on neutralisation of the acid fluoride, a spiral concentrator such as Humphrey's spiral concentrator is suggested. In this regard, use of the neutralised ammonium fluoride solution as conduit for the solids on concentrator, is an option worth considering due to its convenience.

Lewatit TP207 is the obvious resin of choice in the purification of the remnant trace metal cation contaminants. The regeneration step can be combined with the backwash step and be treated as a fluidisation process, with hydrogen chloride gas as the fluid of choice. This simplification may decrease the maintenance time significantly, and improve bed throughput.

Acknowledgements

Contents

List of tables

List of figures

xiii

Nomenclature

$[\ ]$	Concentration	mol·L^{-1}
A_C	Cross-sectional area	m^2
Ar	Archimedes number	
C_{wp}	Weisz-Prater criterion	
D	Diffusivity	$\text{m}^2\text{·min}^{-1}$
D_t	Diameter of fluidisation tank	m
d_b	Bubble diameter	m
dp	Particle diameter	m
E	Activation energy	J·mol^{-1}
F_T	Total volumetric flowrate	$\text{m}^3\text{·s}^{-1}$
G_{corr}	Breakthrough curve empirical parameter	$\text{mol}^3\text{·m}^{-5}\text{·s}^{-1}$
H	Heat of	J·mol^{-1}
h	Height	m
h_s	Suspended height of resin	m

k'	Reaction rate constant	$L^3 \cdot min^{-1} \cdot mol^{-3}$
K	Selectivity coefficient	
K_{equil}, K_{eq}	Thermodynamic equilibrium constant	
MM	Molar mass	$g \cdot mol^{-1}$
N	Number of moles	mol
r_i	Outside radius of a spherical pellet	m
R	Ideal gas constant	$8.314 J \cdot mol^{-1} \cdot K^{-1}$
Re	Reynolds number	
t	Time elapsed	min
T	Temperature	K
x	Conversion	
U	Velocity	$m \cdot s^{-1}$
V	Volume of solution	L
z	Axial displacement	m

Greek Letters

ε	Porosity	
ε_s	Porosity at suspended bed	
p	Density	$g \cdot mL^{-1}$

xv

ν	Valency coordinate of ion	
μ	Viscosity	$kg \cdot m^{-1} \cdot s^{-1}$
$\acute{y}$	Activity coefficients	

Miscellaneous Symbols

R-2COOH	Carboxylic functional groups attached to resin matrix
$R\text{-}CuCOO_2$	Resin contaminated with copper cation
$R\text{-}(COO)_2^- M^{2+}$	Resin contaminated with a divalent metal catio

Subscripts

avg	average
B	bulk
e	equilibrium
eff	effective
f	fluid
I	Surface of ion exchanger
m, max	maximum
mf	Minimum fluidisation
o	Initial(ly)
R, r	Resin
rx	reaction
s	In resin, solid

sol	solution

Superscript(s)

*	In equilibrium with bulk solution

1 Introduction

In the early 2000s, Pelchem constructed and commissioned a nitrogen trifluoride plant (NF_3) in a joint venture initiative with BOC Edwards. At the time, global demand for NF_3 necessitated the venture. NF_3 is pivotal in the fabrication of semiconductors as well as liquid crystal displays (LCD), amongst other applications, reacting in the presence of hydrogen to produce an active radical.

$$NF_3 + H \rightarrow NHF_3 \rightarrow F^* + NHF_2 \qquad (1.1)$$
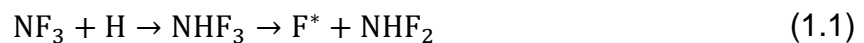
NF_3 is used as a fluorine source for plasma assisted etching of silicon wafers: It is preferred rather than perfluorocarbon gases such as carbon tetrafluoride (CF_4). This is due to its superior etch performance. Furthermore, NF_3 does not lead to the build-up of carbonaceous residues (Branken *et al*, 2014).

In the Pelchem process, ammonium bifluoride salt ($NH_4F.HF$) reacts with fluorine gas to produce NF_3 with other by-products such as nitrous oxide, nitrogen, etc. Prior to the reaction proceeding, anhydrous hydrogen fluoride is added to the ammonium bifluoride to reduce the melting temperature to reasonable levels; the melting point of the salt in the inventory decreases from 700 ºC to 130 ºC. The reactor load comprises of 800 kg ammonium bifluoride salts and 220 kg of HF. Figure 1.1 displays a simplified representation of the NF_3 process.

HF is also produced as a bi-product of the ammonium bifluoride / F_2 reaction. Ammonia gas is used to neutralise and reduce the HF content in the mixture:

$$NH_3 + HF \rightarrow NH_4F \qquad (1.2)$$

This allows the process to be operated in a continuous manner rather than batch or semi-batch. However, the reactants are not charged in stoichiometrically correct ratios, hence an ammonium acid fluoride ($NH_4F.xHF$) by-product is formed. In the general formula $NH_4F.xHF$, x is the acid number, and it typically varies between 0 and 6. In the case of the Pelchem NF_3 process, neutralisation with ammonia can reduce it to 1.5 (see Figure 1.1). The ammonium acid fluoride produced as a waste stream in the NF_3 process is contaminated with material of construction metal cations. Monel is the

material of construction and therefore the cations of interest are copper (Cu^{2+}) and nickel (Ni^{2+}). Additionally, the ammonium acid fluoride waste is stored in steel drums, unfortunately iron (Fe^{2+}) cations leach onto the solution.
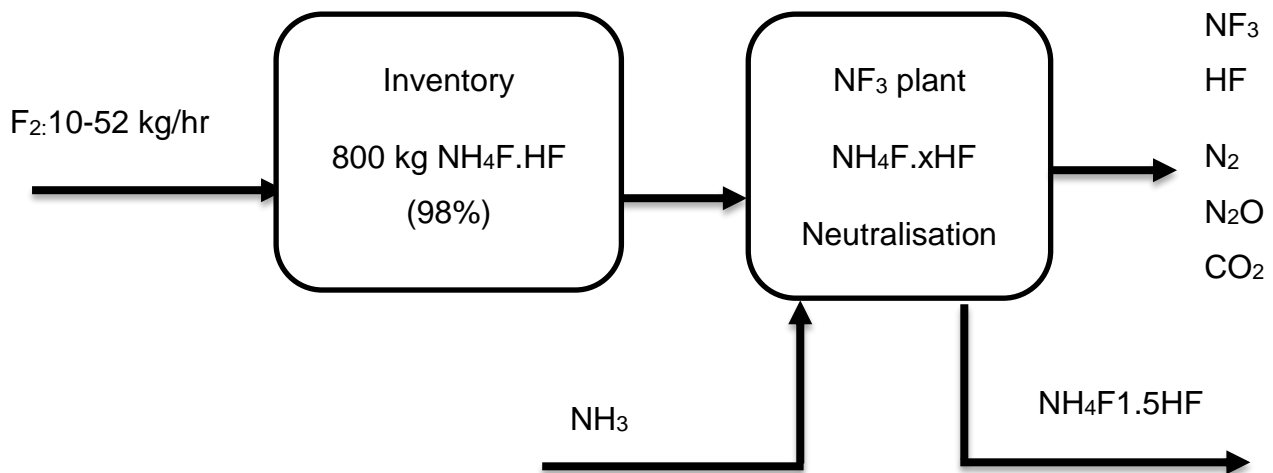
Figure 1.1: An overview of the reactants and products of the NF_3 Process at Pelchem. The inventory of salts to produce NF_3 is 5.5 tons.

Currently the ammonium acid fluoride is disposed of by taking it to a landfill site in drums, crushing the drums and associated content, adding lime to neutralise the HF content. This is deemed to be relatively environmentally benign. The disposal cost of this is in the order of R10/kg $NH_4F.xHF$. Given that the selling price of NF_3 is now the 10th of what it was 10 years ago at around \$21/kg, necessitates that the plant be operated in a way that will reduce costs. This includes the disposal costs of ammonium acid fluoride.

The purpose of this project is to investigate a viable method to purify ammonium acid fluoride ($NH_4F1.5HF$) effluent waste stream of the NF_3 plant at Pelchem. Electronic grade ammonium fluoride is a commodity in high demand in the electronics industry; at the very least, the method to achieve sub-ppm pure 40% ammonium fluoride solution is sought in the project.

Synthetic solutions of ammonium fluoride were prepared by neutralising solutions of ammonium bifluoride with ammonia water solutions. The solutions are spiked with copper cations in the form of copper chloride. Due to the low solubility of nickel cation

in ammonium fluoride solution, only copper cation was used in the synthetic solutions experiments.

The efficiency of the weak acid ion exchange resins in purifying ammonium fluoride is determined experimentally in a laboratory scale investigation. The industrial applicability of the methods of purification was borne in mind and a brief unit operation design was conducted for the industrial process.

2 Literature

2.1 Preparation of ammonium fluoride (Zhan & Zhou, 2012)

The conventional method of ammonium fluoride synthesis involves reacting hydrofluoric acid with ammonia solution. The product is then separated from the reactants by cooling it below its point of crystallization, then drying the resulting mixture. The disadvantages of this system are that it is cumbersome, as it features long production cycle times and is labour as well as energy intensive. In addition, the ammonium fluoride produced is prone to the presence of metal ion impurities: both principal reactants are usually industrial grade and they contain significant quantities of water. As a universal solvent, water will invariably contain metal ion contaminants.

An alternative to the method discussed above, is to use ammonia gas with cold hydrofluoric acid at temperatures of approximately 10 $^{\circ}$C, as reactants. The reaction is represented by

$$NH_3(g) + HF(aq) \rightarrow NH_4F(aq) \tag{2.1}$$
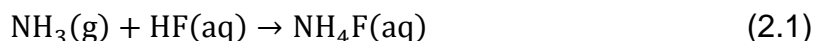
This reaction scheme is less likely to result in a product laden with metal cation contaminants, because in one of the reagents, the presence of water is reduced significantly. The various methods through which ammonium fluoride can be produced will now be discussed. A qualitative feasibility evaluation will then be done with regard to the various methods.

2.1.1 Purified ammonia with HF method (Zhan & Zhou, 2012)

In this method, industrial grade ammonia liquid is used. The ammonia is heated to the gas phase. Subsequently, the organic gas impurities, such as 3 benzyl-6-carboxymethyl 2, 5-diketopierazine, in the ammonia gas are removed using activated charcoal. The oxygen is removed with a deoxidiser resulting in the production of high-purity ammonia gas. This may be reacted with highly pure HF in an exothermic reaction to form electronic grade aqueous ammonium fluoride solution in a similar fashion indicated by equation (2.1).

Since the ammonia is in the vapour phase, it is more practical that it is the limiting reagent and hence easier to control the extent as well as the heat of reaction. This is notwithstanding the fact that HF is a more hazardous chemical to handle. The conversion of ammonia to ammonium fluoride is 100 %. The ammonium fluoride must be separated rapidly from the excess HF, since HF when in the vapour state, may react with NH_4F to form ammonium bifluoride ($NH_4F.HF$).

It is claimed that given the relative simplicity of their invention, it can be tailored for large scale continuous industrial production. Moreover, ammonium fluoride is hygroscopic, it is therefore difficult to maintain its purity if it is in the solid state. This method allows for the direct preparation in the aqueous phase rather than the solid state.

The following temperature and pressure changes occur in this method: industrial ammonia is heated at atmospheric pressure and 50 °C. This results in the release of ammonia gas which is then passed through activated charcoal at pressures between 0.1 and 0.15 MPa to remove the organic impurities. HF at atmospheric pressure and room temperature is then contacted with the ammonia (see equation (2.1)). Given the relatively mild temperatures and pressures and its simplicity, the method is feasible.

2.1.2 Preparation from silicon tetrafluoride gas (SiF_4)

This method involves the use of high purity ammonia and silicon tetrafluoride containing gas. The silicon tetrafluoride containing gas is obtained from the acidulation of phosphorous containing rocks. The gas may be absorbed in water to form fluorosilicic acid (H_2SiF_6). The resulting acid is reacted with ammonia to form an ammonium fluorosilicate solution, from which ammonium fluorosilicate solid (($NH_4)_2SiF_6$) is precipitated. The solid is then purified by recrystallization. Silica is crystallized out, thereby separating ammonium fluoride and silica (Chieng, 1993). The reactions that occur are:

$$3SiF_4 + 2H_2O \rightarrow 2H_2SiF_6 + SiO_2 \qquad (2.2)$$

$$H_2SiF_6 + 2NH_3 \rightarrow (NH_4)_2SiF_6 \qquad (2.3)$$

$$(NH_4)_2SiF_6 + 4NH_3 + 2H_2O \rightarrow SiO_2 + 6NH_4F \qquad (2.4)$$
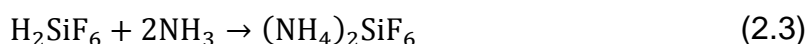
In this method, the purity of ammonium fluorosilicate is of utmost importance. Reaction (2.2) occurs at room temperature and atmospheric pressure. Reaction (2.3) occurs at atmospheric pressure and a temperature of 60 $^{\circ}$C. As illustrated with equation (2.4), the ammonium fluorosilicate is ammoniated in the presence of moisture to form highly pure silica (SiO_2) and ammonium fluoride (Chieng, 1993; Schneider *et al*, 1976).

The method lends itself to many reactions, with an all-important need for purity of the reagents. It is practically cumbersome and will have high operational costs as well as capital costs. It may only be feasible if silica production is of economic interest. However, for the sole production of ammonium fluoride, this method is not ideal, as a significant portion of the reactants is converted to a potentially useless silicon dioxide by-product.

2.1.3 Preparation of ammonium fluoride from sodium fluorosilicate

The reaction of fluorosolicic acid waste with phosphoric acid (H_3PO_4) as a catalyst, and sodium salts (such as NaCl, NaOH etc) forms sodium fluorosilicate (Na_2SiF_6) which may be reacted with ammonia. This results in a solution which is a mixture of NH_4F and other products. NH_4F can be separated using conventional separation techniques (Gutierrez, 1983).

For the batch preparation, the sodium fluorosilicate is charged into a reactor. The ammonia is then added as either a gas or an aqueous solution in stoichiometrically correct ratio to the sodium fluorosilicate. The resulting mixture is agitated at 80 $^{\circ}$C for a minimum of 15 minutes and a maximum of 120 minutes (Gutierrez, 1983).

This method has the same disadvantages as the method discussed in section 2.1.2 of this text; it is cumbersome and is overly dependent on the purity of sodium fluorosilicate. It is therefore equally infeasible as the previous method.

2.2 Uses of ammonium fluoride

Ammonium fluoride offers many diverse applications in the processing industry like etching of silicates, mothproofing agent in wood, the printing and dying of textiles. Some of the more interesting application are discussed.

2.2.1 Ammonium fluoride as a chemical modifier in lead analysis

Graphite furnace atomic absorption spectroscopy (GFAAS) is an analytical technique mostly used for samples that contain metal ions that are possible to vaporise. Before the samples are loaded, they are dissolved in acidic aqueous solutions which aid in the digestion thereof.

The fundamental difference between graphite furnace atomic absorption and flame atomic absorption, is that instead of the presence of a nebuliser for the uptake of the sample, an L'vov platform is used inside a graphite tube in the furnace. In the case of flame atomizers, the aerosol formed by the flow of the oxidant, is mixed with the fuel and all but the very fine solution droplets are removed to the waste containers (Skoog, Holler & Nieman, 1998:209). Up to 90% of the original sample is discarded in this manner.

A crucial disadvantage of flame atomizers is that they feature relatively poor sampling efficiency and thus, relatively retarded sensitivity. This is not only due to the significant wastage of the original sample in flame atomization, but also the comparatively very small residence time (approx. 10^{-4} seconds) of the individual atoms. In the case of electrothermal atomizers such as GFAAS, the entire sample is atomised in a short period of time and the residence time of the atoms in the optical path is at least a second long. This leads to greater sensitivity compared to flame atomization (Skoog *et al,* 1998:210).

Interference, whether it be spectral, matrix or both, results in an inaccurate reading in any spectroscopic technique. In the case of lead (Pb) in a high salinity matrix, particularly a magnesium chloride ($MgCl_2$) matrix, this is more pronounced. Spectral interferences are a result of molecular absorption of the salt in the ultra violet (UV) range or even the light scattering. On the other hand, matrix interferences can be a result of the formation of halides (Husa'kova' *et al*, 2007).

In the presence of a halide salt matrix, the atomic absorption signal of the evolved species is very likely to be blighted by insufficient dissociation in the gas phase. The changes of the vaporization traits at elevated heating rates due to the matrix can only be corrected by a fast-instrumental response, which is not usually possible with most

commercially available atomic absorption spectroscopic apparatus (Kantor *et al,* 1983).

In the case of $MgCl_2$ analysis, its hydrolysis and release of hydrochloric acid (HCl) on the decomposition of MgOHCl is inferred:

$$MgCl_2 . H_2O \xrightarrow{\Delta} MgOHCl + HCl \rightarrow MgO + 2HCl \qquad (2.5)$$
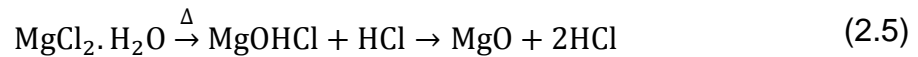
The conventional approach in resolving these problems is time-consuming methods such as pre-concentration and the use of separation techniques.

An alternative analytical method is the use of chemical modifiers. Husa'kova' *et al* (2007) posit that ammonium fluoride is very effective in the elimination of $MgCl_2$ interference on Pb analysis. It also shows superior qualities to the more frequently used chemical modifiers such as nitric acid (HNO_3), ammonium nitrate (NH_4NO_3), etc.

In the case of NH_4F, as with HF, the chloride matrix is converted to a fluoride matrix. Additionally, the presence of NH_4F results in the formation of magnesium fluoride (MgF_2), which is insoluble, and thus will be non-interfering. Factors such as the volatility of a compound play a role; HNO_3 shows less efficacy potential than NH_4NO_3 as it is evaporated and lost too early during the drying step due to its high volatility. On the contrary, NH_4NO_3 is merely converted to NH_4Cl in the drying step. The difference in efficiency between HF and NH_4F is also attributable to the fact that HF is more volatile than NH_4F. Furthermore, HF is a more dangerous substance to handle (Husa'kova' *et al*, 2007).

The use of NH_4F as a chemical modifier is a quick and elegant solution to the matrix interference problem of $MgCl_2$ in Pb solution analysis with GFAAS in comparison to the time-intensive methods like separation techniques. It is imperative that the NH_4F is highly pure to avoid contamination (Husa'kova' *et al*, 2007).

2.2.2 Synthesis of beta zeolite with ammonium fluoride (Jon *et al,* 2005)

Due to its high thermal and chemical stability, Beta (BEA) zeolite is of considerable industrial importance. Zeolite synthesis in fluoride environment results in larger crystals compared to the hydroxyl environment. This is attributed to the mineralisation

power of F$^-$ versus OH$^-$. HF has been used despite the unwieldy safety and health precautions associated with its handling. Ammonium fluoride is a relatively safe alternative to HF in terms of being a source of F$^-$.

The process of synthesis of the zeolite involves microwave irradiation under basic conditions. It has been posited that pure silica BEA zeolite is not possible to produce from a starting gel not containing an aluminium (Al) source. This is not the case when NH$_4$F is part of the synthesis gel. One can therefore conclude that the addition of NH$_4$F plays a vital role in the synthesis of BEA zeolite.

The crystallinity of BEA zeolite prepared in the presence of NH$_4$F is higher than the crystallinity of BEA zeolite prepared in its absence. This is indicative of the thermal stability: the higher the crystallinity, the higher mechanical stability at a variety of temperatures. A contributing factor may be that high silica zeolites synthesized in a fluoride environment, tend to have substantially fewer defects compared with those obtained via the hydroxyl synthesis route. Moreover, the addition of sodium hydroxide has a minute contribution to the thermal stability of the zeolite.

2.2.3 Ammonium fluoride as etchant

Silicon is not just a good semiconductor; it also possesses excellent mechanical properties. This is exploited in the field of silicon micromachining. The most prominent use of silicon etching, has been within the semiconductor industry. Dry etching or plasma assisted etching of silicon makes use of perfluorinated gases such as carbon tetrafluoride (CF$_4$), hexafluoroethane (C$_2$F$_6$), pefluoropropane (C$_3$F$_8$), sulphur hexafluoride (SF$_6$), and many more (Ohji & French, 1999).

In this process, the active fluorine atom (because of a plasma process wherein the source gases are ionised in radio frequency excitation) reacts with the silicon wafer:

$$4F^* + Si \rightarrow SiF_4 \uparrow \qquad\qquad (2.6)$$
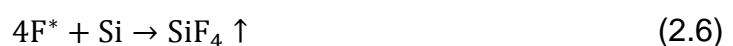
The reaction product must be volatile, to be carried away from the reaction site and therefore allow for etching to continue. Otherwise etching ceases, for an example fluorine cannot be used in the etching of aluminium because the reaction product (AlF$_3$) is not volatile (Saito *et al*, 2003).

NH$_4$F|9

Sometimes the etching of the silicon oxide layer is desired rather than the actual silicon. In which case, the perfluorinated gas is used in conjunction with hydrogen (H_2) to produce active carbon trifluoride which selectively etches SiO_2:

$$CF_4 + H_2 \rightleftharpoons CF_3^* + HF \qquad (2.7)$$

Wet chemical etching is also possible. Silicon dioxide can be etched with dilute hydrogen fluoride (HF) solutions. Or more often, a buffered HF solution with a measured quantity of ammonium fluoride (NH_4F) and HF:

$$SiO_2 + 6HF/NH_4F \rightarrow H_2SiF_6 + 2H_2O \qquad (2.8)$$
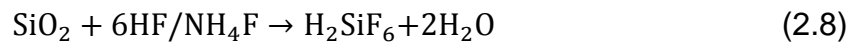
This result in a controlled etch rate. Anisotropic etching of silicon with solutions of NH_4F, is widely used in bulk technique for the manufacturing of Micro Electro Mechanical Systems (MEMS). It is imperative that the buffered solutions are very pure. The NH_4F must be of a technical grade to be effective in this application. Analogous to dry etching, the product of etching must be soluble to be removed from the reaction site (Shah *et al*, 2011).

In some applications, chemical etching is carried out only using ammonium fluoride. During the fabrication of porous silicon, which has applications in micromachining and micro devices, the use of hydrogen fluoride is inappropriate. This is due to the attack of hydrogen ions on the aluminium interconnect layer during the chemical etching. Ammonium fluoride is used as an etchant instead because it has a dramatically lower etch rate of aluminium compared to HF (Ohji & French, 1999).

2.3 Treatment of fluoride effluent streams (precipitation)

Human civilisation is completely dependent on the availability of all forms of water; cooling water for process engineering applications, steam for the running of turbines in electricity generation, drinking water etc. In the case of water for human consumption and hygiene purposes, effective and efficient methods for waste water treatment, such as the removal of heavy metal cations are necessary. Heavy metals tend to be non-biodegradable. Various physico-chemical treatment techniques for water laden with heavy metals have been developed over the years. These tend to be generic in nature, allowing for tailoring to solutions other than water.

The appropriate physico-chemical method to use for purification of a given solution is influenced by several considerations. These include operating conditions such as pH, dose required and initial metal concentration, amongst others. For high concentrations of metal contaminants, in the range of 1000 ppm, lime precipitations are effective. In the case of lower to intermediate concentrations of around 250 ppm, reverse osmosis is the method of choice. Ion exchange is very effective for low contaminant concentrations of less than 100 ppm. The overall cost of treatment of metal contaminated solution is heavily influenced by the process used. Technical applicability, plant feasibility as well as cost implications are some of the factors to consider when choosing an appropriate treatment process or processes (Kurniawan *et al*, 2006).

The justification for heavy metal removal in water waste streams is the need to reduce toxicity. In the field of water treatment, ion exchange resins have the advantage over traditional chemical treatment as well as new technologies such as carbon nanotubes, in that they do not result in residual deposition of chemicals which may have adverse effects on human health (Simate *et al,* 2012).

Small quantities of fluoride are beneficial for strong teeth and bones in humans. Excessive quantities however, lead to dental and skeletal fluorosis. Hence, the reduction/prevention of fluoride contamination of the environment is crucial. Limestone treatment is a popular technique for the treatment of fluoride. In which case, the fluoride is removed via the precipitation of fluorspar (CaF_2) by Ca^{2+} ions formed through the dissolution of limestone. This however, suffers from fundamental inefficiencies: high residual ions needing post treatment, result. Furthermore, defluoridation by crystallization of CaF_2 using calcium salts is limited by its solubility product. Therefore, better methods of dealing with waste fluoride are needed (Gogoi *et al*, 2015).

Heavy metals like Cu, Ni, etc, tend to be highly soluble in aquatic environments: they are prone to accumulate in the food chain. In humans, they may cause serious health disorders if ingested above allowable levels. In the case of ammonium acid fluoride, the justification for the removal of the heavy metal cations is not only for the health benefit but also financial gain: highly pure ammonium fluoride has economic value.

NH_4F|11

There are various physico-chemical treatment processes that can be used to remove heavy metals from waste streams. These include chemical precipitation, coagulation-flocculation, flotation, ion exchange, membrane filtration, etc. Ion exchange and membrane filtration are popular in treatment of waste streams.

Electrotreatment methods such as electrodialysis, membrane electrolysis as well as electrochemical precipitation have many beneficial aspects that contribute to environmental protection. They tend to result in prohibitively high operational costs due to high energy consumption. The constraints that a technique should fall within are

- suitability,
- applicability to local conditions,
- but more crucially, it should achieve purity that is below the maximum contaminant standards legislated by government (Kurniawan *et al,* 2006).

Precipitation or crystallization has been practised for millennia of years. It can be used in situations where the resulting solid is a desired product or the mother liquor is the desired product. In the case of ammonium fluoride purification, the precipitate is the impurity. Often crystallization in inorganic chemicals is effected through the cooling of a liquid stream 1 or 2 ^{o}C below the melting point of the product/impurity desired in the solid phase (Seider, Seader & Lewin, 2004:177).

In the case of ammonium fluoride solutions, the solubilities of the cationic impurities do not change significantly with changing temperature, and crystallisation by evaporation is not appropriate. This is because the decomposition temperature of ammonium fluoride is very close to the boiling point of water. Crystallization by neutralisation is the only reasonable option.

The electronic industry demands high purity electronic grade chemicals. Defects generated in wafers due to the presence of impurities lead to the requirements for minimal impurity content of materials. It is generally accepted that the origin of impurities is from the atmosphere of the manufacturing process, from the materials themselves and/or the leaching of the materials of construction in the equipment, pipes etc. Devices such as chips are manufactured with the aid of materials such hydrogen

fluoride and hence the impurities in such solutions may result in device failure (Fernández-Olmo, Fernández & Irabien, 2007).

Inorganic precipitates in the ammonium acid fluoride liquid streams are likely to contain divalent cations complexes. This is due to the presence of the fluoride ion as the predominant anion in the matrix. For instance, when an ammonium acid fluoride solution contaminated with materials of construction of Monel, is neutralised, a nickel-copper-iron fluoride type precipitate is likely to form.

2.4 Ion exchange terminology (Harland, 1994:32; Helffrerich, 1962:72)

- **Ion Exchange:** Exchange of equivalent numbers of ions with the same charges between the mobile phase and the stationary phase
- **Cationic Exchanger:** When the stationary phase contains positive functional groups
- **Anionic Exchanger:** When the stationary phase contains negative functional groups
- **Ion Exchange Resins:** Cross-linked polymers with charged functional groups capable of facilitating ion exchange.
- **Chelating Resins:** Ion exchange resins capable of forming co-ordination complexes with heavy metals. Electron donating ligands in the resins, are crucial in this
- **Ionogenic groups:** Functional groups within the exchanger framework that are charged. Essentially, the fixed charges within a matrix is a result of these groups
- **Co-ions:** Mobile ions sharing the same charges as the macromolecular exchanger framework's fixed charges
- **Counter-ions**: Ionic species with a charge sign contrasting that of the exchanger framework
- **Capacity**: Also, known as Ion Exchange Capacity, or Maximum Capacity. This is the objective number of exchangeable ionic species in each amount of resin. The ionic species may or not be readily exchangeable. This is dependent on

factors such as the degree of ionisation of the counter ions i.e. RCOONa vs RCOO$^-$Na$^+$.

> **Scientific Weight Capacity**: When the capacity is quoted in units such as *meq/g dry H*$^+$ for cationic exchangers and and/ or meq/g Cl$^-$ form for anionic exchangers

> **Technical Volume Capacity**: Capacity defined in units of *eq/L packed bed in H*$^+$ *or Cl*$^-$ in moist form.

> **Apparent Capacity or Effective Capacity:** The useful capacity of the resin at a specific temperature, concentration etc. When ionogenic groups are ionised, they may act as fixed charges that ought to be balanced by counter-ions. When they are not ionised, this does not apply. It therefore stands to reason that ionogenic groups that tend to be less readily ionisable, have lower effective capacities than their respective maximum capacities. For instance, strong acid resins tend to have higher capacity at wider ranges of pH than weak acid resins. This is because strong acid resins have functional groups that are fully ionised on all pHs, meanwhile weak acid resins have optimum pHs where they may be fully ionised

> **Sorption Capacity:** When the take-up of ions in the resin is attributed to sorption rather than classical ion exchange.

> **Breakthrough Capacity** is the capacity achieved in column operations, typically it is quantified as 80% of the actual breakthrough of cations. The presence of fixed ionic groups in resins, plays an important role in terms of electro-neutrality (by balancing the counter-ions**)**

2.5 Overview of ion exchange

Ion exchange resins are typically insoluble solid structures containing exchangeable ionic species. The exchange occurs when an electrolytic solution is in contact with the ion exchange agent, a stoichiometric number of ions similar in charge in the electrolytic solution are exchanged with ions in the exchange agent. This happens in a chemically equivalent and reversible manner and ensures electro-neutrality. In a nutshell, ion exchange may be represented by Figure 2.1. For ion exchange to be successful, the resin or solid phase must be insoluble on the electrolyte that it will

be used to purify. Hence, if a polymeric resin is used, it should be a cross-linked network polymer (Harland, 1994:2).

Initial State   Equilibrium

(A) (B)   Counter-ions

⊖   Co-ions

Matrix with fixed charges
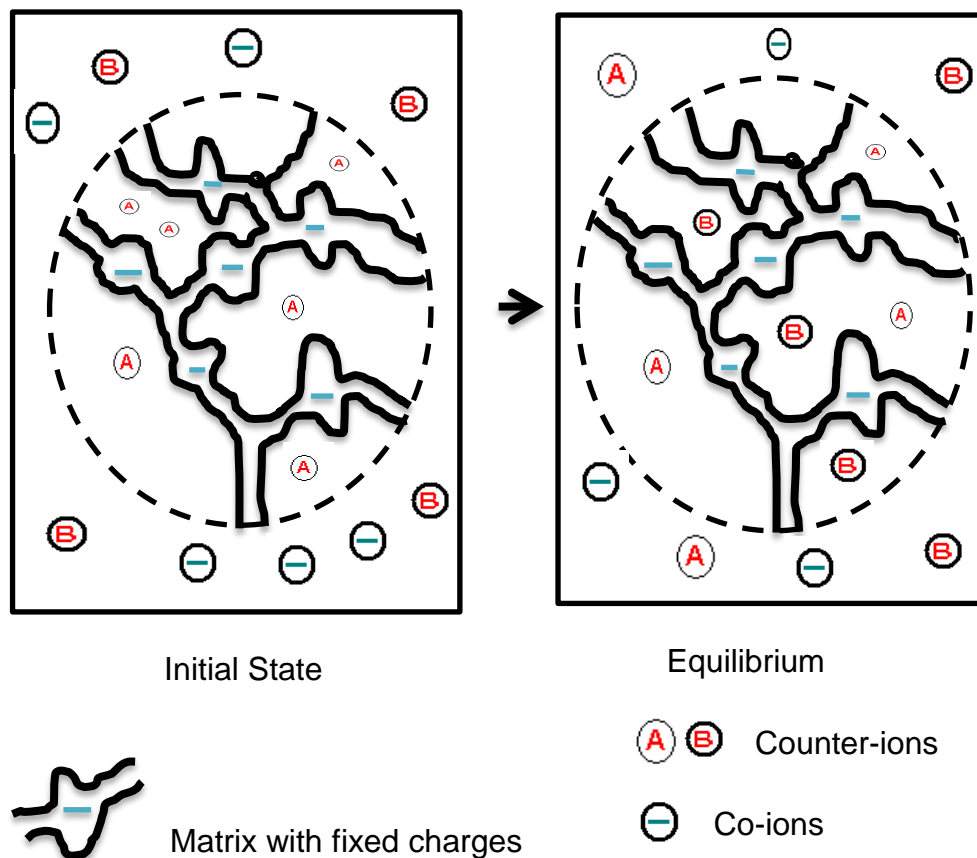
Figure 2.1: A typical cationic exchange resin system with an electrolytic solution. The resin contains A type counter-ions which are replaced by B type counter-ions in an equilibrium process (adapted from Helfferich (1962:6)).

Ion exchange resins are mostly used in economic sectors such as power generation, food and beverages preparation, chemical purification, drinking and waste water treatment as well as other applications of technology. Markets and Markets (M&M) predicts that the ion exchange industry will be worth more than $2 billion by 2026. The compound annual growth rate (CAGR) of the industry is projected at 4.15% from 2016 through 2026. Globally, Asia-Pacific is the leading ion exchange resin consuming region. It and North America account for more than 70% of the market. The factors driving the global increase in use of resins include population growth, which necessitates increased power generation as well as water and wastewater treatment amongst other applications.

2.5.1 Ion exchange use

Ion exchange chromatography is popular with biochemical processes because many biological molecules are charged at particular pHs. It is a separation technique that can be used for molecules or ions based on the interactions between charged solute and oppositely charged molecules linked to a matrix. This matrix may be mineral in nature e.g. zeolites, it may be coal which contains carboxylic acid or other weak-acid functional groups.

Liquid ion exchangers have also been used. These are obtained by dissolving compounds with ionogenic functional groups in organic solvents, which are immiscible with water. When contacted with contaminated aqueous solutions, the ion exchange occurs.

Many other materials have the potential to be used as ion exchange materials, but ion exchange resins are currently the most important class of ion exchangers. Since they are cross-linked, they are sufficiently hydrophobic to permit effective ion exchange. Only solvents capable of breaking carbon-carbon bonds, which are a result of the crosslinking, can dissolve the resin (Coulson *et al*, 1991:823).

Because of its polymeric nature, the matrix of ion exchange resins is elastic and is a flexible random network. The degree of crosslinking and the nature of the ionogenic functional groups determine the stability and the effectiveness of the resin. For ion exchange to occur, the ions in the solute should display higher affinity to the co-ions in the resin than the counter-ions within the resin itself. For instance, Cu^{2+} has a higher affinity for most weak acid resin's co-ions than the proton, which is the counter-ion in the prepared weak acid resin matrix (Trujillo, Spinti & Zhuang, 1995:233).

The major advantages of ion exchange purification are high removal efficiency as well as relatively fast kinetics. Additionally, where a solution contains more than one contaminant, ion exchange resins are suitable as they effectively remove most contaminants without selective bias (Purkayastha, Mishra & Biswas, 2014).

Amongst its many uses, ion exchange is also used in solvent reclamation. The advantage it displays over technologies such as thermal reclamation and electrodialysis, is that absorbent losses are virtually eliminated and reclamation

costs are minimised. Moreover, degradation of the solvent is avoided (Gao *et al,* 2015).

Increasingly, ion exchange resins find use in the nuclear industry. They are used to purge radioactive contaminants like neutron activation products as well as fission products which tend to leak from fuel elements. Ion exchange resins are employed in the demineralisation of wastewater emanating from nuclear power plants, recycle of nuclear fuels as well as the decontamination of nuclear installation, amongst many uses (Wang & Wan, 2015).

2.5.2 Ion exchange resin characterisation

Ion exchange resins can be characterised as strong cation exchange resins, weak cation exchange resin, strong anion exchange resin and weak anion exchange resin. The word strong or weak-ion exchange resin is referring to the extent of variation or lack thereof of ion exchange potential with pH, not necessarily the binding ability of the counter-ions. Strong ion exchange resins are completely ionised on virtually all pH units, whereas weak ion exchange resins have a range of pH units, where they are ionised. The degree of dissociation and therefore exchange capacity of weak ion exchange resins varying markedly with pH. Due to this difference, strong ion exchange resins are much easier to operate, because one less parameter: pH, needs to be controlled.

The factors affecting the equilibrium distribution of ions between the resin and electrolyte include

- temperature,
- degree of ionisation of solvent,
- the actual solute and the nature of the resin itself amongst other things

Generally, a concentration gradient between the liquid phase and the resin is the driving force for the diffusion of ion to the resin. An additional requirement for ion exchange, in contrast with adsorption, is the need to maintain electro-neutrality of the system (Coulson *et al*, 1991:825).

The porosity of the resin matrix is a crucial parameter, because the charged species are inside as well as outside the matrix. Effectively, the matrix can be viewed as a

molecular sieve; large molecules may be excluded and small ones may be absorbed. This affects the capacity parameter. Another parameter which may affect porosity and therefore capacity, is the mesh size. A fine mesh size results in an increased surface area to volume ratio, and therefore increased capacity and decreased time for ion exchange. On the downside, the flowrate is severely limited. Accordingly, an appropriate mesh size must be chosen, for optimal ion exchange.

Ion exchange can be considered as a special case of adsorption; a form of chemisorption. Furthermore, the sorption may be studied as a function of pH for weak acid resins. The sorption mechanism can be interpreted based on the structural traits of the pores in the virgin resin and the resin after sorption (Coulson *et al,* 1991:826; Stefan & Meghea, 2014).

2.5.3 Chemistry of complex formation

Ion exchange chelating resins are demonstrably very useful in the removal of metal cations in solution because they display a high selectivity and ability to form complexes. This behaviour shows a strong correlation to pH due to the variability of the ionisation of the ionogenic groups and therefore the capacity, in the resin with pH. Moreover, the capacity also shows a strong dependence to the decomplexing pH (DpH); at pH values below the DpH, the formed complexes may rupture, rendering the purification ineffective (Valverde *et al,* 2005).

Typically, ion exchange resins contain sulphur, nitrogen and oxygen functional groups. The Irving-Williams series predicts the stability of transition element cation complexes with the afore-mentioned functional groups. This is because, it qualitatively explains the stability of the formed complexes using coordination chemistry. The magnitude of the stability parameter is highly dependent on the metal centre of the resulting ligand. The stability for the transitional metals tracks the following trend:

$$Mn(II)<Fe(II)<Co(II)<Ni(II)<Cu(II)>Zn(II)$$
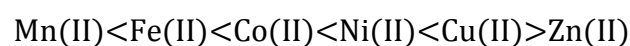
Electrostatic effects play a major role in determining the order of stability parameters: the effective nuclear charge shows a gradual increase across the period, hence the ligands are bound more and more tightly traversing the period. It

is rationalised from the variation of ionic radius and crystal field stabilization energy (CFSE), which quantifies the stability when a transitional metal ion in the crystal field, is attached to a set of ligands. When d-orbitals are split in a ligand because of the repulsion of electrons in the d-orbitals of the metal, many of them tend to have lower energies than before with respect to a spherical field known as the barycentre in which the five d-orbitals are degenerate. These are general concepts in ligand field chemistry that are used to predict the behaviour of the transition elements regarding complex formation (Demirçivi *et al*, 2013).

The ligand field stabilization energy (LFSE) encapsulates these concepts resulting in a reasonably coherent narrative. It is an extension of CFSE with a focus on splitting of the d-orbitals and the different energies that result when that occurs. Fundamentally, not all ligands cause an equal amount of splitting. To provide a fuller picture on the difference in splitting, the spectrochemical series was defined. It is an ordering of different potential ligands for metals ranging from what is referred to as weak field ligands, these cause a relatively small split in the d-orbitals, to strong field ligands, and these cause a large split in the d-orbitals energies:

$$I\text{-}, Br\text{-}, Cl, F\text{-} < OH\text{-} < H_2O < NH_3 < CN\text{-} < CO$$

Weak field   Strong field

This is largely due to the differences in electronegativity: weak field ligands tend to be highly electronegative, thus they hold the electrons tighter. This causes less repulsion with the electrons in the d-orbital. On the other hand, strong field ligands are comparatively less electronegative, hence the electrons are relatively loosely held meaning more repulsion with the d-orbitals is favoured. This causes a greater split in the d-orbitals energies. Generally, Fe (II), Co (II), Ni (II) and Cu (II) complexes have extra stabilization which is proportional to the LFSE (Chakraboty, 2012; Fleischer, 2005).

2.5.4 Ion exchange operation

In practice, the operation of ion exchange purification involves:

➢ Equilibration, which is the replacement of counter-ions that originally comprise of the ion-exchange resin, with more readily exchangeable ones e.g. most

cationic ion exchange resins are transported in sodium form, during equilibration, the sodium cation is replaced with a proton.

➢ Sample absorption occurs subsequently to equilibration. The solute ions replace the counter-ions, thereby purifying the solution/solvent.

➢ Elution is the regeneration of the resin by removing the absorbed contaminants. This is typically effected by changing the pH, such that the contaminant ions no longer enjoy favourable conditions to be attracted to the co-ions of the resin.

➢ After equilibration as well as after elution, the resin is washed generously with ultrapure water to remove ions that may very well compete with the co-ions in the resin, therefore rendering the purification ineffectual.

2.5.5 Selectivity

The equilibrium between ion exchangers and solutions, is of interest because it affects the distribution of the competing ions between the ion exchangers and the solutions. In organic ion exchangers, sorption and swelling are prominent equilibria phenomenon. Due to the increase of the osmotic pressure in solutions, swelling becomes much more pronounced in resins; the volume of the beads is heavily dependent on the composition of the solution (Lafond *et al,* 2015).

The advantage of organic exchangers over other types of exchangers, is primarily due to the tailorability of certain parameters in organic exchangers. These include the structure, degree of crosslinking, capacity, etc. These aspects either influence or are influenced by equilibria considerations (Helfferich, 1962:97).

Indeed, the equilibrium distribution of ions between the resin and the mobile phase depends on temperature, degree of ionisation of the mobile phase, the nature of the solute. In the interest of simplicity, one can assume that the resin is fully ionised, the solvent is not ionised, whilst the solute is completely ionised. At the exclusion of other mechanism, only ion exchange is considered. Hence a counter-ion can be expected to diffuse down any concentration gradient that exists between the porous solid and the liquid. The maintenance of electro-neutrality is another requirement. This is known as the Donnan potential along the existence of the concentration gradient (Coulson *et al*, 1991:825).

Mobile co-ions are limited almost completely to the liquid phase. Indeed, some may diffuse into the resin accompanied by charge balancing counter-ions. The net effect will essentially be an increase in the quantities of ions in the resin causing it to swell. This has a cumulative effect of increasing the exchange capacity above that which arises from the fixed ionic groups alone. Swelling is a reproducible equilibrium trait of a resin, dependent on its degree of crosslinking and its ion exchange capacity, as well as the temperature and the solution composition (Coulson *et al*, 1991:825).

Polyvalent exchanging ions result in more cross-linking within the resin and hence result in less swelling than the monovalent ions. $Al^{3+} < Ca^{2+} < Na^+$. Water swelling is overwhelmingly the consequence of hydration of ionic groups. When ionic equilibrium is examined, as an exercise in convenience, the exchange is normally written in a form of chemical equation. For example, the purification of ammonium fluoride designed to remove copper (II) ion from the solution can be written:

$$Cu^{2+} + R - 2COOH \rightleftharpoons 2H^+ + R - CuCOO_2 \qquad (2.9)$$
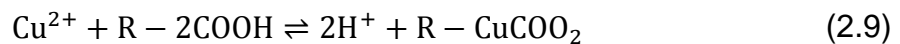
R is the cationic exchange resin framework. In general, the exchange of an ion A of valency v_A in solution, for an ion B of valency v_B on the cationic resin can be written:

$$v_B A + v_A B(R) \rightleftharpoons v_A B + v_B A(R) \qquad (2.10)$$

Including activity coefficients ɏ the thermodynamic equilibrium constant K_{equil} becomes:

$$K_{equil} = \frac{(ɏ_B[B])^{v_A}(ɏ_{A,R}[A_R])^{v_B}}{(ɏ_A[A])^{v_B}(ɏ_{B,R}[B_R])^{v_A}} = \frac{(ɏ_B)^{vA}(ɏ_{A,R})^{vB}}{(ɏ_A)^{vB}(ɏ_{B,R})^{vA}} K \qquad (2.11)$$

K is the selectivity coefficient. In dilute solutions, the activity coefficient approach unity and the selectivity coefficient approximates the equilibrium constant. When the selectivity coefficient is greater than unity, the exchanger takes up ion A in preference to ion B (Coulson *et al*, 1991:826).

In the case of the purification of ammonium fluoride from copper (II) contamination, the selectivity coefficient is:

$$K = \frac{[H^+]^2[Cu(COO)_2]}{[Cu^{2+}][COOH]^2} = \frac{\left(2([Cu^{2+}]_o - [Cu^{2+}])\right)^2([Cu^{2+}]_o - [Cu^{2+}])}{[Cu^{2+}]\left([COOH]_o - 2([Cu^{2+}]_o - [Cu^{2+}])\right)^2} \qquad (2.12)$$

2.6 Ion exchange mechanism and kinetics

The mechanism of ion exchange may be broken down to:

- The diffusion of the ion from the bulk solution to the exchanger surface. This occurs rapidly in homogenous solutions.
- The diffusion through the matrix structure to the actual exchange site of the resin, where binding occurs. The degree of crosslinking of the exchanger as well as the concentration of the solution, play a pivotal role in this step of the mechanism. In most cases, this is the rate limiting step in the ion exchange process.
- The exchange of ions at the exchange sites of the resin. This tends to happen instantly and is an equilibrium process e.g.

$$R - 2COO^-H^+ + M^{2+} \rightleftharpoons R - (COO)_2^- M^{2+} + 2H^+ \qquad (2.13)$$
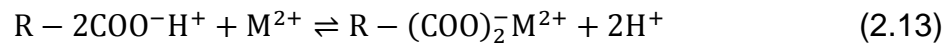
The more charged the ion is, the tighter it is bound to the exchanger.

- The diffusion of the counter ion from the exchange site to the surface of the resin.
- The diffusion of the ion from the surface to the external eluent.

Figure 2.2 is the graphical representation of these steps in ion exchange. Invariably, the rate limiting step in ion exchange processes is inter-diffusion of the counter-ions within the exchanger. Unlike external mass transfer limitations, this unaffected by the agitation of the solution (AlOthman, Alam & Naushad, 2013).
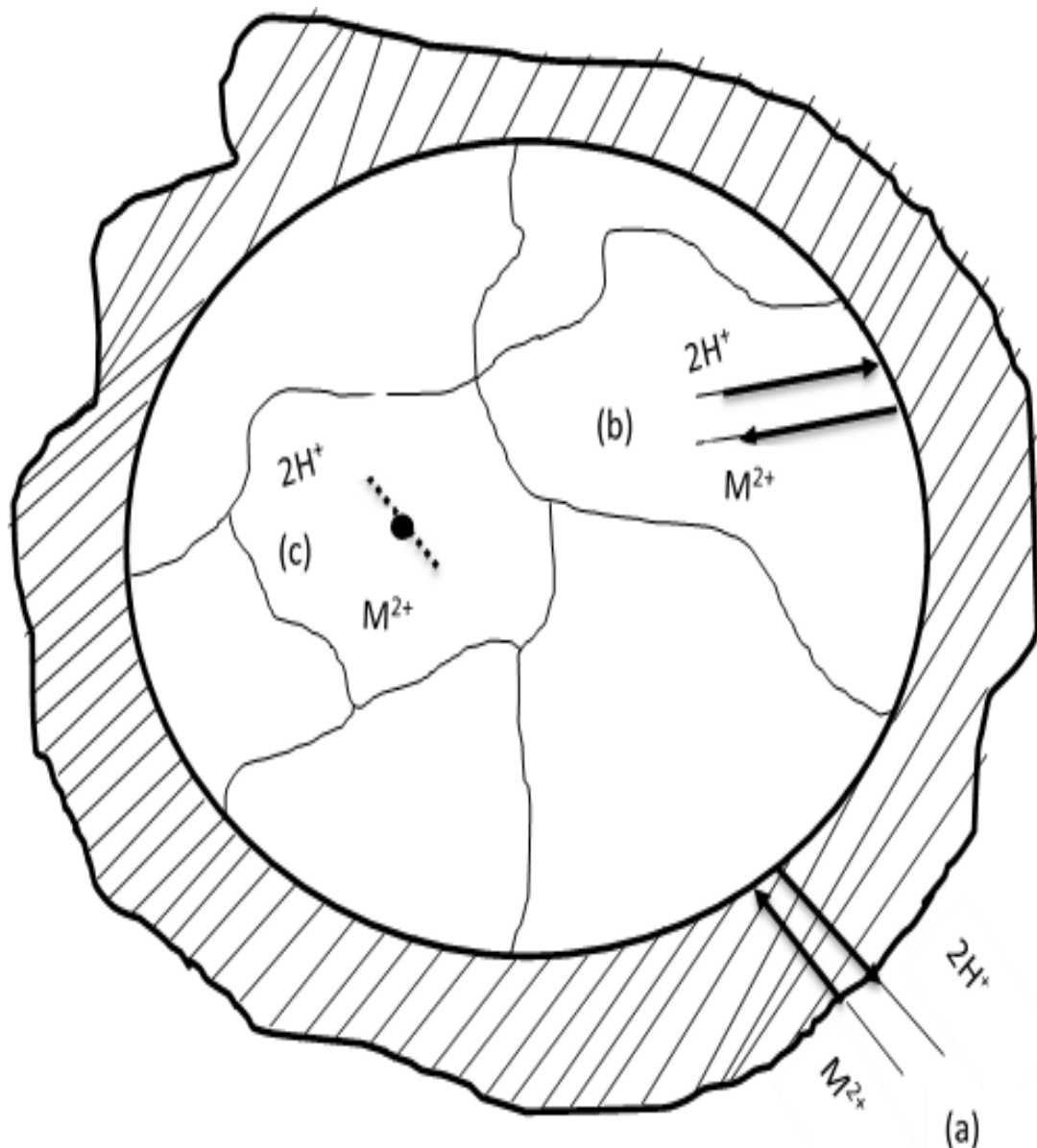
Figure 2.2: Ion exchange mechanism a) Film diffusion. (b) Intraparticle diffusion. (c) Chemical reaction (adapted from Harland (1994:136)).

Kinetic expressions in ion exchange are based on conservation of mass considerations. In adsorption, these expressions often take the form of adsorption reaction model (ARM), wherein the adsorption is regarded as a reaction rate controlled process; adsorption diffusion model (ADM), wherein the diffusion path of the sorbate inside the pellet is considered in the model; and the double exponential model (DEM), where internal and external diffusion is taken to account (Russo *et al*, 2015).

In ion exchange, an analogous approach can be taken i.e. kinetic data can be analysed in terms of ion exchange reaction model (IERM), where the ion exchange phenomenon is expressed as a reaction rate process. Alternatively, the ion exchange intraparticle diffusion model (IEDM) approach can be followed. Moreover, the DEM approach could be used in ion exchange in a similar way as it can be used in adsorption.

2.6.1 Apparent kinetics

Following the IERM approach, the reaction can be represented as the reaction of the carboxylic functional group with the contaminant cation:

$$2COO^-H^+ + Cu^{2+} \quad \rightleftharpoons \quad Cu\,(COO)_2 + 2H^+ \tag{2.14}$$

The reaction can be regarded as a closed system wherein the mass balance of the metal cation, and application of first principles of reaction kinetics allows for the mathematical representation of the apparent reaction rate equation. Thus, mass balance of Cu^2:

$$-\frac{d[Cu^{2+}]}{dt} = k'[COOH]^2[Cu^{2+}] - \frac{k'}{K_{equil}}[Cu(COO)_2][H^+]^2 \tag{2.15}$$

To write the capacity $[COO^-H^+]$ in terms of the copper concentration, one considers that the capacity remaining or the number of moles of COO^-H^+ remaining at any time is the starting number of moles minus the change in the number of moles of COO^-H^+ i.e.

$$N_{COOH} = N_{COOHo} - \Delta N_{COOH} \tag{2.16}$$

From the reaction stoichiometry, the change in the number of moles of COO^-H^+ is twice the change in the number of moles of Cu^{2+}. Likewise, the other reagents can be written in terms of the concentration of Cu^{2+}. Therefore, equation (2.15) becomes

$$\frac{d[Cu^{2+}]}{dt} = k'\,([COOH]_o - 2\{[Cu^{2+}]_o - [Cu^{2+}]\})^{\,2}\,[Cu^{2+}]$$
$$- \frac{4k'}{K_{equil}}\,([Cu^{2+}]_o - [Cu^{2+}])^3 \tag{2.17}$$

The conversion at equilibrium can be computed from equation (2.17) since the system is at steady state:

$$k' \left([COOH]_o - 2\{[Cu^{2+}]_o - [Cu^{2+}]\}\right)^2 [Cu^{2+}]$$
$$- \frac{4k'}{K_{equil}} \left([Cu^{2+}]_o - [Cu^{2+}]\right)^3 = 0$$

$$k'_o e^{-\frac{E}{RT}}\left([Cu^{2+}]_o(1 - x_e)\right)\left([COOH]_o - 2([Cu^{2+}]_o x_e)\right)^2$$
$$- 4\left(\frac{k'_o e^{-\frac{E}{RT}}}{K_{eqo}e^{-\frac{\Delta H_{rx}}{RT}}}\right)([Cu^{2+}]_o)^3 x_e^{\;3} = 0$$

(2.18)

2.6.2 Mass transport

The mass transfer coefficient is inversely proportional to the boundary layer thickness, with the proportionality constant being the diffusion coefficient. The hydrodynamic radius of the particle plays a significant role on the overall reaction rate. At low speeds, the boundary layer is thick and may contribute to retardation of the reaction rate, whilst at higher speeds the boundary layer is so small that for all intents and purposes it may be considered to be negligible. In this case, the concentration at the surface of the pellet is regarded as the same as the bulk concentration. This is the case in this text (Young Kim *et al,* 2015).

In ion exchange resin processes, intraparticle diffusion is usually the rate limiting step, particularly if the solution is in the liquid phase. Workers in the field of ion exchange posited empirical expressions to represent the assimilation of the ions into the resin. These do not include the actual reaction or attachment of the counter-ions once inside the pores, which is an inherent limitation. For purposes of approximating the orders of magnitude of the diffusivity, these are sufficient. One of these is

$$\frac{d[Cu^{2+}]_s}{dt} = \frac{\pi^2 D_r}{r_i^2}\left([Cu^{2+}]_s^{\;*} - [Cu^{2+}]_s\right)$$

(2.19)

This results in a parabolic estimation of the concentration profile and can be compared to the experimental results to obtain necessary reaction rate parameters such as the effective diffusivity (Coulson *et al*, 1991:1061; García-Mateos *et al*, 2014).

The diffusivity of the counter-ions into and out of the resin is indicative of intraparticle diffusion. This is a crucial parameter in the design and use of ion exchange resins in the purifications of contaminated ammonium fluoride solution (He, Azarian & Pecht, 2014).

The pores in resin pellets are the sites of reaction. They tend to be a series of tortuous, interconnecting paths of pore bodies with varying cross-sectional areas (Gritti & Guiochon, 2014). The average effective diffusion, at any position in the pellet is of interest, rather than diffusion in each pore body (Everson, Neogamus & Kaitano, 2011). Hence the effective diffusivity is directly proportional to pellet porosity and the constriction factor which accounts for the disparity in cross-sectional area that is perpendicular to diffusion. It is also directly proportional to the concentration gradient as explained by Fick's law (Russo *et al*, 2015).

2.6.3 Weisz-Prater criterion

Regarding the limiting step of the reaction, the diffusion rate can be compared to the observed reaction rate. Weisz and Prater devised a method to determine when a reaction is not retarded by the internal mass diffusion. The Weisz-Prater criterion involves the analysis of the quotient between the observed reaction rate and diffusion rate.

$$C_{wp} = \frac{-r_{observed}(r_i)^2}{D_r[\text{A}]_I} \qquad (2.20)$$

The concentration of the counter-ion is the surface concentration, this is the same as the bulk concentration because the external mass transfer limitations are negligible. If the Weisz-Prater is significantly lower than unity, and diffusion is not the limiting step. Conversely, if it is pointedly greater than unity, it can be deduced that diffusion is the limiting step (Fogler, 2006:839).

2.7 Column operation/breakthrough

The purification of ammonium fluoride spiked with copper (II) cation on a column, appears to be suitable for modelling as a tubular reactor. Figure 2.3 displays the dimensions of the burette. Using the control volume approach, the differential equation in this regard is:

$$\frac{-F_T}{A_C}\frac{MM_{sol}}{\rho_{sol}}\frac{\partial[Cu^{2+}]}{\partial z} - k'\left([Cu^{2+}][-COOH]^2 - \frac{1}{K_{equil}}[Cu(COO)_2][H^+]^2\right)$$
$$= \frac{\partial[Cu^{2+}]}{\partial t}. \tag{2.21}$$

The other species of the reaction can be written based on this equation with the appropriate stoichiometric factors. The next logical step would be to discretise the resulting partial differential equation with respect to time and position, then implement an integration technique to model the breakthrough curve. This approach fails to produce good modelling results.

Other methods include treating ion exchange in column operations, mathematically as an adsorption process. Conventionally breakthrough profiles are generated using classical linear driving force (LDF) modelling. This is typically used to account for external mass transfer phenomenon as well as intraparticle diffusion (Leinekugel-le-cocq *et al,* 2007).

For LDF, one of the most important variable is the total concentration of the exchangeable binding sites. In the case of ion exchange resins, this is closely related to the apparent capacity (Hackbarth *et al,* 2015). The crucial drawback of the LDF is the relatively large errors it produces at short times (Patton, Crittenden & Perera, 2004).

During breakthrough, the exchangeable binding sites are not necessarily zero, but rather an increasing number of them are becoming inactive. In ion exchange, this could be due to the decreased ionisation of the functional groups. Deokar & Mandavgane (2015), posited that this phenomenon can be modelled as deactivation kinetics, in similar fashion to gas-solid reactions characterises by the so-called shrinking core model.

Solute transport tends to be governed by the spatial distribution of hydraulic properties. Customarily, it is modelled as a random space function (Fiori *et al,* 2015). Indeed, the ionisation/deionisation of the functional group in the resin, can be regarded as a reaction. The reaction rate thereof, can be modelled as a power law expression. Hence the random space function can plausibly be represented as a power law expression (Fiori & Becker, 2015).
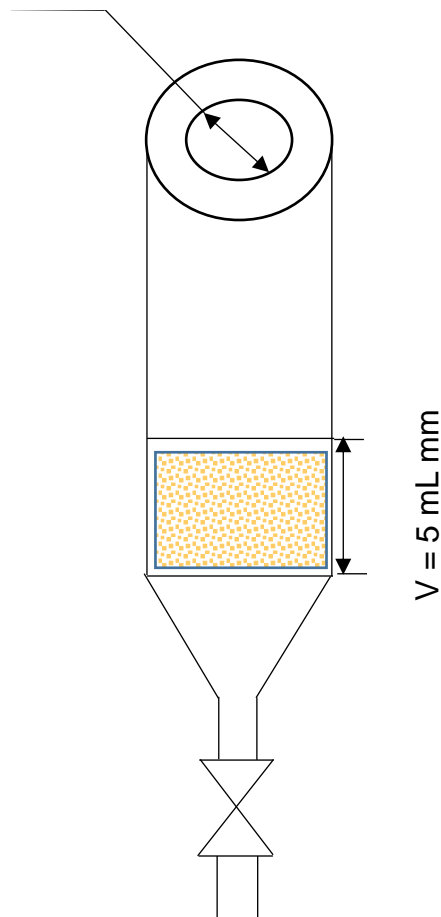
Figure 2.3: Dimensions of the burette of interest.

If the reaction of the metal cation with the resin is regarded as an irreversible reaction, the backward reaction naturally falls away. The reaction itself may not be necessarily elementary. Prior to breakthrough, within the mass transfer zone, the metal cation starts off at the concentration of the solution and decreases to zero. At breakthrough, it decreases, but not to zero. To simplify mathematical manipulations, it is practical to regard this phenomenon to be linear in nature i.e. the concentration gradient in the transfer zone, is governed by a straight line.

Most reactions follow power law reactions. For those who do not, stochastic methods may plausibly be utilised to model the reaction. A crucial parameter in this process, is the flow regime under which the reaction occurs. The modelling can be executed with integrity for laminar as well as turbulent flow.

In the packed bed operations, external, internal mass transfer and reaction factors play a role. If the reaction is constrained by intraparticle mass transfer, the diffusivities

of the two counter ions, play a major role in the kinetics. Intuitively, since the reaction is constrained by internal mass transfer, the diffusivity parameter will play a major role.

To maintain the relative simplicity of the integration, a parameter having the dimensions of the square of the product of the resin depth and the external mass transfer coefficient, G_{corr} is defined. Thus, the effective reaction constant, comprises of the reaction rate constant, k', the square of the pseudo-diffusivity pre-exponential constant, D_{ro}, and G_{corr} which considers the different masses of the counter-ions, bed porosity, pressure drop, external mass transfer limitations, bed depth etc.:

$$k'_{eff} = G_{corr} \left(\frac{1}{D_{ro}}\right)^2 k' \tag{2.22}$$

The mass transfer parameter is squared because two counter-ions are involved: one diffuses in whilst the other diffuses out of the resin. The temperature dependence of the effective rate constant is reflected on the apparent reaction rate constant rather than any of the mass transfer parameters. This empirical deduction is only applicable when the flow regime is laminar. Turbulent flow is likely to be governed by a different empirical deduction which falls outside of the scope of this text.

Given all these considerations, the resin bed can be divided into layers of the transfer zone, wherein the reaction occurs in a plug flow manner, until the next layer. The process repeats itself until the whole depth of the bed is traversed by contaminant. In their simplest form, breakthrough curves are a concentration profile history of effluent from ion exchangers.

Empirically, the ion exchange bed is modelled as a fixed bed with multiple layers comprising of mass transfer zones wherein the mobile phase upstream, has the feed concentration of metal cation, downstream of the layer, the mobile phase has a zero concentration of the metal cation prior to eventual breakthrough of the cation. On breakthrough, the concentration downstream is the cumulative sum of the prior breakthrough concentrations and the current breakthrough concentration as per effective rate constant.

The current breakthrough concentration of the metal cation is calculated from a modified Euler-type integration which assumes a linear variation of the metal ion

concentration with axial distance i.e. the concentration of the metal cation is dependent on time as well as position. As a first approximation, the position dependency is presumed to be linear. Figure 2.4 illustrates the principle of the integration.
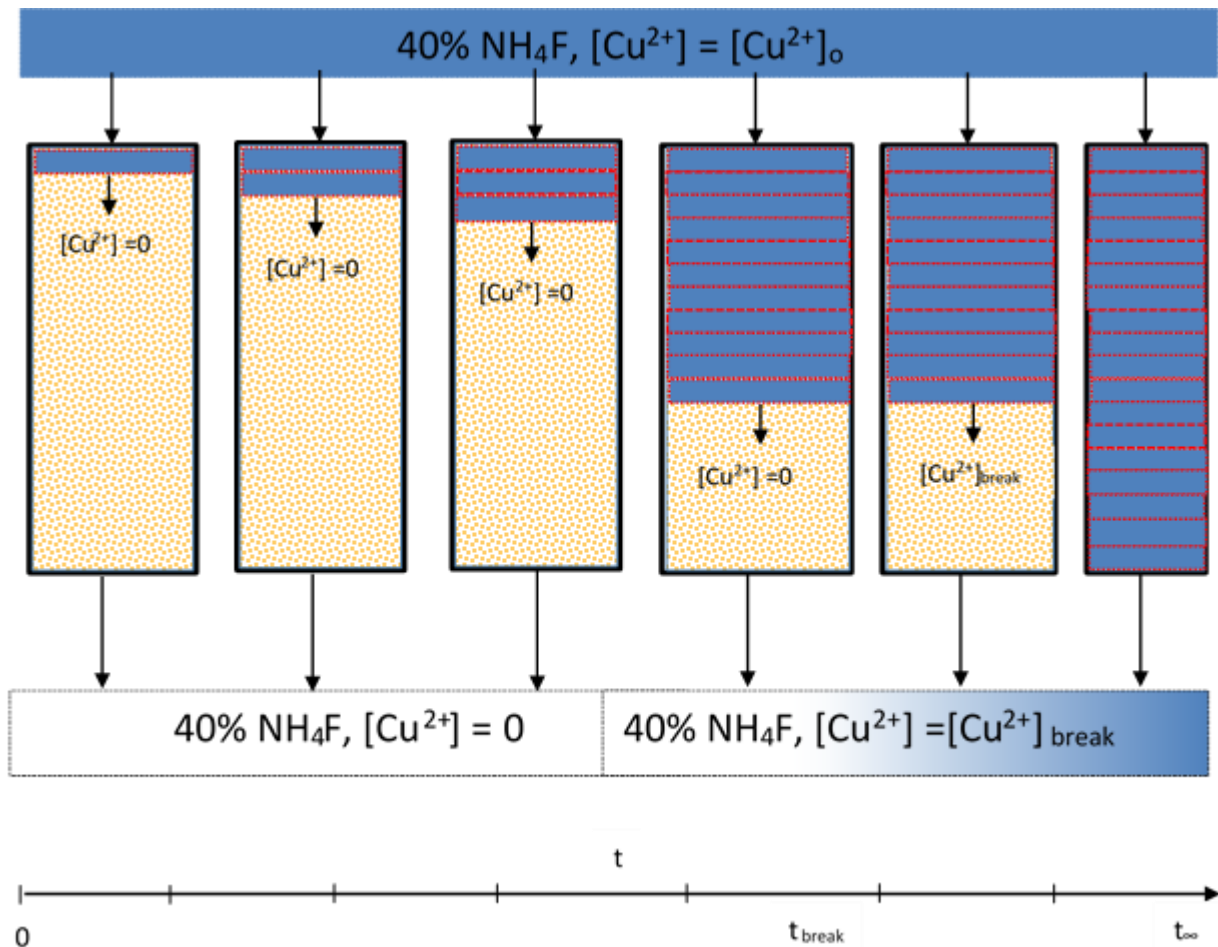

Figure 2.4: Modified Euler integration encompassing time elapsed and axial distance covered by metal cation in the resin. The depth of the bed is subdivided into various elements, (L_1, L_2, etc.) wherein simplified Euler integration is conducted.

It is noteworthy that breakthrough occurs before the resin is saturated with the metal cation. Furthermore, the metal cation is not only removed from solution due to ion exchange, but some physisorption takes place. Thus, a level of uncertainty is inherent in the modelling of the breakthrough curves. Considering this, an additional variable is introduced to account for this uncertainty. It is arbitrarily chosen as a power law expression dependent on position:

$$uncertianty = constant1(z)^{constant2}$$
(2.23)

In this case, z is the displacement within a layer of resin depth as per

Figure 2.4. Mathematically, the integration can be represented as:

$$[Cu^{2+}](i,j) = \sum_{i=0}^{m}\sum_{j=0}^{n}[Cu^{2+}](i,j)$$
$$- timestep\langle constant3 \times slope(i,j)$$
$$+ k'_{eff}[Cu^{2+}]^2(i,j)[COOH]^2(i,j)\rangle$$

$$[Cu^{2+}](t,z)$$
$$= \begin{cases} 0, & [Cu^{2+}](i,j) < det.limit\ ICP-OES \\ [Cu^{2+}](i,j) + uncertainty, & [Cu^{2+}](i,j) \geq det.limit\ ICP-OES \end{cases}$$
(2.24)

Sometimes, dimensionless variables are convenient in the drawing of breakthrough curves, in that for the right conditions, they can be used in predictions of breakthrough at different flowrates, concentrations etc. than the ones used to generate the breakthrough curve of interest. This is very useful in the case of industrial use of ion exchangers: breakthrough curves can be generated at laboratory scale, the information gleaned from them can be applicable at industrial scale if in the two cases (laboratory and industrial) mass transfer limitations are eliminated. Thus, from laboratory generated breakthrough curve, the breakthrough at industrial scale can be predicted. This approach, is a simpler and potentially more effective method than following the complex mathematical approach to predict the breakthrough.

When the resin bed is saturated with cations, the feed concentration of the solution remains unchanged, after absorption on the bed. Thus, the dimensionless concentration at capacity, is 1. The design capacity (a dimensionless quantity), should

be specified at a value less than that as a precautionary measure. The dimensionless time it takes the resin to reach capacity, can be read off from the breakthrough curve. Even more useful, the dimensionless time it takes for breakthrough to occur, can also be read off from the graph. The time it takes for the resin to reach capacity is:

$$\text{time to saturation} = \left(\frac{\text{Design Flowrate} \times \text{Concentration at capacity}}{\text{resin capacity}}\right)^{-1} \quad (2.25)$$

The design flowrate is chosen such that there is no possibility of mass transfer limitations. Of more interest for industrial applications, is the time it takes until breakthrough occurs. This the product of the time to saturation and the dimensionless time when breakthrough occurs on the breakthrough curve.

2.8 Process considerations

If a substantially high heat of reaction needs to be removed from a process, various heuristics are considered. These include retaining inert streams rather than separating them from reactants prior to reaction. This approach has obvious implications for the size of the reactor. Another alternative is to use an excess of one or more of the reactants, to absorb the heat. This tends to increase the running costs of a plant, due the increased need of separator-recycle operations.

Use of colds shots; where one or more of the reactants is fed in a staggered fashion, can also be used. This has an advantage in that, a 'cold' reactant absorbs some of the heat already emitted and the heat of reaction released in the first place, is not as excessive because the one of the reactants, at any given time, is present in smaller quantities.

Once the reaction scheme to produce a desired product has been chosen, sources and sinks are matched. In industrial process systems, this invariably means recycle of unused reactants and the storing of products. Additionally, inerts and products of undesirable side reactions should be disposed of. In the case of reversible side reactions, these are recycled to extinction i.e. the Le Chatelier's principle is used to favour the backward reaction rather than the forward reaction for those side reactions. In the case of irreversible side reactions, purge streams are used to eliminate the build-

up of undesirable products in the system, potentially clogging it. This is not done in the case of hazardous or environmentally harmful products.

Continuous industrial reactors can be considered to lie between two ideal reactors: continuously stirred tank reactors (CSTRs) and plug flow reactors (PFRs). These two have a fundamental difference in terms of the concentration profile; PFR maintain a concentration profile, whilst the CSTRs, are perfectly mixed. This has implications on the conversion achieved in a given process.

Virtually, in all reaction process systems, separator unit operations are ubiquitous. In terms of capital expenditure, they often supersede the reactor systems. The principle of operation that is typically employed to effect the separations, is a difference in either physical and/or transport properties. For example, in liquids, the difference in volatilities is typically used as the driving force for separation. In solids, the difference in densities is used in that regard.

On completion of the process synthesis for any given product, equipment selection is usually the next logical step. This involves a creative process that seeks to judiciously achieve process objectives by using available/attainable resources with due consideration to the practical and financial imperatives. For instance, given the existence of a mining industry in South Africa, solid-solid equipment may be readily available on the market.

One of these include, spiral concentration equipment such as the Humphreys spiral concentrator. The driving force is the difference in specific gravity of the solids to be separated. Both gravity and the centrifugal force are used to separate lighter solids from heavier ones. In addition, friction and drag forces play a role in the separation (Perry & Green, 1997:19-34).

Although fluidised bed reactors are on the higher scale regarding operating costs, they have many desirable qualities. The mixing resembles that of a CSTR and temperature control is relatively easy. As with the other reactors, there is an interplay between mass transfer and reaction rate as the limiting steps of the reaction. Particle size and the density of the particles relative to the fluid density, are important parameters in the fluidisation (Fogler, 2006: CD12-3.2).

Geldart classified powders to four categories to account for the fluidisation properties. The Wen and Yu correlation can be used to determine the minimum fluidisation velocity, given particle size of pellets (Rhodes, 2008:171-175):

$$Ar = dp^3 p_f(p_s - p_f)\frac{g}{\mu^2}$$

$$Re_{mf} = (1135.7 + 0.0408Ar)^{0.5} - 33.7 \qquad (2.26)$$

$$U_{mf} = \frac{\mu Re_{mf}}{dp p_f}$$

A correlation for the maximum allowable velocity before the resin pellets are carried over out of the bed is (Fogler, 2006: CD12-3.11):

$$U_{max} = \left(1.78 \times 10^{-2}\frac{(p_s - p_f)^2}{p_f\mu}\right)^{1/3} d_p \qquad (2.27)$$

The operating fluidisation velocity is set between the lower bound of minimum bubbling velocity and the maximum allowable velocity.

The porosity of the bed at fluidisation is determined using a material balance:

$$\varepsilon_{mf} = 1 - \frac{h_s(1 - \varepsilon_s)}{h_{mf}} \qquad (2.28)$$

The diameter of the bubble, is an important parameter in fluidisation. Mori-Wen devised a correlation to determine this parameter (Fogler, 2006: CD12-3.15):

$$\frac{d_{bm} - d_b}{d_{bm} - d_{bo}} = \exp\left(\frac{-0.3h}{D_t}\right)$$

$$d_{bm} = 0.652\left[A_c(U - U_{mf})\right]^{0.4} \qquad (2.29)$$

$$d_{bo} = 0.0037(U - U_{mf})^2$$

The reaction rate in the fluidisation system is complicated by the three material balances that need to, be undertaken: bubble, cloud and emulsion phase balance. These should be solved simultaneously and for reaction orders other than first order, numerically. That exercise is beyond the scope of this text.

3 Experimental

3.1 Materials

Ammonium bifluoride ($NH_4F.HF$) was purchased from Protea Chemicals, and it is specified at 98% purity. Pelchem supplied the ammonium acid fluoride laden with contaminant cations. Industrial grade ammonia water solution, with an ammonia composition of 25% NH_3, was also purchased from Protea Chemicals. Laboratory grade copper (II) chloride ($CuCl_2.2H_2O$), was purchased from Merck KGaA.

Purolite supplied a weak acid ion exchange resin: Purolite S930Plus. Cwenga Chemical & Water Engineering Associates supplied Lewatit TP207, which just like the Purolite counterpart, is an iminodiacetic acid cation exchange resin. Figure 3.1 shows the structures of these resins. Suppliers of the resins claim the capacity of the two resins is at an identical 2eq/L.

$$N(CH_2COOH)_2$$

$$N(CH_2COOH)_2$$
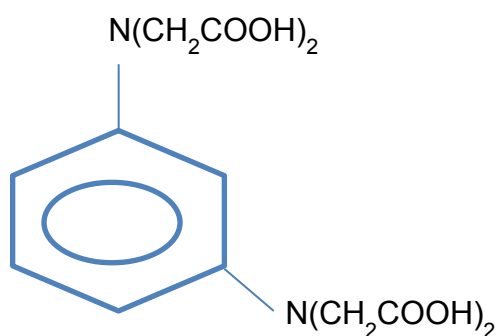
Figure 3.1: Iminodiacetic functional groups in cationic ion exchange resins.

3.2 Apparatus

An 826 pH mobile metrohm pHmeter was used to monitor the pH of solutions. This instrument is resistant to HF attack. A rudimentary isothermal water bath was assembled. This consists of a 2 L glass beaker, 500 mL polyethylene beaker, ceramic balls, an AGIMATIC-N magnetic stirrer and heater and A Heidolph Ekt Heikon temperature feedback control system. Figure 3.2 shows photographs of setup of this system.
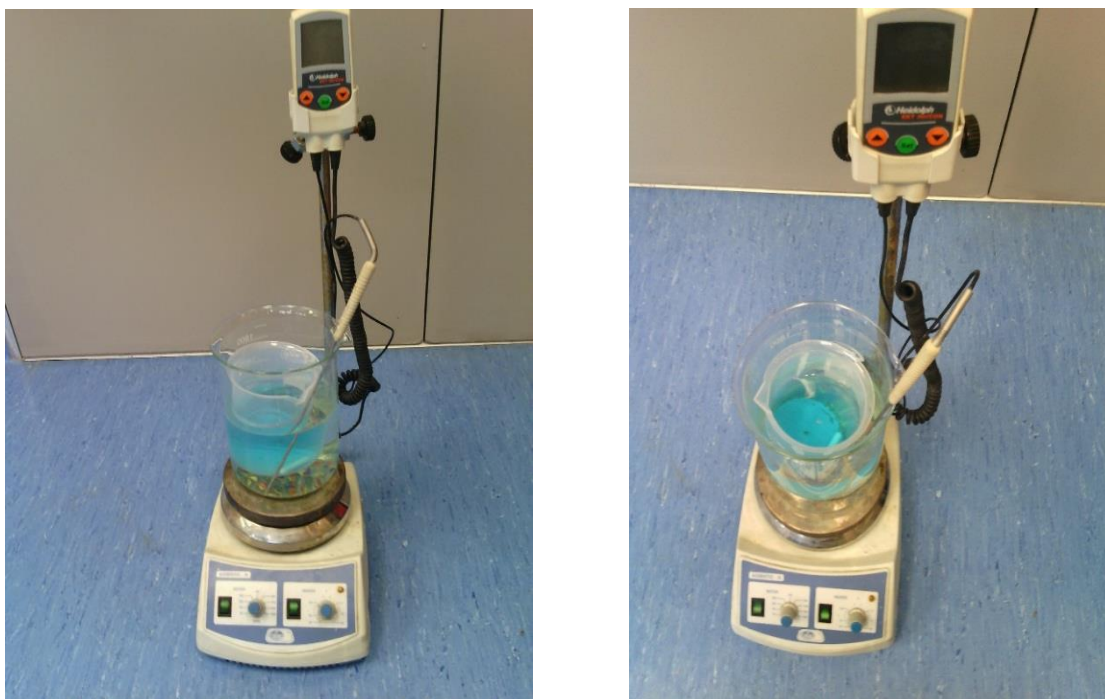
Figure 3.2: Isothermal water bath setup at a glance.

The fluoride content in the Pelchem sample was established using the Mettler Toledo Seven Compact fluoride ion electrode. Use was made of polyethylene burettes for the column experiments. The flowrate in the burettes was controlled using Hoffman clips.

The concentrations of the cationic species were determined using the inductively coupled plasma- optical emission spectroscopy (ICP-OES), as well as the inductively coupled plasma- mass spectroscopy (ICP-MS). A Spectra Acors ICP-OES is used. The characterisation of the resin was done with an ultrahigh resolution field emission scanning electron microscope (SEM) JEOL 6000F and a micromeritics TriStar II Surface Area and Porosity BET analyser. Thermogravimetric analysis was conducted with a TGA 4000 Perkin Elmer instrument for the determination of the breakdown temperatures of the precipitates.

3.3 Planning

The independent variable with respect to precipitation is the amount of ammonia water solution added. The solubility of the metal contaminant cations, shows a strong dependence on the pH of the ammonium acid fluoride solution. Of interest, is the amount of ammonia to be added to effect the most precipitation of the contaminant

cations. The measured variable is the concentration of the cations in the mother liquor, after various amounts of ammonia were added.

With respect to the static equilibrium experiments, the independent variable is 'infinite' time as well as the initial concentration prior to reaction. The change in concentration at a very long time or what can be referred to as 'infinite' time, is the measured variable. This establishes, the amount of contaminant absorbed in the resin, as well as the selectivity of the resin for the cation of interest.

Kinetic experiments have time as an independent variable, by their very nature. As with the equilibrium experiments, the measured variable is the change in concentration. This is done at finite time intervals as opposed to selectivity experiments, which are conducted at very long or 'infinite' time intervals. The most crucial output variables in these experiments are contaminant absorbed per unit time, reaction orders as well as the reaction rate constants. It may also be paramount to establish whether or not the intrinsic kinetics of the reaction have been determined.

With regard to the breakthrough curve experiments, the independent variable is the volume of liquid run through the resin. The capacity of the resin to absorb contaminant is the variable of interest. This is ascertained by measuring the concentration of those contaminants after liquid is run through resin.

The output variables discussed are inextricably interwoven together; the selectivity coefficient is indicative of the ability of the resin to absorb the contaminants, the reaction rate constants and reaction orders, determine how quickly the resin arrests the contaminants from the solution and the breakthrough curves combine all these aspects in a simple and easily accessible manner.

3.4 Methods

The project was predominantly a wet-lab based experimental investigation. Overwhelmingly, cationic ion exchange resins were investigated regarding its suitability to purify ammonium fluoride. Static equilibrium, chemical reaction rates, breakthrough curves and flow rates are amongst some of the aspects covered within the project from the experimental perspective. Precipitation of contaminants via pH adjustments were also investigated.

The Pelchem ammonium acid fluoride sample, may contain more contaminants due to the nature of the sampling process rather than the NF_3 production process itself. For an example, iron cations only leach into the sample through the mild steel drums that are used for the storage of the ammonium acid fluoride from the production process.

Additionally, the presence of all the contaminants at pre-set concentrations may hamstring the investigation: some cations may display a selective bias for absorption to the resins more than others, and they may be present in concentrations that are too low to expedite the determining of the aforementioned output variables and parameters. For instance, both copper and nickel are present in the Pelchem sample at concentrations that are too low to breakthrough within reasonable flowrates for the column experiments.

With this in mind, synthetic solutions of ammonium fluoride were prepared by neutralising ammonium bifluoride with ammonia water solutions. These were to be spiked with both copper and nickel cations to replicate the Monel material of construction contamination of the ammonium acid fluoride. However, nickel cation displays an inappreciable solubility in ammonium fluoride at relevant pHs. Therefore, only copper was used to spike the ammonium fluoride solution. This was generalised to other metal cations through the use of mathematical modelling with the continuity equation.

Using synthetic ammonium fluoride solutions at a pH of 6.89, spiked with 887.5 ppm copper (II) cations, the selectivity static experiments, kinetic experiments and the breakthrough experiments were conducted. For the selectivity experiments, 5 mL of each resin was immersed in 1 litre solutions and the slurry was stirred with a small magnetic stirrer for approximately 9 hrs. To understand the role that the pH of the solution plays, 40 % ammonium bifluoride spiked with copper (II) cations, was also investigated with regard to the capacity of the resins. The concentration of the copper varied between 695 ppm and 936 ppm. Subsequently, the solution was decanted to separate it from the resin and the concentration of the cation in solution was analysed.

Ammonium fluoride solutions are capable of etching thermocouple probes. These are typically fabricated from nickel based alloys. In the case of the kinetic experiments,

this is undesirable, not only due to the potential damage to the probes, but also the nickel and iron may decrease the selectivity of the copper cation by competing against it in the absorption by the resin. Therefore the temperature of the ammonium fluoride-resin slurry cannot be measured and controlled directly. Instead, a polyethylene (PE) beaker containing 200 mL of the 40% NH_4F spiked with 887.5 ppm copper (II) cations, is immersed in a 2 L glass beaker with ceramic marbles at the bottom and 550 mL of water. The marbles ensure that the polyethylene beaker is not subjected to direct heat, the water serves as a water bath (see Figure 3.2). The water temperature in the glass beaker serves as an indirect measured variable for the temperature of the ammonium fluoride solution.

Prior to the commencement of the experiments, the 500 mL polyethylene beaker is filled with 200 mL water and the 2 L glass beaker, with 550 mL water. This is to replicate the dimensions of the contents of the experiments. For the temperatures of interest; 30 °C, 50 °C and 65 °C, the temperature in the water in both beakers, is measured. This is to calibrate what the temperature in the glass beaker should be, to have a certain temperature in polyethylene beaker. For an example, to have a temperature of approximately 65 °C in the polyethylene beaker, the temperature in the water contained within the glass beaker, must be 76.5 °C. The setpoint point temperature in the temperature feedback system, is set at the appropriate temperature and time is allowed to pass for the thermal stability of the system.

Experiments themselves, have a duration of 30 minutes. They commence after the temperature of the system is stable. Immediately when the 5 mL resin is put into the PE beaker containing copper-NH_4F mixture, the stop watch is started. Sampling occurs at 1 mL every minute for the first five minutes, every two minutes for the next ten minutes and every five minutes for the last fifteen minutes.

The column breakthrough curve experiment involved the use of plastic burettes. A 5 mL bed volume for the resins was chosen. Cationic resins are normally transported and stored in sodium form. To make the resin more selective to contaminant cations, they are protonated using a strong mineral acid like sulphuric acid or hydrochloric acid.

A 10% H_2SO_4, 100 mL solution was used for this purpose. Deionised water was used to remove the co-ion (SO_4^{2-}, Cl^-) that accompanies the protons from the acid, as well

as other impurities and reduce ionic strength. The resin was then rinsed with pure 40% NH_4F, to maintain a similar pH and matrix conditions for the experiments. For the actual experiments, a 1 L solution of 40 % ammonium fluoride with a pH of 6.89 was absorbed in the resins until breakthrough of the copper. The flowrate was controlled at between 3 bedvolumes/hour and 10 bed volumes/hour. Sampling was conducted at every 10 bed volumes of liquid absorbed in resin. Figure 3.3 illustrates the process. In the case of the Pelchem sample, the resin was regenerated and reused.
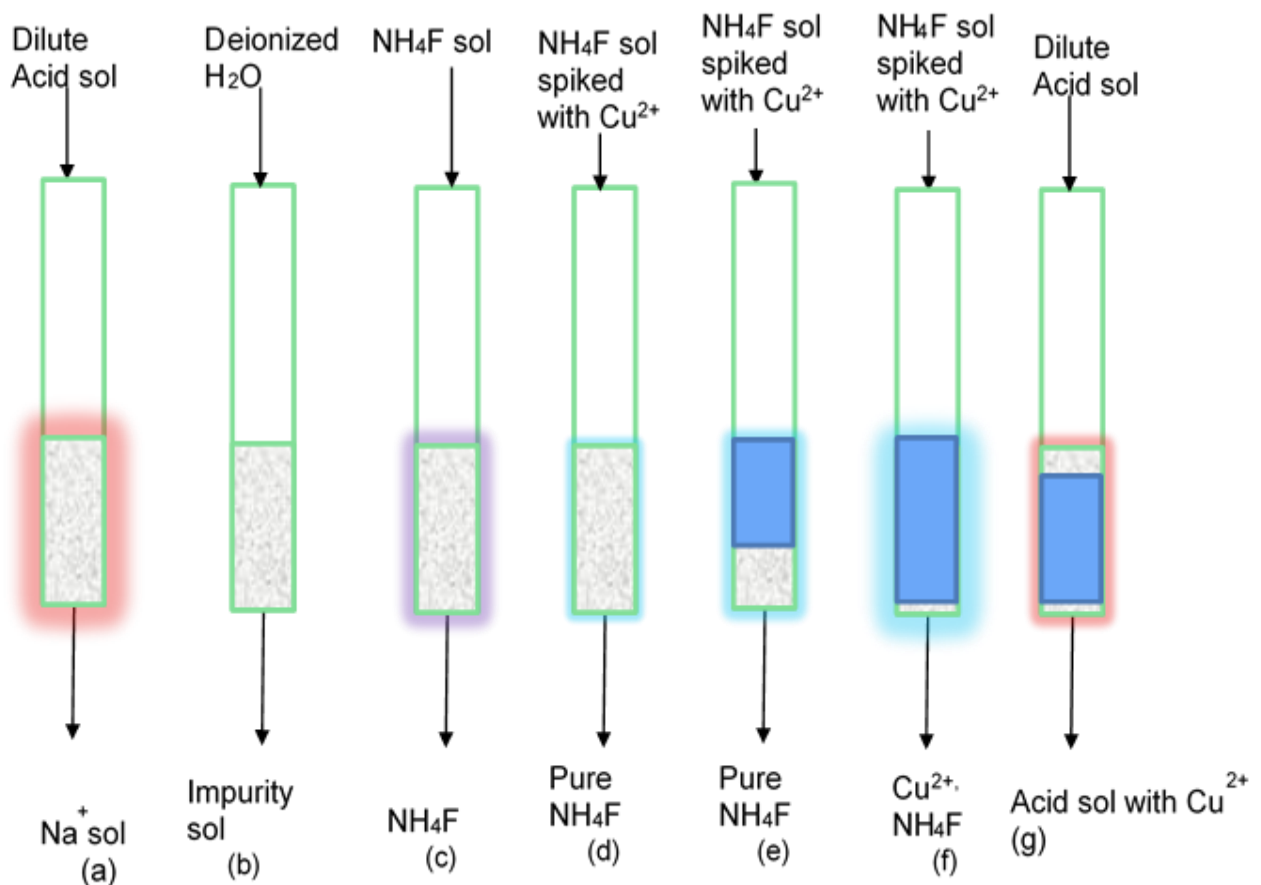
Figure 3.3: Cationic ion exchange resin operation: (a) Resin preparation. (b) Ionic strength reduction. (c) Resin rinsing. (d) - (e) Copper absorption. (f) Copper breakthrough. (g) Resin regeneration.

The Pelchem sample is a mixture of solid and liquid. 200 g of the sample were mixed with water. Gradually, ammonia water solution was added, resulting in some precipitation of cations. The concentrations of the cations were determined using standard addition. The method was chosen because sample matrix may be complex and unknown interferences may feature. Figure 3.4 to Figure 3.6 show the calibration

curves for the three cations of interest, the rationale for standard addition is explained in Appendix A2
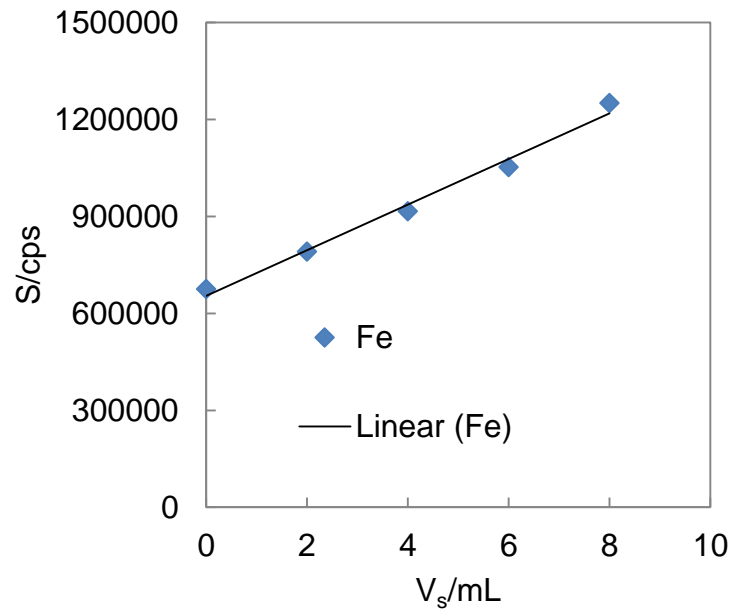

Figure 3.4: The standard addition method calibration graph for Fe. The quotient of the y-intercept to the slope is 9.26.
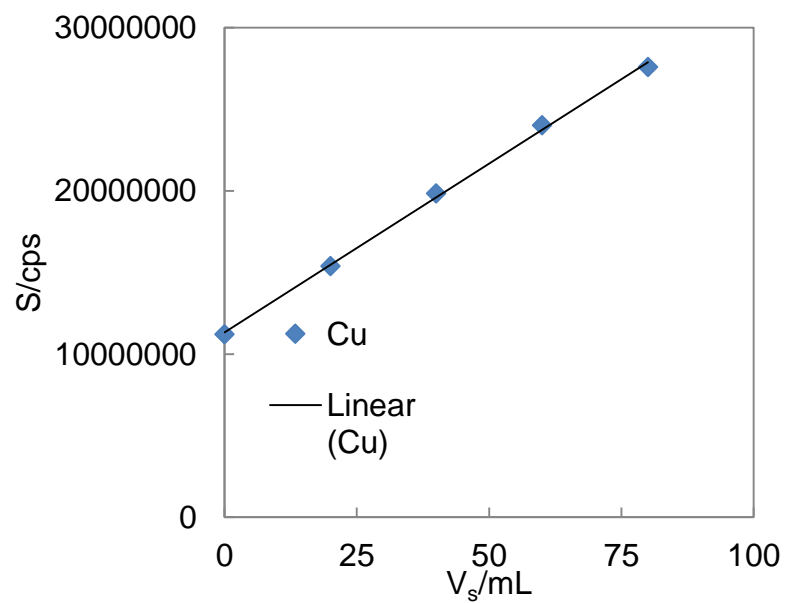

Figure 3.5: The standard addition method calibration graph for Cu. The quotient of the y-intercept to the slope is 54.71.

NH_4F|42
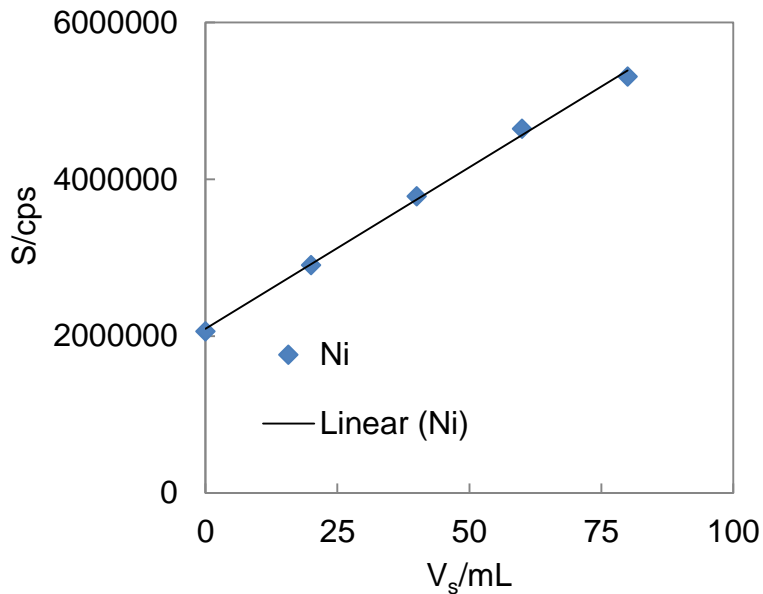
Figure 3.6: The standard addition method calibration graph for Ni. The quotient of the y-intercept to the slope is 50.84.

An amount of the sample was added to an equal amount of water in mass i.e. 500 g of the sample was added to 500 mL of water. The mixture was stirred to minimise the solid phase. After which, it was gradually neutralised to a pH of 6.8. This lead to precipitation of some of the metal cation contaminants. The solution was filtered and the precipitant collected. An attempt was made to identify the contents of the precipitants, but the XRD could not conclusively unmask the precipitate. Thermogravimetric analysis was used to reveal the dissociation temperatures of the chemical species that make up the precipitant. This can be seen in Figure 3.7. Three equal masses of 0.3 g of the Pelchem sample, were put in the oven at three different temperatures: from the results of the TGA, the temperatures were 190 ^{o}C, 270 ^{o}C and 500 ^{o}C for a minimum period of 24 hours. These were then analysed with XRD. The results are reported on section 4.4 of this text.
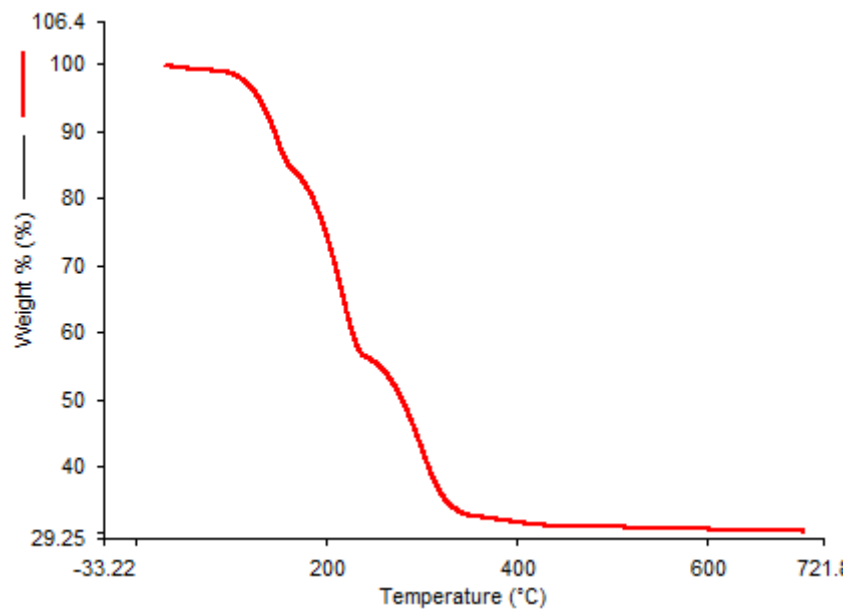
Figure 3.7: Dissociation temperatures for precipitate.

NH$_4$F|44

4 Results and discussion

4.1 Capacity of cationic resins for Cu^{2+}

Elution of Purolite S930Plus and Lewatit TP207 and calculating the sodium cation replaced with the proton from the acid, confirmed the manufacturers claim that the Lewatit as well as the Purolite have a capacity of 2 eq/L for monovalent cations (1eq/L for divalent cations). The useful capacity is a strong function of pH.

4.1.1 Capacity in $NH_4F.HF$

Table 4.1 shows the capacity of Purolite S930Plus to absorb Cu^{2+} in a matrix of 40% ammonium bifluoride. The durations of the reactions were at least 5 hours.

Table 4.1: Absorption of Cu^{2+} in $NH_4F.HF$ onto Purolite S930Plus.

Parameter	Rep.1	Rep. 2	Rep. 3	Average
Conc Cu^{2+} before reaction/ppm	790.5	694.9	936.0	807.1
Conc after reaction,Cu^{2+} /ppm	589.5	496.7	823.1	636.4
Capacity Cu^{2+}/eq/L	0.31	0.31	0.18	0.27
Standard deviation of capacity	0.08			

Lewatit TP207 performs marginally worse than Purolite in the absorption of Cu^{2+} in the $NH_4F.HF$ matrix. Table 4.2 displays these declinations. The reactions lasted for at least 7 hours.

Table 4.2: Absorption of Cu^{2+} in $NH_4F.HF$ onto Lewatit TP207.

Parameter	Rep. 1	Rep. 2	Rep. 3	Average
Conc Cu^{2+} before reaction/ppm	732.2	784.8	830.6	782.5
Conc after reaction,Cu^{2+} /ppm	589.2	642.8	621.8	617.9
CapacityCu^{2+}/eq/L	0.23	0.22	0.33	0.26
Standard deviation of capacity	0.06			

4.1.2 Capacity and selectivity coefficients in NH$_4$F

Ammonium fluoride at a concentration of 40%, is the desired product. Its pH is approximately 7. The calculation of the selectivity coefficient mimics the calculation of the equilibrium constant for ideal solutions. In the case of ammonium fluoride, the starting concentration is an invariant 887.5 ppm Cu^{2+}, this is 0.013966M. The capacities of the two resins is 2 eq/Lresin, 5 mL resin is immersed in 1 L solution. Hence the capacity in molar concentration unit is 0.01 M. For the experiment that resulted in the remaining concentration of 267.4 ppm Cu^{2+} (0.004208 M), after exposure to Purolite S930Plus, given that the reaction is a reversible reaction, the selectivity coefficient as per equation (2.12), at room temperature is

$$K = 4 \gg 1$$

The selectivity is significantly higher than unity, therefore the forward reaction is favoured. Hence it can be inferred that purification is thermodynamically possible. Table 4.3 summarises the capacity and selectivity coefficients for the purification of ammonium fluoride spiked with Cu^{2+} in Purolite S930Plus

Table 4.3: Absorption of Cu^{2+} in NH$_4$F onto Purolite S930Plus.

Parameter	Rep. 1	Rep. 2	Rep. 3	Average
Conc Cu $^{2+}$ before reaction/ppm	887.5	887.5	887.5	887.5
Conc after reaction,Cu^{2+} /ppm	267.4	321.2	308.2	298.9
CapacityCu^{2+} /eq/L	0.98	0.89	0.91	0.93
selectivity coefficient K	4.2	2.3	2.6	3.03
Standard deviation of capacity	0.04			
Std dev of selectivity coefficient	1.02			

The capacity of the Purolite S930Plus for the cation increases markedly with the pH: the average capacity for Cu^{2+} of the Purolite S930Plus in a NH$_4$F.HF matrix is 0.27 eq/L, in a NH$_4$F matrix, it is 0.93 eq/L. This is not that far from the maximum capacity of the resins which is 1 eq/L, for divalent cations. Lewatit TP207 has an even

higher capacity, and the standard deviation for capacity and selectivity coefficients are lower. These improvements can be seen on Table 4.4.

Table 4.4: Absorption of Cu^{2+} in NH_4F onto Lewatit TP207.

Parameter	Rep. 1	Rep. 2	Rep. 3	Average
Conc Cu $^{2+}$ before reaction/ppm	887.5	887.5	887.5	887.5
Conc after reaction,Cu^{2+} /ppm	266.1	266.65	299.1	277.27
CapacityCu^{2+}/eq/L	0.98	0.98	0.93	0.96
selectivity coefficient K	4.3	4.2	2.9	3.80
Standard deviation of capacity	0.03			
Std dev of selectivity coefficient	0.78			

4.2 Observed kinetics versus diffusion rate

The purification of ammonium fluoride off copper (II) cation, in terms of power law kinetics is represented by equation (2.15). Equation (2.19) is used for determination of the effective diffusivity. Additionally, the Weisz-Prater criterion is computed from equation (2.20). Figure 4.1, Figure 4.2 and Figure 4.3 display the data for 30 ºC, 50ºC and 65ºC respectively. The controlling step of the reaction is the intraparticle diffusion.
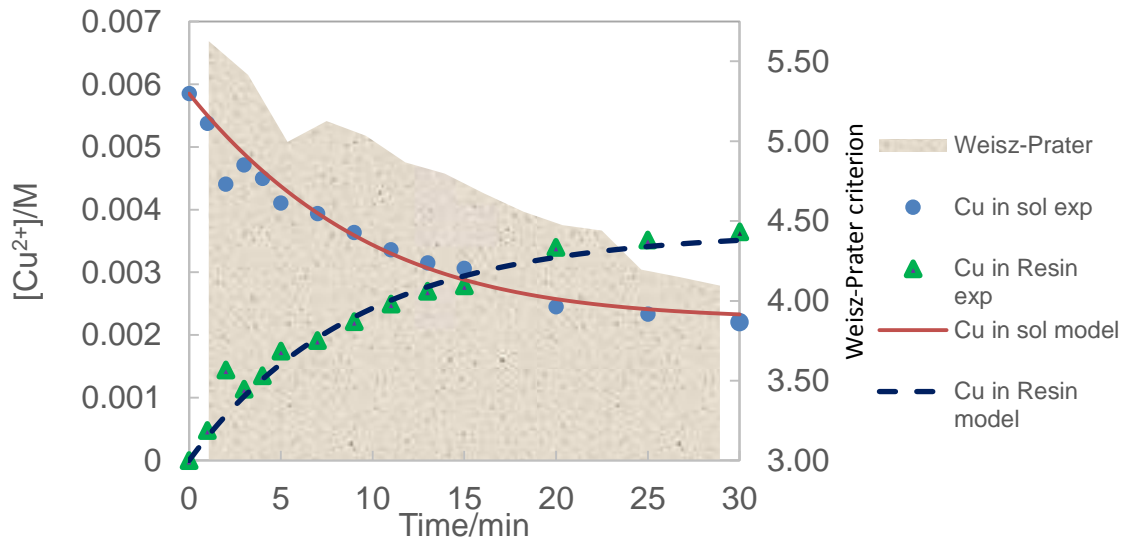
Figure 4.1: The concentration profile for Lewatit TP207 at 30 °C. The right-hand side ordinate axis is the Weisz-Prater criterion.
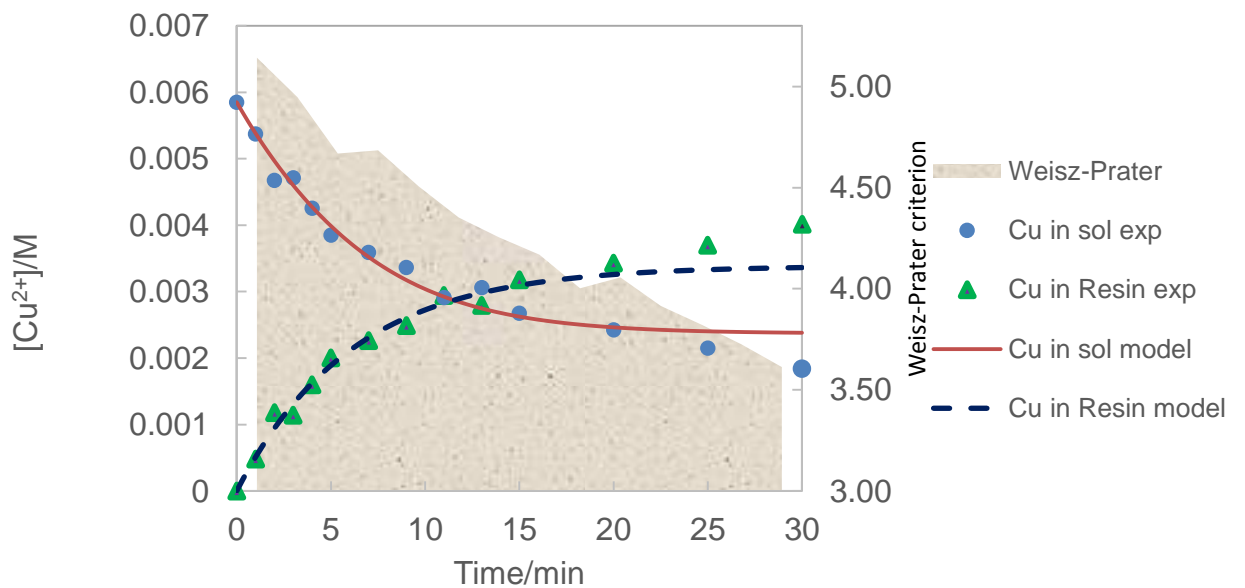

Figure 4.2: The concentration profile of $Cu^{2+}(aq)$ on Lewatit TP207 at 50 °C.
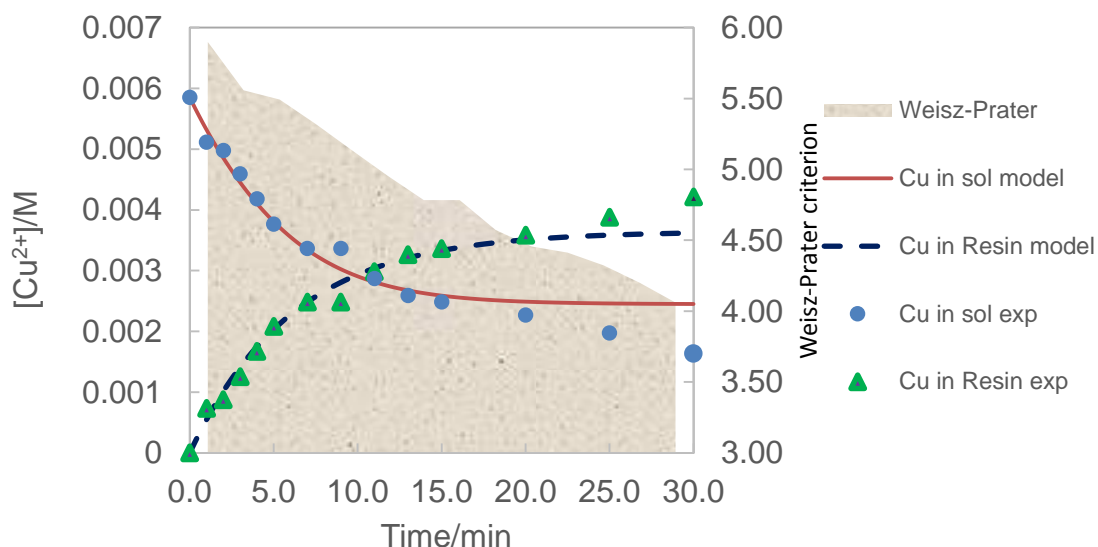
Figure 4.3: The concentration profile of Cu^{2+}(aq) on Lewatit TP207 at 65 ^{o}C

Generally low percentage errors with regard to the integration, albeit with relatively high standard deviations are achieved. The average percent error for the reaction rate integration, is 4.2%. In the case of the diffusivity, it is higher.

Table 4.5 shows the average of the triplicate parameters for Lewatit resin at three temperatures.

Table 4.5: Lewatit observed reaction and internal diffusion parameters.

Temperature/^{o}C	k'_{avg}/Lsol^2· min^{-1}·mol^{-2}	$K_{eq,avg}$	$D_r \times 10^9$/m^2·min^{-1}
30	19	23	0.67
50	32	26	1.24
65	52	28	1.68

The same exercise is repeated for the Purolite resin. Figures Figure 4.4, Figure 4.5 and Figure 4.6 display the graphs for Purolite S930Plus at 65 ^{o}C, 50 ^{o}C and 30 ^{o}C, in that order.
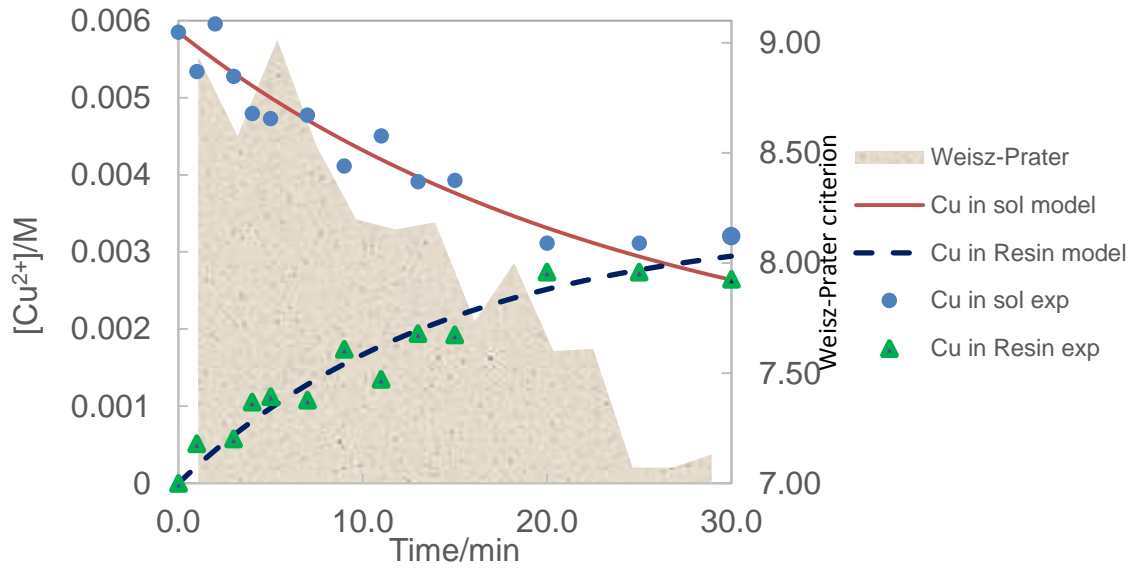
Figure 4.4: The concentration profile of Cu^{2+}(aq) on Purolite S930Plus at 65 °C.

For both resins, the Weisz-Prater criterion is much larger than unity at all temperatures. Comparatively, internal mass transfer limitations are much more pronounced with the Purolite Resin. Table 4.6 records the average parameters. For the two resins, the reaction parameters determined at different temperatures are used to ascertain the reaction kinetics. This involves plotting the inverse of the absolute temperatures against the natural logarithm of the reaction rate constant and equilibrium constant. In the case of the equilibrium constant, for the two resins, Figure 4.7 demonstrates the plot.
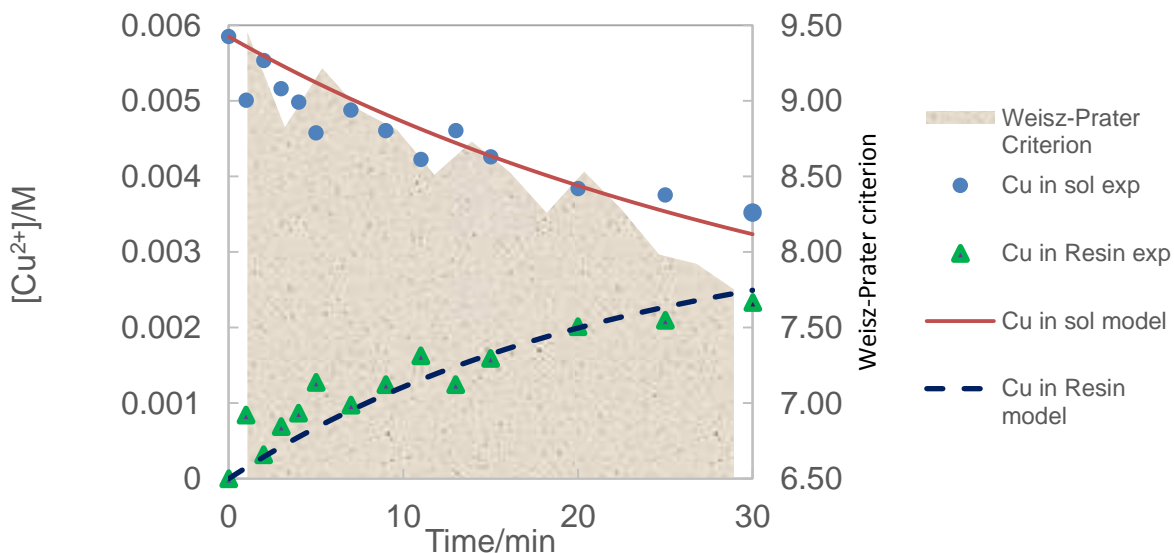
Figure 4.5: The concentration profile of Cu^{2+}(aq) on Purolite S930Plus at 50 °C.
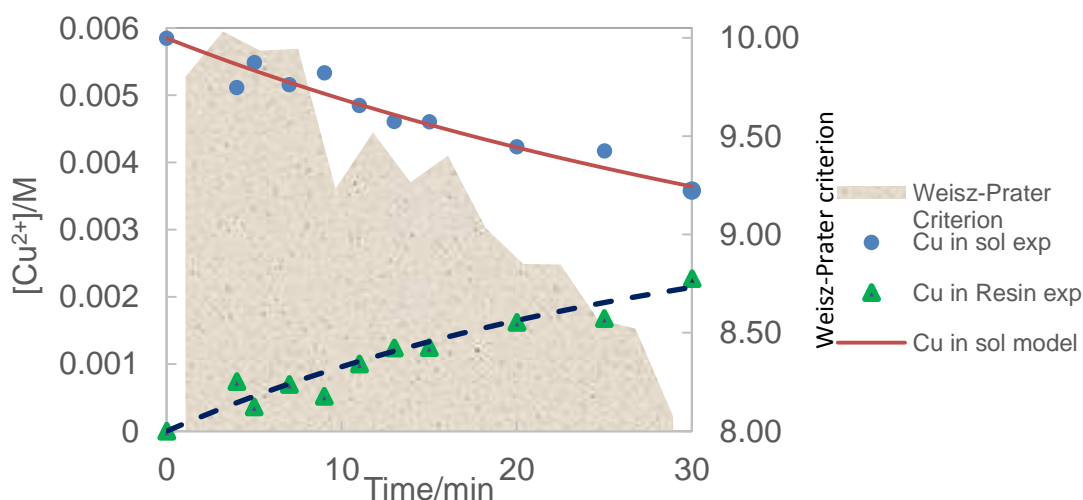
Figure 4.6: The concentration profile of Cu^{2+}(aq) on Purolite S930Plus at 30 °C.

Similarly, the natural logarithm of the reaction rate constants at the three temperatures is plotted against the inverse of absolute temperature. Figure 4.8 illustrates the plot. In order to establish the temperature dependency of the diffusivity in the resins, a pseudo-Arrhenius plot is drawn. Figure 4.9 is an embodiment of such a plot. Using information gleaned from the respective graphs, the reaction parameters can be established. These are summarised on Table 4.7.

Table 4.6: Purolite observed reaction and diffusion parameters.

| Temperature/^{o}C	k'$_{avg}$/Lsol$^2\cdot$ min$^{-1}\cdot$mol^{-2}	K$_{eq,avg}$	Dr$\times10^{10}$/m$^2\cdot$min^{-1}
30	7.5	2	1.56
50	10	3.7	2.02
65	13.7	6	2.75
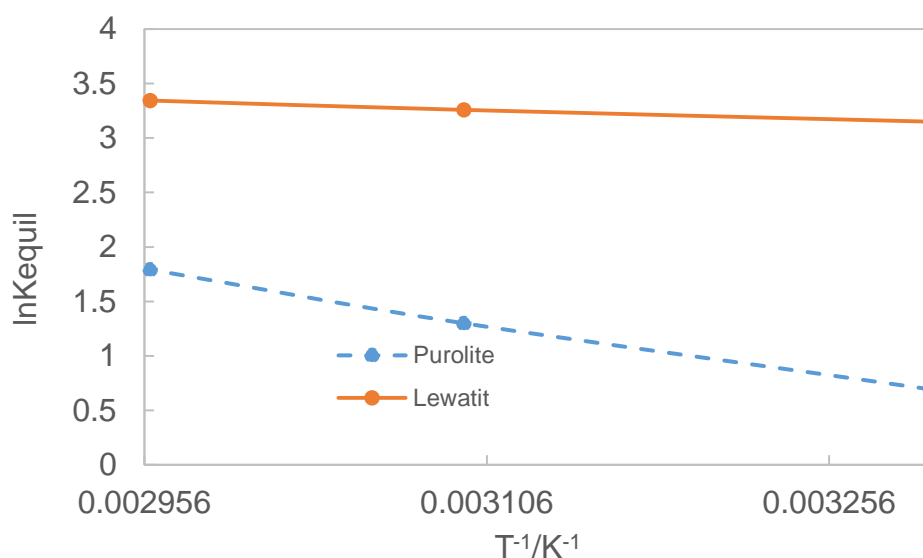
Figure 4.7: The Van't hoff plot for the two resins' (R^2 = 0.9978 for Lewatit, R^2 = 0.9972 for Purolite).

In a nutshell, the reaction of copper (II) cations is an endothermic process. Although relatively low total percentage errors between the integration and experimental results are achieved in the analysis of the reaction rate constants, non-negligible standards of deviation for the triplicate experiments result.
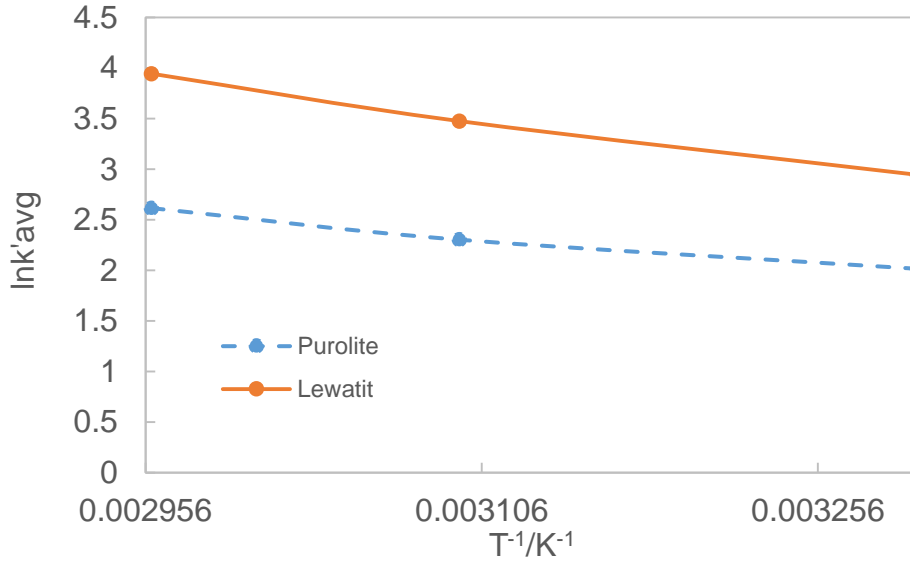
Figure 4.8: The Arrhenius plot for the two resins' (R^2 = 0.9942 for Lewatit, R^2 = 0.9815 for Purolite).
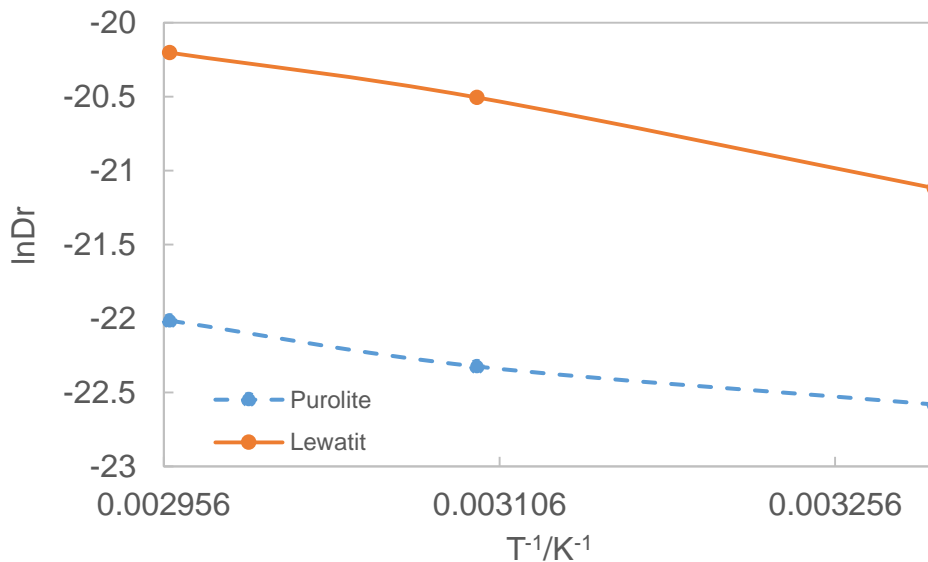

Figure 4.9: The pseudo-Arrhenius plot of the diffusivities (R^2 = 0.9724 for the Purolite, R^2 = 0.9935 for the Lewatit).

Tentatively, it can be inferred that mass transfer limitations play a role, or perhaps the dominant role in the purification reaction. This could be due to the irregular nature of the resin structure and the tortuous path that the counter-ions travel. This can be qualitatively demonstrated by analysis of scanning electron microscopy pictures.

Table 4.7: Reaction parameters for $Cu^{2+}(aq)$ with Lewatit and Purolite

Parameter	Purolite S930Plus	Lewatit TP207
$E/J{\cdot}mol^{-1}$	14 368	24 116
$k_o'/L^2{\cdot}min^{-1}{\cdot}mol^{-2}$	2 213	269 682
$-\Delta H_{rx}/J{\cdot}mol^{-1}$	-26 555	-4 696
K_{eqo}	75 057	150
$E_p/J{\cdot}mol^{-1}$	13 527	22 486
$D_{ro}{\times}10^8/m^2{\cdot}min^{-1}$	3.29	517.9

Figure 4.10 shows the SEM pictures for virgin or unused Lewatit TP207 and virgin Purolite S930Plus, respectively. The two resins appear to be dense, with very limited porosity. Indeed, BET analysis revealed that the surface area of both resins is quite small. In the case of Lewatit TP207, it is 10 m^2/g. Purolite S930Plus has a surface area of 14 m^2/g.

As can be seen on Figure 4.10 (a), Lewatit TP207 has a much more pronounced cavity which runs along the circumference of the pellet. This cavity appears to be filled when the resin is used by absorbing Cu^{2+}. This is can be seen on Figure 4.10 (c). There appears to be no observable differences in the used Purolite and the virgin, comparing (d) to (b). Scrutinising the resin pellets, it appears that the resins have nanometre-size pores. Figure 4.11 is illustrative of that. No significant changes between the used and the virgin resins are detected.
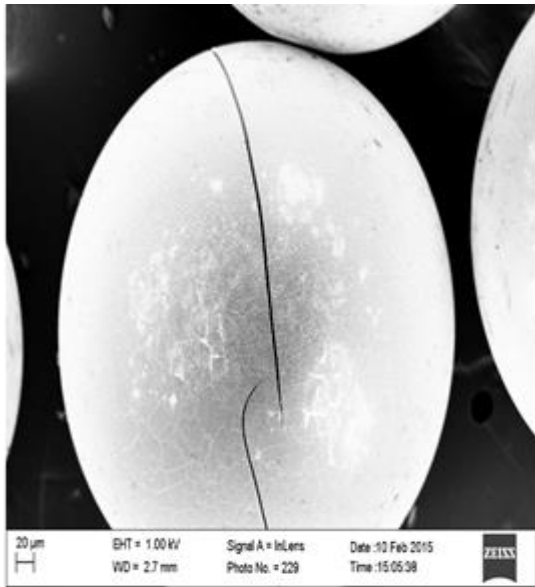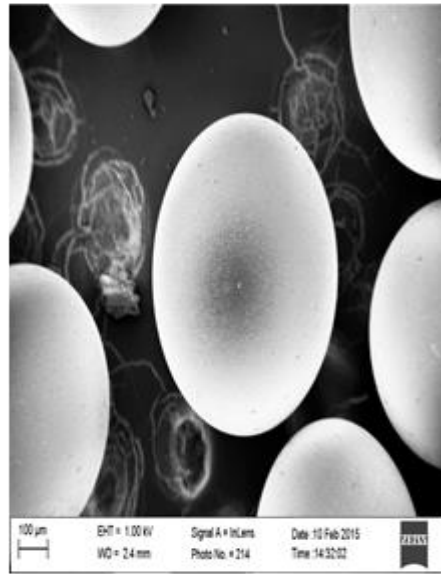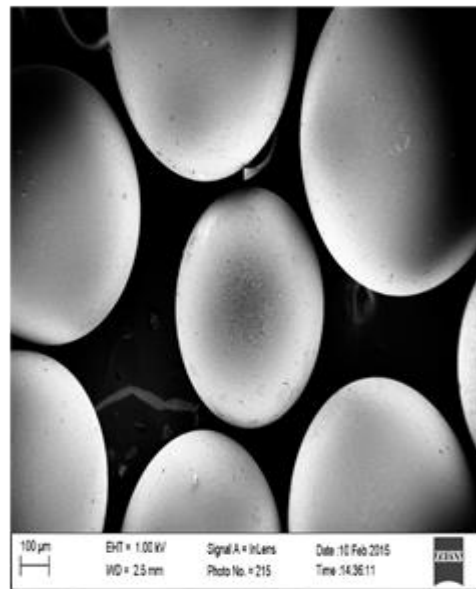
Figure 4.10: (a) Virgin Lewatit TP207. (b) Virgin Purolite S930Plus. (c) Used Lewatit TP207. (d) Used Purolite S930Plus.
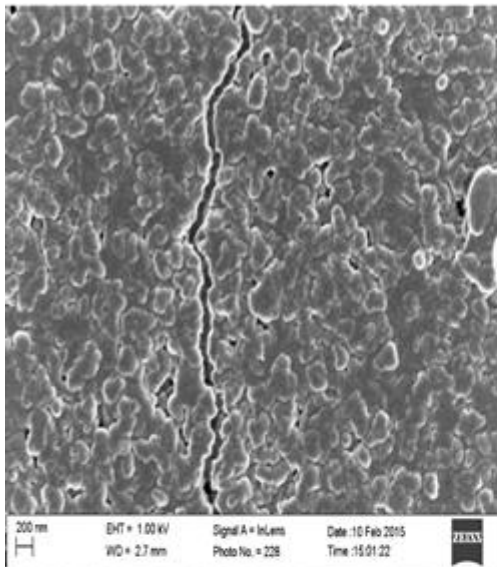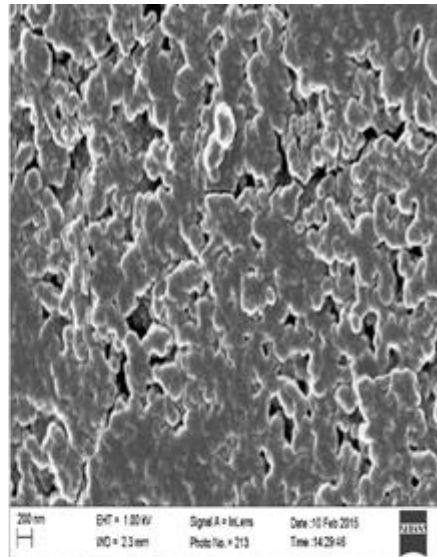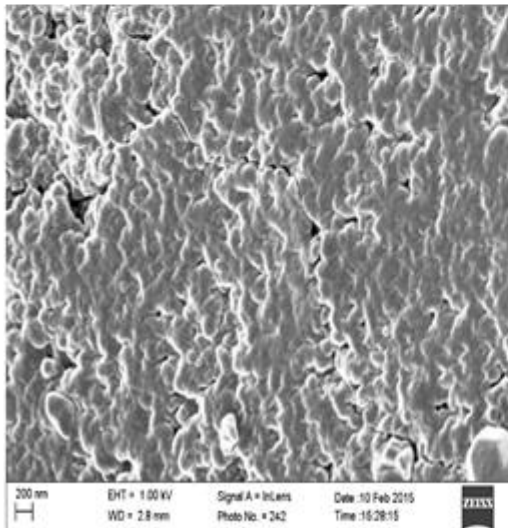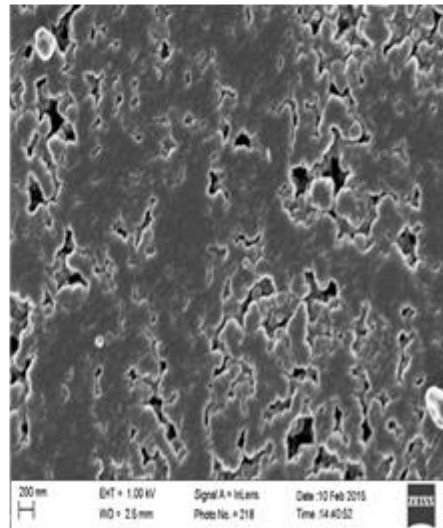
Figure 4.11: (a).Magnified virgin Lewatit TP207. (b) Magnified virgin Purolite S930Plus. (c) Magnified used Lewatit TP207. (d) Magnified used Purolite S930Plus

Considering the Weisz-Prater criterion and the SEM pictures, it can be conclusively deduced that intraparticle diffusion is the limiting step of the reaction. It can be plausibly assumed that the apparent kinetics do not change much when a flow type reactor, rather than batch is used, to ascertain the parameters In this regard equation (2.18) is used to determine the equilibrium conversion.

When the equilibrium temperature is 25 ^{o}C, $x_e = 0.56$ for Lewatit, and 0.41 for Purolite. This is too low in relation to the observed conversion in the two resins. Moreover, the equilibrium constants obtained using least square fitting are physically unrealisable. This represents the limitations of mathematical depiction of reality necessitating engineering judgement.

In the case of the equilibrium constant, the Adams method for the integration, is used instead of the more popular Euler or the Runge Kutte methods. It has predictor-corrector components, which makes it ideal for the current application. To eliminate the possibility of physically unrealisable equilibrium constants, manual fitting of the curves is favoured rather than least squares fitting.

It is instructive to keep in mind that the hydronium ion, has a very low residence time as it is part of the mobile phase. On the contrary, the other product is part of the stationary phase. In accordance with Le Chatelier's, the forward reaction is strongly favoured. The reaction lies so far to the right, such that for all practical purposes, it may be considered to be an irreversible reaction, hence the backward reaction may be momentarily cast away in the modelling of the kinetics.

If the reaction is considered to be second order with regard to capacity (-COOH) and is second order to copper cation concentration, the integration results in an improvement in the estimation of the experimental data, contrary to the forward only elementary reaction orders. Figure 4.12 illustrates the integration results relative to the experimental results of the kinetic experiments for Lewatit TP207 at a temperature of 50 ^{o}C. The apparent reaction rate constant is 7000 $L^3 \cdot min^{-1} \cdot mol^{-3}$.

Table 4.8 demonstrates the reaction parameters at three temperatures, for Lewatit TP207 and Purolite S930Plus, respectively. Comparing the two resin's reaction dynamics at 50 ^{o}C, it can be deduced that the Purolite has a reaction rate constant that is almost three times as small as that of its counterpart. Given that the rate orders for the Purolite and the Lewatit are the same, apparently the Lewatit is more sensitive to the copper (II) cation, hence it reacts at a faster rate than Purolite.
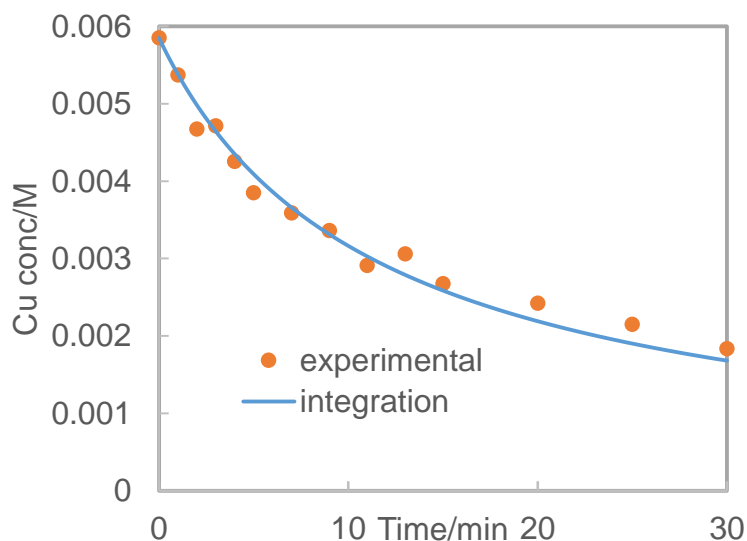
Figure 4.12: The concentration profile for Lewatit TP207 at 50 °C. Total percentage error is less than 5%.

Table 4.8: Average reaction rate constants. The reaction is 2nd order to the two reactants.

Temp/°C	Lewatit TP207 k'_{avg}/ $L^3 \cdot min^{-1} \cdot mol^{-3}$	Purolite S930Plus k'_{avg}/$L^3 \cdot min^{-1} \cdot mol^{-3}$
30	3 933.3	1 502.7
50	6 550	2 243.3
65	8 166.7	2 789.7

The apparent reaction rate constants for Lewatit TP207-Cu^{2+} and Purolite S930Plus-Cu^{2+} in 40% ammonium fluoride, at three temperatures, 30 °C, 50 °C and 65 °C have been determined. This allows for the estimation of the pre-exponential constants, as well as the activation energies for the resin-Cu^{2+} systems. Figure 4.13 shows the graphical embodiment of the linearized Arrhenius equation to that effect. The mean of all the triplicate results for the apparent reaction constant was used.
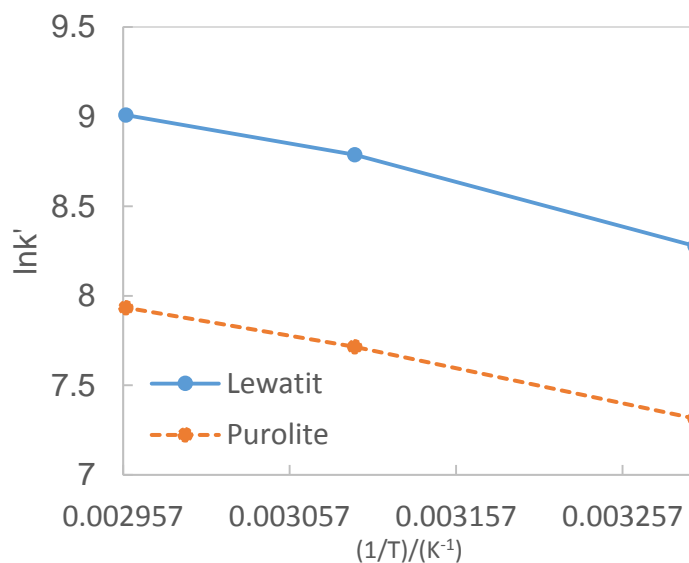
Figure 4.13: The natural logarithm of the apparent reaction rate constant against the inverse of temperature, R^2 = 0.9875 for Lewatit and 0.9968 for Purolite.

Evaluating the activation energies from the slopes of Figure 4.13 and the pre-exponential constants from the ordinates of the afore-mentioned graph, allows for the tabulation of the results on Table 4.9.

Table 4.9: Apparent rate constant for Lewatit TP207 at 50 °C.

Parameter	Purolite S930Plus	Lewatit TP207
$E/J \cdot mol^{-1}$	15 140.0	17 994.5
$k_o'/ L^3 \cdot min^{-1} \cdot mol^{-3}$	619 086.3	5 091 077.2

4.3 Breakthrough curves

Figure 4.14 demonstrates the purification of water spiked with 581 ppm Cu^{2+}.
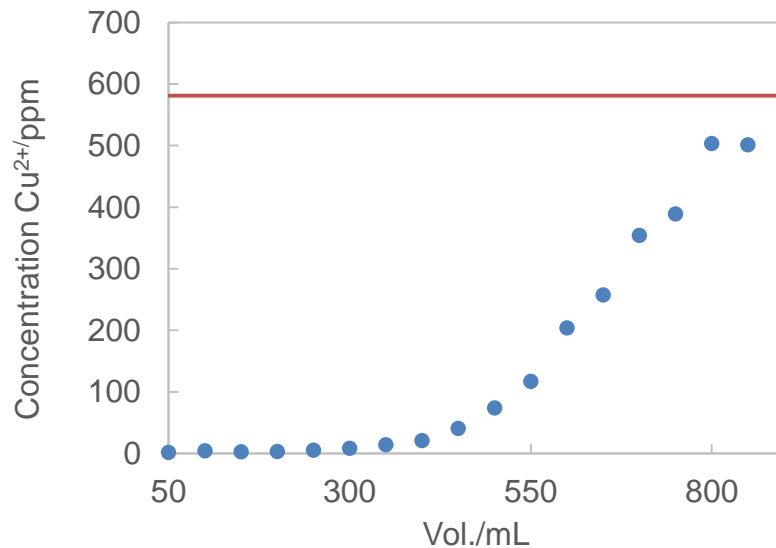

Figure 4.14: Breakthrough curve of Cu^{2+} in water, Lewatit TP207 resin. The flowrate is 100 mL/hr.

Breakthrough of the cation ion only occurs at a volume 350 mL collected. When the solution matrix is changed to 40 % NH_4F rather than pure water, breakthrough occurs at a lower volume. Albeit, at a higher concentration of 887.5 ppm Cu^{2+}(aq), Figure 4.15 is illustrative of this in the case of the Lewatit resin.

For the integration, the effective reaction constant is 2.78×10^{13} $m^9day^{-1}mol^{-3}$. In its constitutive parts it is:

$$k'_{eff} = G_{corr} \left(\frac{1}{D_{ro}}\right)^2 k' = 1.5 \times 10^5 \left(\frac{1}{5.18 \times 10^{-6}}\right)^2 0.0049655.$$

As per equation (2.24), the modified Euler-type integration in the bed, is:

$$[Cu^{2+}](i,j) = \sum_{i=0}^{m} \sum_{j=0}^{n} [Cu^{2+}](i,j) - 7.87$$

$$\times 10^{-18} \langle 9.17 \times slope(i,j) + 2.78 \times 10^{13} [Cu^{2+}](i,j)[COOH]^2(i,j) \rangle$$

$$[Cu^{2+}](t,z) = \begin{cases} 0, & [Cu^{2+}](i,j) < 0.017 \\ [Cu^{2+}](i,j) + 3^{11}z^{3.95}, & [Cu^{2+}](i,j) \geq 0.017 \end{cases}$$
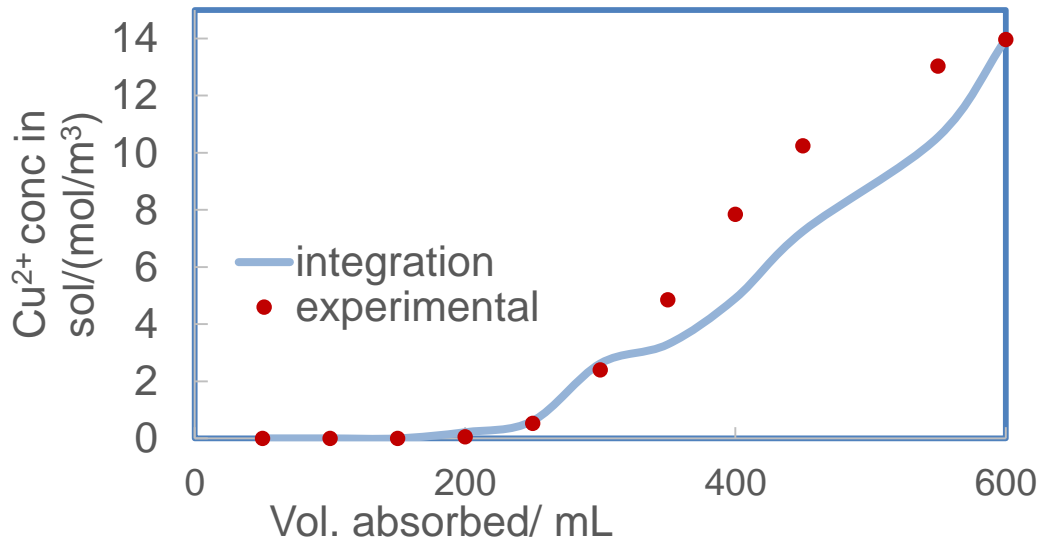
Figure 4.15: Breakthrough curve of Cu^{2+}(aq) in Lewatit TP207. The matrix is 40% ammonium fluoride solution.

The dimensionless characteristic breakthrough curve for Lewatit TP207, based on experimental results, is drawn on Figure 4.16. If the design concentration capacity is 0.85, as per Figure 4.16 the dimensionless time is 0.78.
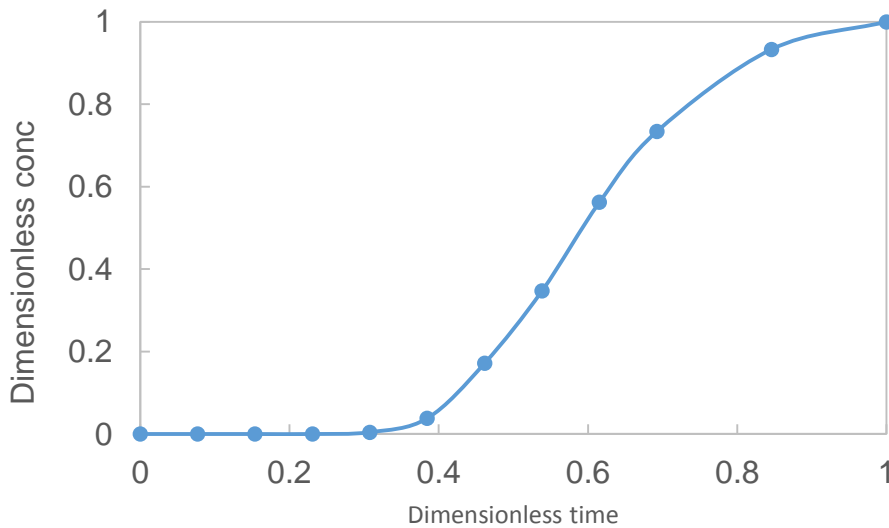
Figure 4.16: The breakthrough characteristic curve for Lewatit TP207 at a flowrate of 6 BV/hr. Breakthrough occurs at time 0.33.

In the case where the concentration of the diatomic cations is 50 ppm for $Fe^{2+}(aq)$, 120 ppm for $Ni^{2+}(aq)$ and 200 ppm for $Cu^{2+}(aq)$, the overall feed concentration is 370 ppm diatomic cation $M^{2+}(aq)$.

The concentration at capacity of the resin, is the product of the dimensionless design concentration at capacity and the feed concentration. If the design concentration at capacity is specified at 85%, the concentration at capacity is 314.5 ppm.

If in the aim of ensuring that there are no mass transfer limitations, the flowrate is pegged at 5 Bed Volumes/hour (BV/hr) i.e. at a flowrate lower than the one used to generate the breakthrough curve, the time it will take to reach saturation for the resin is as per equation (2.25), is 38.65 hr/Lresin. From Figure 4.16, breakthrough occurs at 33.4% of the time it will take to reach saturation of the resin; 13.1 hr/Lresin.

4.4 Actual Cu, Ni and Fe contaminated sample

The ammonium acid fluoride sample from Pelchem is a thick slurry. A 1:1 dilution with water makes it malleable to analysis. Figure 4.17 shows the potential difference of the fluoride as a function of fluoride concentration, prepared.

$$y = -53.75x + 81.283$$
$$R^2 = 0.9983$$
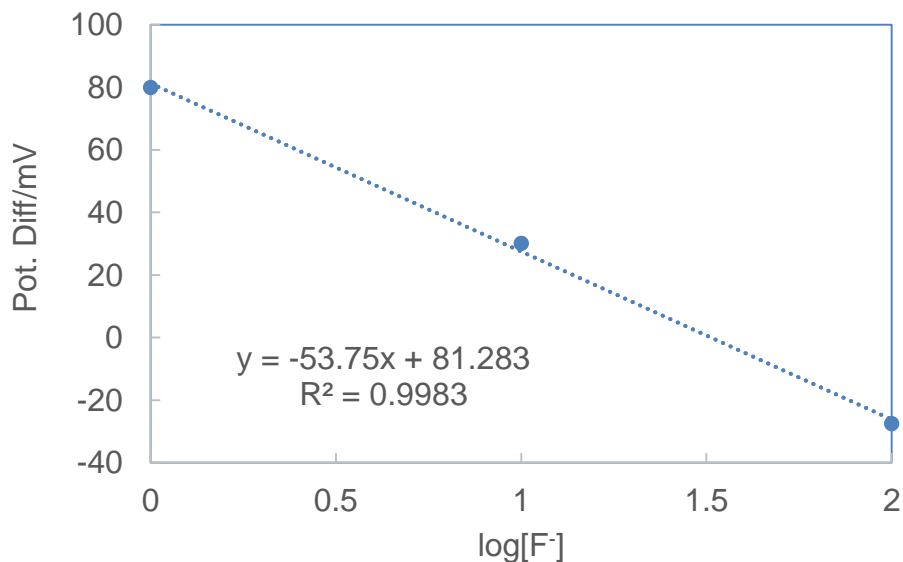
Figure 4.17: The potential difference of a NaF solution as a function of the decimal logarithm of fluoride concentration.

The potential difference in the 1:1 diluted sample, is 2.9 mV. The linear interpolation from the trend line reveals the concentration of the ammonium fluoride to be 56 %.

Using the standard addition method on the prepared solution, revealed that the prepared solution contains 60.5 ppm Fe (II) cation, 1786.7 ppm Cu (II) cation and 1660.2 ppm Ni (II) cation. Given that the solutions were prepared by diluting 15.31 g of ammonium acid solutions to 50mL with water, the concentrations of the cations in the untreated sample are given in Table 4.10.

Table 4.10: Concentration of cations in the ammonium acid fluoride

Cation	Concentration/ppm
Fe	197.5
Ni	5422
Cu	5835

Addition of ammonia water solution significantly decreases the solubility of the cations in the ammonium acid solution prepared by diluting to 50 mL with water. When 50 mL ammonia water is added, the solution decreases from 60.5 ppm Fe^{2+} concentration to 8.9 ppm. Ni^{2+} decreases from 1 660.2 ppm to 161 ppm, Cu^{2+} decreases from 1 786.7 ppm to 225 ppm. Further addition of the ammonia water results in relatively smaller amount of precipitation. Figure 4.18-Figure 4.20 displays this.
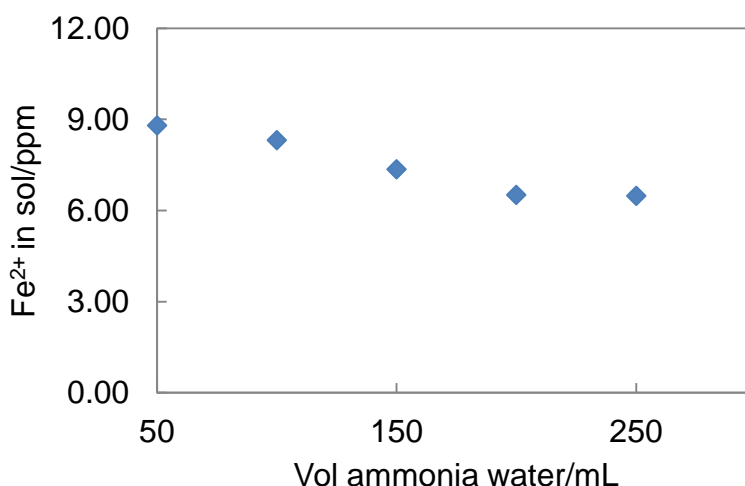

Figure 4.18: The precipitation of Fe^{2+} from ammonium acid fluoride sample. At about 175 mL ammonia water added, the solubility of Fe^{2+} stabilizes.
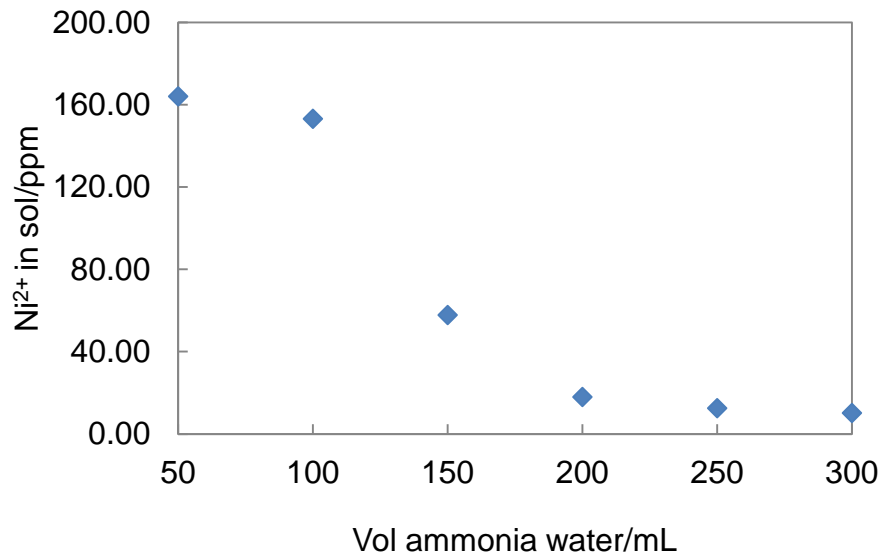
Figure 4.19: The precipitation of Ni^{2+} from ammonium acid fluoride solution. At about 200 mL ammonia water added, the solubility of Ni^{2+} stabilizes.

The addition of only 50 mL of ammonium water, results a significantly larger decrease in solubility of the cations than the addition of the subsequent 250 mL ammonia water solution. On addition of the 250 mL, Fe^{2+} solubility on decrease from about 8.9 ppm to 6 ppm. Cu^{2+} shows are larger decrease: from 225 ppm to about 120 ppm. The largest decrease is apparent in Ni^{2+}: from 161 ppm to 20 ppm.

Figure 4.21 shows the XRD diffraction pattern of the precipitate. The phases that are readily identifiable are ammonium fluoride as well as ammonium bifluoride. The other components in the precipitate are not conclusively unmasked. When the precipitate is heated to a temperature of 190 ºC, and analysed with a diffractometer, a nickel-copper fluoride hydrate type compound is unveiled as a component of the precipitate.

When the precipitate is heated to 270 ºC, the water is driven off and a nickel-copper oxide compound remains. Figure 4.22 shows this. This compound retains its stability to even temperatures exceeding 500 ºC. This is shown on Figure 4.23-Figure 4.24.
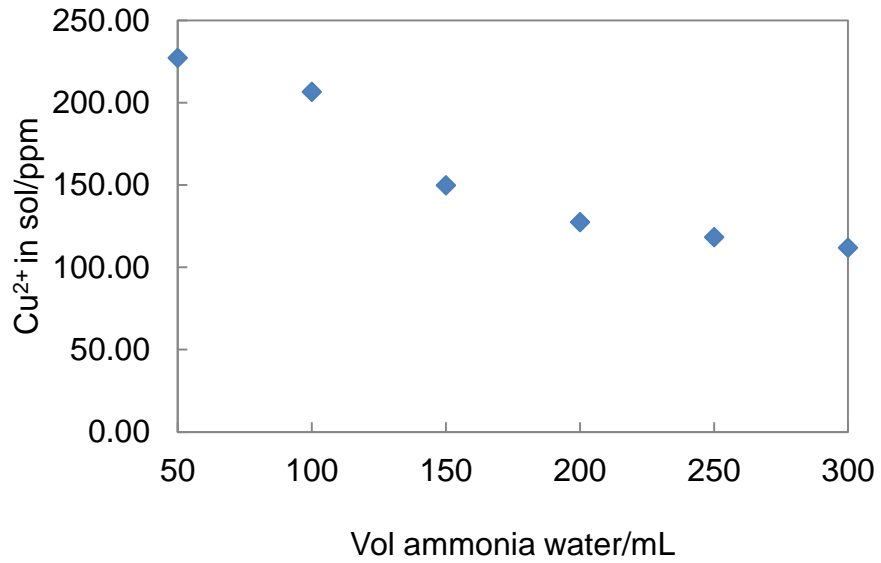
Figure 4.20: The precipitation of Cu^{2+} from ammonium acid fluoride solution. At about 200 mL ammonia water added, the solubility of Cu^{2+} stabilizes.
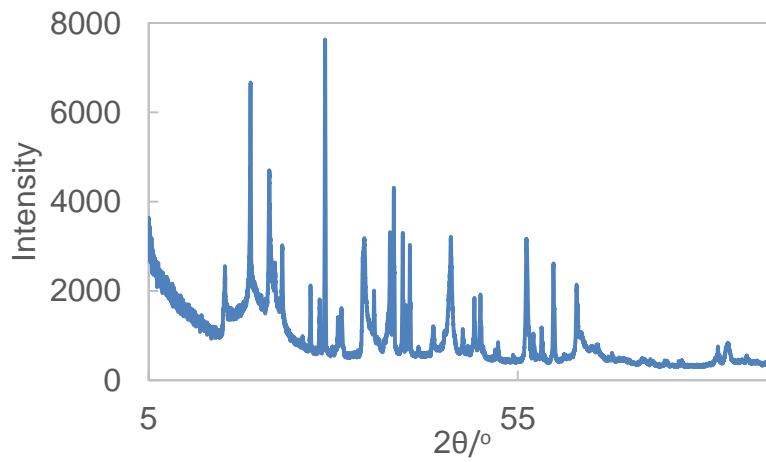
Figure 4.21: X-ray diffraction profile of precipitate.
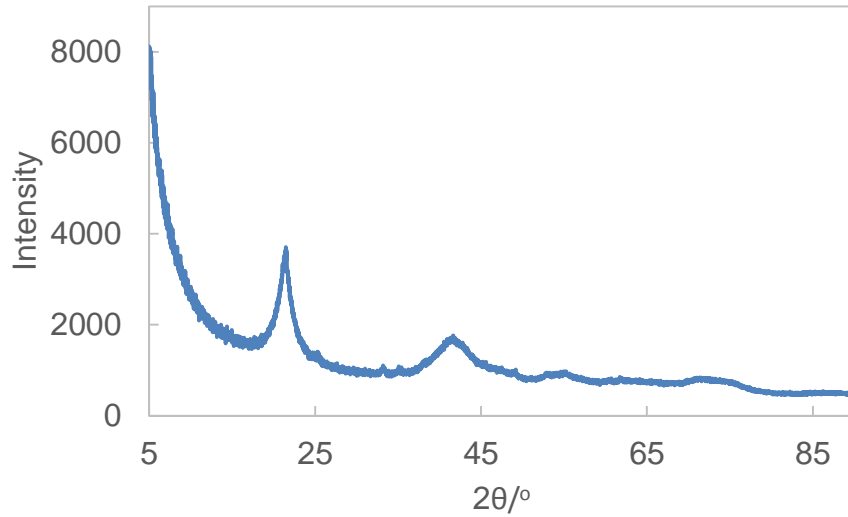
Figure 4.22: Nickel-copper fluoride hydrate maxima in precipitate.
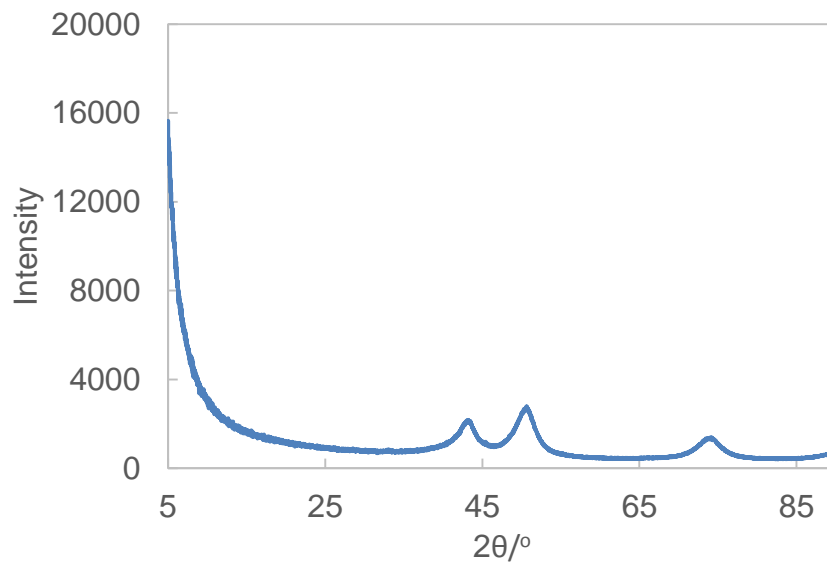
Figure 4.23: Nickel-copper oxide maxima. The precipitate was heated to 270 $^{\circ}$C.
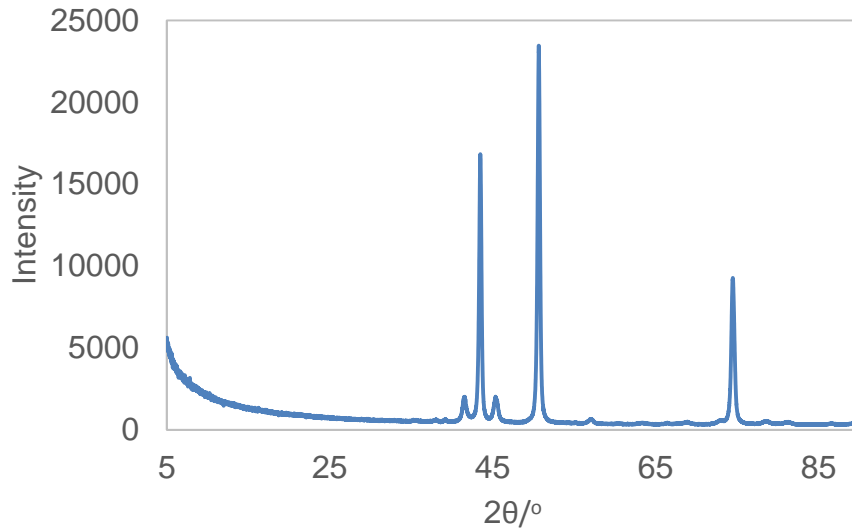
Figure 4.24: Nickel-copper oxide XRD pattern at 500 °C. The maxima is much more clearly defined.

After precipitation, the remnant cations can be absorbed by ion exchange resins. Thus for a 40 % NH_4F solution, Figure 4.25-Figure 4.27 shows the effectiveness of Lewatit TP207 versus Purolite S930Plus in for $Fe^{2+}(aq)$, $Ni^{2+}(aq)$ and $Cu^{2+}(aq)$ contamination respectively. Analysing the results from all three cations, Purolite consistently performs worse than Lewatit TP207. These results have been achieved at a flowrate of 20 BV/hr.
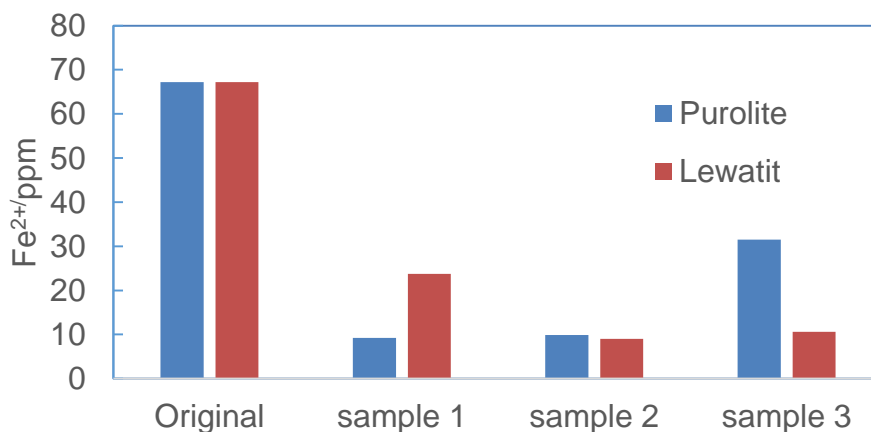
Figure 4.25: Iron cation absorption in Lewatit TP207 and Purolite S930Plus. The performance of the two resins is bad, Purolite in overall terms, is worse.
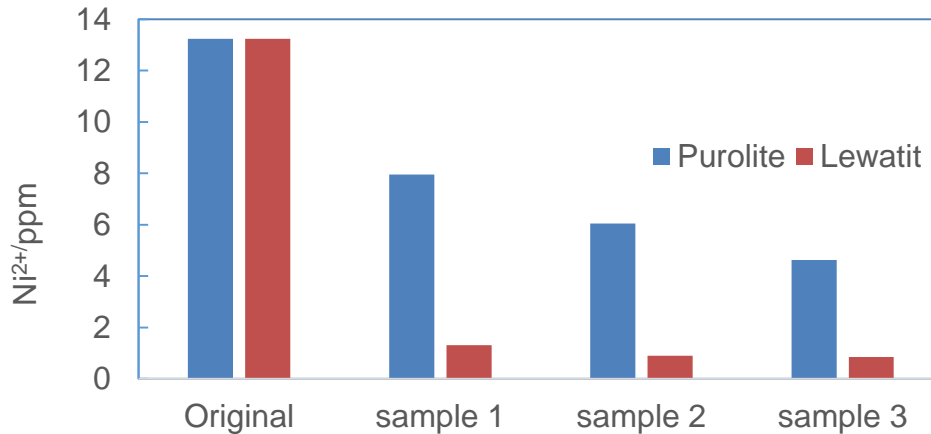
Figure 4.26: Nickel cation absorption in Lewatit TP207 and Purolite S930Plus. The Lewatit resin performs much better than the Purolite resin.
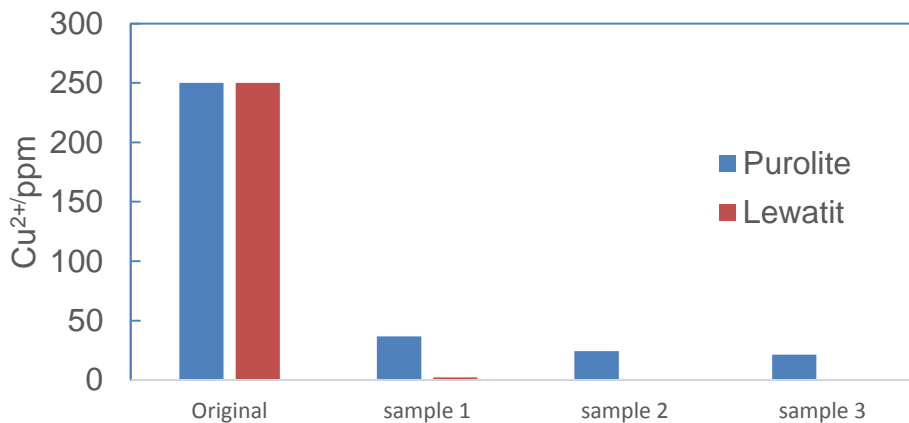
Figure 4.27: Copper cation absorption in Lewatit TP207 and Purolite S930Plus. In keeping with the trend, Lewatit performs better.

Iron (II) cation is the one contaminant in the ammonium fluoride solution, which is not appreciably absorbed by the ion exchange resins. Even the Lewatit resin has a poor performance regarding the absorption of Fe^{2+} (aq). This is not surprising given the coordination chemistry involved in the complex formation process through which the absorption occurs: Fe^{2+} (aq) is predicted to be the least likely transition cation to form a complex. The presence of Fe^{2+} (aq) is predominantly due to the steel drums; wherein the ammonium acid fluoride is stored, rather than the corrosion of Monel material of construction. To demonstrate this, some portions of the ammonium acid fluoride slurry contain very little or no detectable Fe^{2+}(aq) cations, whilst they contain the other two cations. This is because the slurry is not well mixed; the concentration of the cations

is highly dependent on the position of the sampling. Table 4.11 demonstrates this and the concentration of the solution after absorption on the Lewatit resin.

Table 4.11: <u>Absorption of neutralised Pelchem sample with Lewatit TP207.</u>

40% NH_4F	Concentration(ppm)		
	$Fe^{2+}(aq)$	$Ni^{2+}(aq)$	$Cu^{2+}(aq)$
Original solution	0	144	923
Sample 1	0	0	0
Sample 2	0	0	0
Sample 3	0	0	0

4.5 Design aspects

The objective of the design is to provide a viable method in the treatment of ammonium acid fluoride slurry, produced as a by-product in an NF_3 process. The desired product is 40 % NH_4F (aq). This implies that the acid fluoride must be neutralised. There is only one truly viable method of neutralising ammonium acid fluoride to 40 percent ammonium fluoride: ammonia. In the liquid phase, ammonia is available commercially as 25 % NH_3 (aq). The ammonium acid fluoride has an average concentration of 56 percent NH_4F. Since the desired concentration of the solution is 40 percent ammonium fluoride, the ammonia water neutralisation route is inacceptable as it is too dilute. Instead, ammonia gas is used. Given the NF_3 process, it is available in abundance.

The neutralisation reaction is therefore a three-phase reaction, with ammonia and the slurry. In the Pelchem process, there already is a neutralisation reaction. Evidently it is not effective enough as the ammonium acid fluoride is produced instead of the more desirable ammonium fluoride. This could be the manifestation of the complications of three-phase reactions: mass transfer limitations leading to the requirements of impractical residence times to allow neutralisation to go to completion.

The current neutralisation reactor utilised by Pelchem in the NF_3 process resembles a continuously stirred tank reactor (CSTR). This is bedevilled by high maintenance costs

in part, due to the corrosion of the stirrer and other associated materials of construction. The neutralisation reaction is violently exothermic. Adding more ammonia to drive the neutralisation further towards completion, might lead to a thermal runaway, posing a safety risk. Moreover, corrosion, like any other irreversible reaction is exacerbated by high temperature reactor conditions, hence the further degradation of the stirrer and piping, would be experienced.

To mitigate this, the neutralisation reaction is staggered: rather than effected in one chamber, multiple reaction chambers are used. To limit the exothermic heat, and therefore the reaction temperature, the ammonia is introduced as cold shots in the respective chambers. Figure 4.28 demonstrates the logic for this approach.
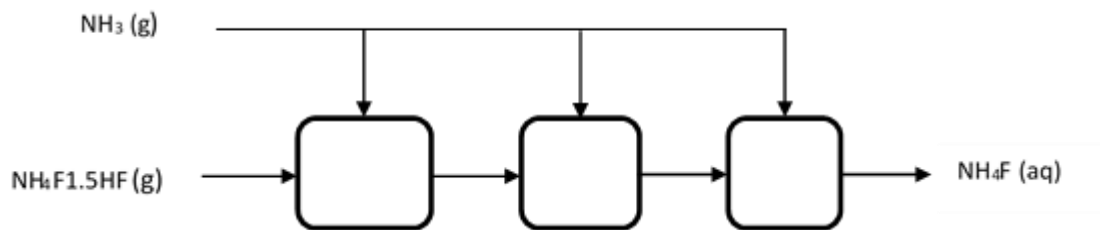
Figure 4.28: Ammonia cold shots to neutralise ammonium acid fluoride slurry to ammonium fluoride.

Cold reactants absorb some of the heat produced by the exothermic reaction, limiting the chances for a thermal runaway. Moreover, this approach also increases the effectiveness of the neutralisation reaction by increasing the conversion. This is due to the introduction of a concentration gradient which is otherwise not present in a single CSTR, but is in multiple CSTRs in series and plug flow reactors (PFR).

For practical considerations, the neutralisation reaction may not necessarily go to completion. Therefore, the recycle of some reagents is essential. Prior to recycle, the separation of the reagents from the product(s) as well as from inert or undesirable by-products, is necessary. In three-phase systems, separations are typically effected by phase separations as this is the most obvious and easiest separation route. This would then be followed by separation within the same phase using differences in a certain physical property e.g. volatility in liquids or density. This formulaic approach is inappropriate for the current case, in that the separations are much more conveniently

done all in one: a unit operation capable of phase separation and solid-solid separation is employed. Figure 4.29 is illustrative of the recycling and separation reasoning.
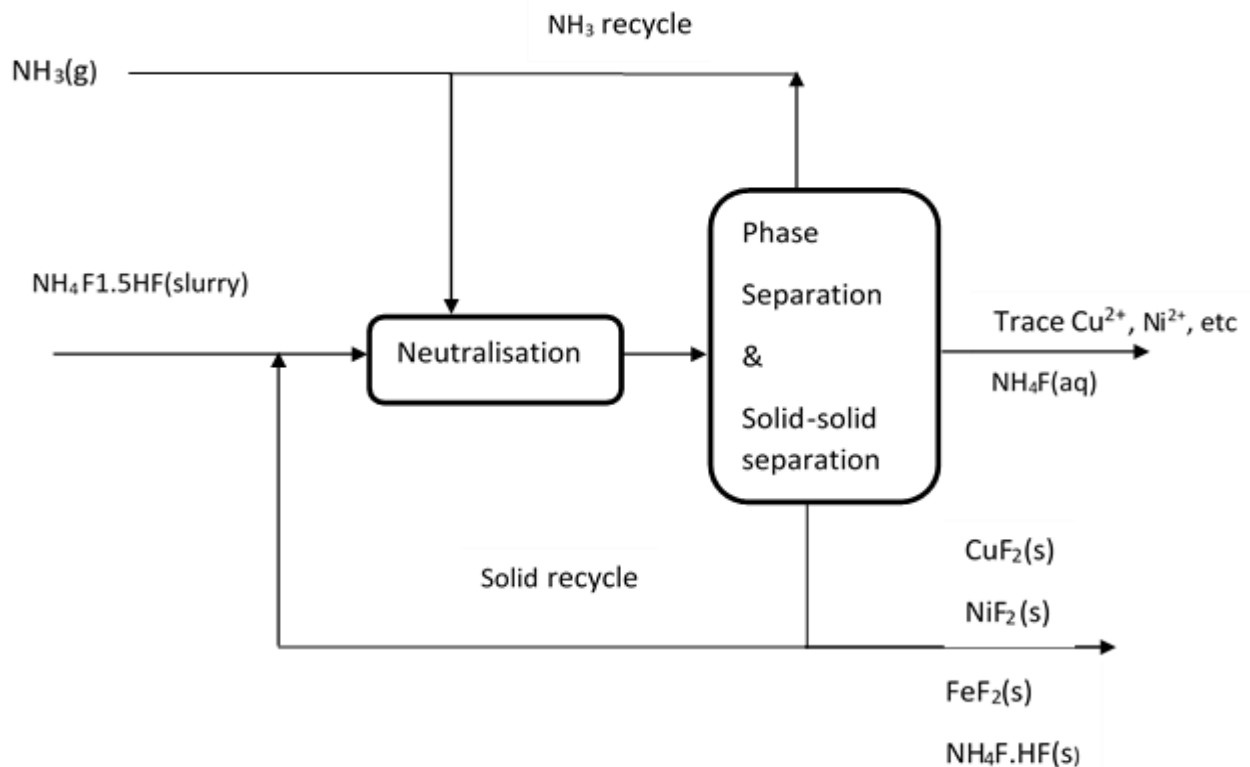
Figure 4.29: Neutralisation and separation sequence. The majority of the metal contaminant is precipitated out and purged.

The solid recycle is predominantly ammonium bifluoride. This is contaminated with the Monel metal fluoride precipitates. Since the path of the metal cations to the ammonium acid fluoride stream, is corrosion, an irreversible redox reaction, a purge stream is used. This is to prevent a build-up of the metal fluoride precipitant potentially clogging the system.

The unit operation capable of solid-solid separation and liquid separation is a spiral concentrator. It utilises a fluid, in this case, the ammonium fluoride solution to transport the solid mixture. Centrifugal force and gravity are used to effect the solid-solid separations: the metal fluoride precipitates all have densities in excess of 4 000 kg/m^3 (4 230 kg/m^3 for CuF_2, 4 720 kg/m^3 for NiF_2 and 4 090 kg/m^3 for FeF_2), whilst the density of ammonium bifluoride is only 1 500 kg/m^3. The heavier components of the solid mixture are driven to the periphery, whilst the lighter component, ammonium

bifluoride, is collected on the inside edge and therefore recycled. Liquid-solid separation can be effected using simple sedimentation.

The trace copper and nickel cations remnant in the ammonium fluoride solution, can be removed using cationic ion exchange resins. This text has demonstrated that Lewatit TP207 is the better than Purolite S930Plus for this purpose. It is therefore the resin of choice in this regard. Industrially, ion exchange resins are used cyclically; where absorption and elution steps are utilised to remove metal cation contaminants from the solution and subsequently, from the resin, respectively. In addition, a backwash step is used to remove the potentially entrained solid impurities in the resin.

In the case of Lewatit TP207, the expansion of the resin during this step, ranges from 50 % to 80 %. The elution involves regeneration of the resin to a useful state i.e. the metal cation contaminant is replaced with protons. Naturally the resin is rinsed with deionised water. The resin is then ready for reuse. This cycle is repeated until the resin expires. In the case of Lewatit TP207, this takes two years, loss of capacity due to aging or even oxidation, ultimately renders the resin useless.

In the process industry, HCl gas is abundant. Hence it is convenient to use it as regenerant of the Lewatit TP207. Moreover, in order to have a streamlined design, the backwash step is combined with the regeneration step such that the metal cation contaminants are removed together with the solid impurities entrained in the resin. Figure 4.30 shows the principles of operation of the resin.


40 % NH_4F HCl, solids, M^{2+} Deionised H_2O

Pure NH_4F HCl(g) H_2O

NH_4F|72
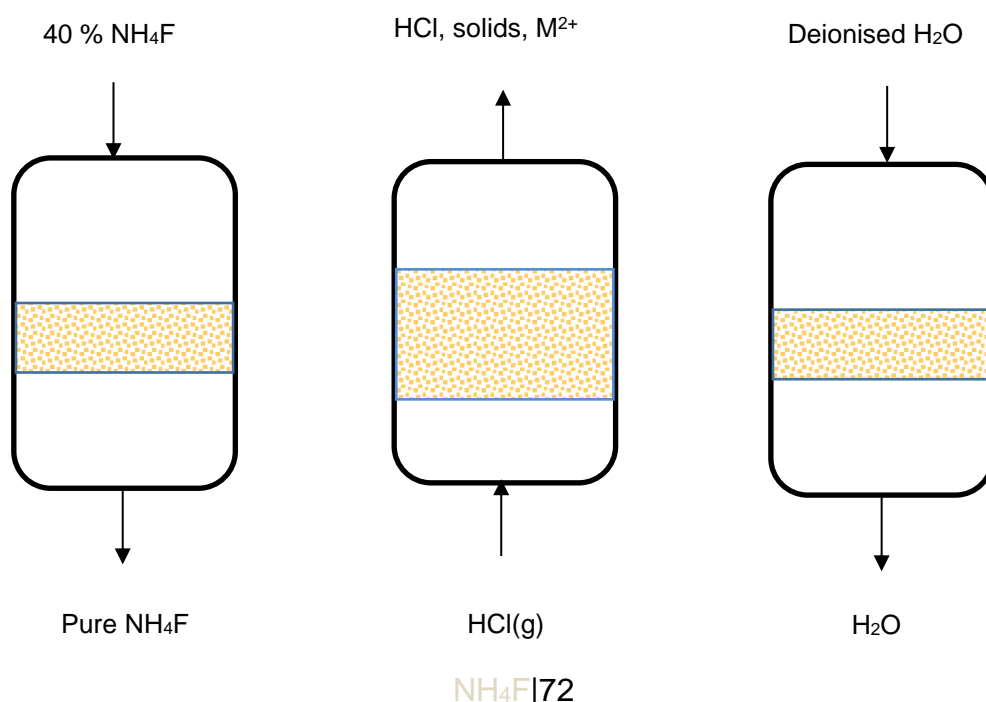
Figure 4.30: Stages during the purification of 40% NH_4F with Lewatit TP207. (a) In service. (b) Backwash and regeneration.

For the purpose of regeneration and backwash, the ion exchange bed is treated as a fluidised bed. Since the particle size of the resin particles is larger than 150 μm, some instability and slugging can be expected. The mitigating factor is that the fluidisation is meant to occur for a short period, not the bulk of the resin bed. The computation of the Archimedes number allows for the utilisation of the Wen and Yu correlation to determine the minimum fluidisation velocity. From equation (2.26):

$$Ar = dp^3 p_f (p_s - p_f) \frac{g}{\mu^2} = 1.263 \times 10^4$$

$$Re_{mf} = (1135.7 + 0.0408 Ar)^{0.5} - 33.7 = 6.9$$

$$\therefore U_{mf} = \frac{\mu Re_{mf}}{dp p_f} = 0.13 \text{ m. s}^{-1}$$

This can be contrasted with the experimentally determined minimum fluidisation value, the experimental value takes precedence.

The maximum allowable velocity as per equation (2.27), is:

$$U_{max} = \left(1.78 \times 10^{-2} \frac{(p_s - p_f)^2}{p_f \mu}\right)^{1/3} d_p = 0.6 \text{ m. s}^{-1}$$

For group B particles in the Geldart classification, the minimum bubbling velocity is the same as the same as the minimum fluidisation velocity. The fluidisation velocity is pegged at 0.3 m.s^{-1}.

For convenience, the resin pellet bed is specified at 1 m^3 and the diameter to height ratio is set at 1:5. Given that the volumetric expansion of the resin is only 80%, more than enough of the transport disengagement height is provided. For a 10 m height of the vessel, the cross sectional area of the bed is 3.14 m^2. The settled bed height of resin pellets is therefore the quotient of the volume and the cross-sectional area: 32 cm. The height at minimum fluidisation is 80 % more than the settled height: 58 cm. Hence the porosity at fluidisation is:

$$\varepsilon_{mf} = 1 - \frac{h_s(1 - \varepsilon_s)}{h_{mf}} = 0.67$$

The diameter of the gas bubble, as per equation (2.29), is:

$$d_{bo} = 0.0037(U - \boldsymbol{U_{mf}})^2 = 1.07 \times 10^{-4} \text{m}$$

$$d_{bm} = 0.652\left[A_c(U - \boldsymbol{U_{mf}})\right]^{0.4} = 0.507 \text{ m}$$

$$\therefore d_b = d_{bm} - (d_{bm} - d_{bo})\exp\left(\frac{-0.3h}{D_t}\right) = 0.042 \text{ m}$$

5 Conclusions and recommendations

The two resins have high selectivity for copper (II) cation. This makes them suitable for the cleaning of ammonium solutions contaminated with Monel cations. The apparent reaction kinetics can be modelled using power law reaction kinetics, wherein the pre-exponential equilibrium constant is 150 for Lewatit TP207 and 75056 for Purolite S930Plus with Cu^{2+}(aq) in a matrix of 40% NH_4F.

The standard heat of reaction in the case of Purolite S930Plus, is -26555 $J \cdot mol^{-1}$, whilst in the case of Lewatit TP207, it is -4 696 $J \cdot mol^{-1}$. For Lewatit TP207, the pre-exponential rate constant is 269 682 $L^2 \cdot min^{-1} \cdot mol^{-2}$, whilst for Purolite S930Plus, it is 2 213 $L^2 \cdot min^{-1} \cdot mol^{-2}$. The activation energies are 24 116 $J \cdot mol^{-1}$ and 14 368 $J \cdot mol^{-1}$ for Lewatit TP207 and Purolite S930Plus, respectively. It was established that the diffusivity also displays a temperature dependency, which was evaluated via pseudo-Arrhenius analysis.

Breakthrough curve modelling is only possible with a high degree of empiricism. Treating breakthrough curves as a characteristic concentration profile in the cases where mass transfer limitations are eliminated, is a more fruitful exercise. In the case of the Lewatit resin, it takes 13 hours per litre of resin, to reach breakthrough if the flowrate is 5 BV/hr and the concentration is 370 ppm of the cations in the ammonium fluoride.

The average contaminant load on the ammonium acid fluoride from the Pelchem NF_3 process, is 197 ppm Fe^{2+}(aq), 5 422 ppm Ni^{2+}(aq) and 5 835 ppm Cu^{2+}(aq). Ammonia is quite effective in reducing these cations in solution. In fact, when the acid fluoride is neutralised, only trace quantities of the metal cations remain. The precipitate formed is predominantly ammonium bifluoride, together with a copper-nickel fluoride hydrate type of compound.

For NF_3 process, the neutralisation reaction of the acid fluoride is a violently exothermic process. To reduce the heat output, cold shots of ammonia gas ought to be used rather than charging all the ammonia at once. Moreover, the storage of the

acid fluoride on steel drums, is to be avoided as the Fe^{2+}(aq) cannot be completely removed by the resins. Instead, a continuous neutralisation process is proposed.

For the separation of the ammonium bifluoride solid from the metal fluoride salts precipitated on neutralisation of the acid fluoride, a spiral concentrator such as Humphrey's spiral concentrator is suggested. In this regard, use of the neutralised ammonium fluoride solution as conduit for the solids on concentrator, is an option worth considering due to its convenience.

Lewatit TP207 is the obvious resin of choice in the purification of the remnant trace metal cation contaminants. The regeneration step can be combined with the backwash step and be treated as a fluidisation process, with hydrogen chloride gas as the fluid of choice. This simplification may decrease the maintenance time significantly, and improve bed throughput.

6 References

Alothman, ZA, Alam, MM and Naushad, M (2013) "Heavy toxic metal ion exchange kinetics: Validation of ion exchange process on composite cation exchanger nylon 6, 6 Zr(IV) phosphate" *Journal of Industrial and Engineering Chemistry*, 19 (2012), 5009-5011.

Amorello, D, Barreca, S, Bruno, M, Milia, A, Orrechio, S and Pettignano, A (2016) "Chemical characterization of ancient liturgical vestment (chasuble) by Inductively Coupled Plasma–Optical Emission Spectrometry (ICP–OES)" *Microchemical Journal*, 129(2016), 305-309.

Bäuerlein, PS, ter Laak, TL, Hofman-Caris, RCHM, de Voogt, P and Proge, STJ (2012) "Removal of charged micropollutants from water by ion exchange polymer- effects of competing electrolytes" *Water Research*, 46 (2012), 5009-5011.

Bauer, G (1965) *Handbook of Preparative Chemistry 2nd edn, vol 2,* Academic Press, New York.

Branken, DJ, Krieg, HM, le Roux, JP and Lachmann, G (2014) "Separation of NF_3 and CF_4 using glassy perfluoropolymer Teflon AF and Hyflon AD60 membranes" *Journal of Membrane Science*, 462 (2014), 75-87.

Chakraboty, P (2012) "Speciation of Co, Cu and Ni in coastal and estuarine sediments: Some fundamental characteristics", *Journal of Geochemical Exploration,* 115 (2012), 13-23.

Chieng, PC (1993) "Method of production of high purity silica and ammonium fluoride", European Patent 0555940A1, assigned to International Minerals & Chemical Corporation, US.

Coulson, JM, Richardson, JF, Backhurst, JR and Harker, JH (1991) *Coulson & Richardson's Chemical Engineering 4th edition,* Volume 2*,* Butterworth Heinemann, Newcastle.

Demirçivi, P, Esen, H, Yıldırım, H, Bozdoğan and Hızal, J (2013) "Preconcentration and Removal of Cu (II) Ions using Diisocyanate Derivatized Ethylene-Vinyl Alcohol Copolymer Ion Exchange Resin" *Ion Exchange Letters*, 6(2013), 12-15.

Deokar, SK and Mandvgne, SA (2015) "Estimation of packed-bed parameters and prediction of breakthrough curves for adsorptive removal of 2,4-dichlorophenoxyacetis acid using rice hush ash" *Journal of Environmental Chemical Engineering,* 3 (2015), 1827-1836.

Everson, RC, Neogamus, HWJP and Kaitano, R (2011) "The random intraparticle model for description of combustion of char particles derived from mineral-and inertinine rich coal" *Fuel,* 90(2011), 2347-2352.

Fernández-Olmo,I, Fernández,JL and Irabien, A (2007) "Purification of dilute hydrofluoric acid by cormmercial ion exchange resins" *Separation and Purification Technology*, 56(2007), 118-125.

Fiori, A and Becker, MW (2015) "Power law breakthrough curve tailing in a fracture: The role of advection" *Journal of Hydrology,* 525(2015), 706-710.

Fiori, A, Volpi, E, Zarlenga, A and Bohling, GC (2015) "Gaussian or non-Gaussian logconductivity distribution at MADE site: what is its impacts on the breakthrough curve?" *Journal of Contaminant hydrology,* 179 (2015), 25-34.

Fleischer, H (2005) "Structural chemistry of complexes of $(n-1)$ d_{10} ns_m metals with β-n-donor substituted thiolate ligands $(m=0, 2)$" *Coordination chemistry reviews,* 249(2005), 799-827.

Fogler, HS (2006) *Elements of Chemical Reaction Engineering 4th edition*, Prentice Hall, New Jersey.

García-Mateos, FJ, Ruiz-Rosas, R, Marquès, MD, Cotoruelo, LM, Rodríguez-Mirasol, J and Cordero, T (2015) "Removal of paracetamol on biomass-derived activated carbon: Modeling the fixed bed breakthrough curves using batch adsorption experiments" *Chemical Engineering Journal,* 279(2015), 18-30.

Gogoi, S, Nath, SK, Bordoloi, S and Dutta, RK (2015) "Fluoride removal from groundwater by limestone treatment in the presence of phosphoric acid" *Journal of Environmental Management*, 152 (2015), 132-139.

Gritti, F and Guichon, G (2014) "The rationale for optimum efficiency of columns packed with new 1.9μ fully porous Titan-C_{18} particles- A detailed investigation of intra-particle diffusivity" *Journal of Chromatography A,* 1355(2014), 164-178.

Gutierrez, HJ (1983) "Preparation of ammonium fluoride", ES 527452, assigned to Derivados del Fluor, Spain.

Hackbarth, F, Girrardi, F, Santos, JC, de Souza, AAU, Boaventura, RAR, de Souza, SMAGU and Vilar, VJP (2015) "Ion exchange breakthrough curves for single and multi-metal systems using marine nacroalgae Pelvetia canaliculata as a natural cation exchanger" *Chemical Engineering Journal,* 269(2015), 359-370.

Harland, CE (1994) *Ion Exchange: Theory and Practice 2nd Edition,* Royal Society of Chemistry, Letchworth.

He, X, Azarian, MH and Pecht, MG (2014) "Analysis of the Kinetics of Electrochemical Migration on Printed Circuit Boards Using Nernst-Planck Transport Equation" *Electrochimica Acta,* 142(2014), 1-10.

Helfferich,FG (1962) *Ion Exchange*, Mcgraw-Hill, New York.

Husa'kova', L, Šrămkoṽa,J, Cernohorskỷ,T and Bařinova',M (2007) "Ammonium fluoride as a novel chemical modifier for elimination of magnesium chloride interference on the determination of lead by graphite furnace atomic absorption spectrometry", *Talanta,* 72 (2007), 1400-1403.

Jon, H, Lu, B, Oumi, Y, Itabashi, K and Sano, T (2005) "Synthesis and thermal stability of beta zeolite using ammonium fluoride", *Micromeso,* 89 (2005), 88-95.

Kantor, T, Bezúr, Pungor, E and Winefordner, JD (1983) "Volatilization studies of magnesium compounds by a graphite furnace and flame combined atomic absorption method. The use of a halogenating atmosphere", *Spectrochimica Acta,* 4 (38B), 581-607.

Katoh, M, Kimura, M, Sugino, M, Horikawa, T, Nakagawa, K and Sugiyama, S (2015) "Modification of commercial NaY zeolite to give high water diffusivity and absorb a large amount of water", *Journal of colloid and Interface science,* 455(2015), 220-225.

Krabbenhøft, K and Krabbenhøft, J (2008) "Application of the Poisson-Nernst-Planck equations to the migration test", *Cement and Concrete Research,* 38 (2008), 77-88.

Kurniawan, TA, Chan, GYS, Lo, W and Babel, S (2006) "Physico-chemical treatment techniques for wastewater laden with heavy metals" *Chemical Engineering Journal,* 118 (2006), 83-98.

Lafond, E, Cau Dit Coumes, C, Gaufinet, S, Chartier, D, Le Bescop, P, Stefan, L and Nonat, A(2015) "Investigation of the swelling behaviour of cationic exchange resins saturated with Na^+ ions in a C_3S paste", *Cement and Concrete Research,* 69 (2015), 61-71.

Leinekugel-le-Cocq, D, Tayakout-Fayolle, M, Le Gorrec, Y and Jallut, C (2007) "A double linear driving force approximation for non-isothermal mass transfer modelling through bi-disperse adsorbents" *Chemical Engineering Science,* 62 (2007), 4040-4053.

Liu, W and Xu, H (2015) "A complete analysis of classical Poisson-Nernst-Planck model for ionic flow" *J. Differential Equations*, 258(2015), 1192-1228.

Markets and Markets 2017, Ion Exchange Market by Type, accessed 30 March 2017 http://www.marketsandmarkets.com/search.asp?search=ion+exchange

Ohji, H and French, PJ (1999) "Single step electrochemical etching in ammonium fluoride" *Sensors and Actuators*, 74 (1999), 109-112.

Patton, A, Crittenden, BD and Perera, SP (2004) "Use of the linear driving force approximation to guide design of monolithic adsorbents" *Chemical Engineering Research and Design* 82(A8), 999-1009.

Perry, RH and Green, DW (1997) *Perry's Chemical Engineers' Handbook 7th edition*, McGraw-Hill, New York.

Purkayastha, D, Mishra, U and Biswas, S (2014) "A comprehensive review on Cd(II) removal from aqueous solution" *Journal of water Process Engineering,* 2(2014), 105-128.

Rhodes, M (2008) *Introduction to Particle Technology 2nd edition*, Wiley, West Sussex.

Russo, V, Tesser, R, Trifluoggi, M, Giogni, M and Di Serio, M (2015) "A dynamic intraparticle model for fluid-solid adsorption kinetics" *Computers and Chemical Engineering,* 74(2015), 66-74.

Saito, N, Youda, S, Hayashi, K, Sugimura, H and Takai, O (2003) "Chemical resistivity of self-assembled monolayer covalently attached to silicon substrate to hydrofluoric acid and ammonium fluoride" *Surface Science,* 532-535(2003), 970-975.

Scheider, S, Weis, W, Beyl,V and Niederprum (1976) "Process for the production of ammonium fluoride from fluosilicic acid", US patent 4026997, assigned to Bayer Aktiengesellschaft, US.

Seider, WD, Seader, JD and Lewin, DR (2004) *Product & Process Design Principles 2nd edition,* Wiley, New York.

Simate, GS, Iyuke, SE, Ndlovu, S, Heydenrych, M and Walubita, LF (2012) "Human health effects of residual carbon nanotube and traditional chemicals in drinking water" *Enviroment International,* 39(2012), 38-49.

Singh, A, Allen-King, RM and Rabideu, AJ (2014) "Groundwater transport modelling with nonlinear sorption and intraparticle diffusion" *Advances in Water Resources,* 70(2014), 12-23.

Skoog, DA, Holler, FJ and Nieman, TA (1998) *Principles of Instrumental Analysis*, Saunders College Pub., Orlando.

Stefan, DS and Meghea, I (2014) "Mechanisms of simultaneous removal of Ca^{2+}, Ni^{2+}, Pb^{2+} and Al^{3+} ions from aqueous solutions using Purolite® S930 ion exchange resin " *C.R. Chimie*, (2014), http://dx.doi.org/10.1016/.

Trujillo, EM, Spinti, M and Zhuang, H (1995) *Ion Exchange Technology: Advances in Polution control*, Technomic Publishing Co. inc, Basel.

Valverde, JL, De Lucas, A, Carmona, M, Gonzålez, M and Rodríguez, JF (2005) "Model for the determination of diffusion coefficients of hecterovalent ions in macroporous ion exchange resins by zero-length column method" *Chemical Engineering Science,* 60 (2005), 5836-5844.

Wang, J and Wan, Z (2015) "Treatment and disposal of spent radioactive ion-exchange resins produced in the nuclear industry" *Progress in Nuclear Energy*, 78 (2015), 47-55.

Young Kim, T, Su An, S, Geun Shim, W, Wook Lee, J, Young Cho and Hwan Kim (2015) "Adsorption and energetic heterogeneity properties of cesium ions on ion exchange resins" *Journal of Industrial and Engineering Chemistry*, 27 (2015), 260-267.

Zhan, J and Zhou,L (2012) "Method for producing electronic grade aqueous ammonium fluoride solution", China Patent 20120145949, assigned to Shangai Huayi Microelectronic materi

Appendices

A.1 Inductively coupled plasma-optical emission spectroscopy / mass spectrometry

Inductively coupled plasma-optical emission spectroscopy (ICP-OES) is perhaps one of the handiest analytical tools in the market. It is robust to chemical interferences as well as elemental interactions. Furthermore, it is capable of low detection levels of concentrations. Using a high-frequency field, with an inert noble gas, often argon, the ICP source produces a plasma. This is effectively a high energy ionised gas.

At temperatures in the upper 10 000 K, a sample may be dissolved, dissociated as well as atomised. This has an effect of excitation of elements in the sample. The relaxation thereof, results in emission of characteristic frequencies for the elements (Amorello *et al*, 2016).

The light (which is proportional to the concentration in the sample) is measured using an emission spectrometer. It separates the characteristic frequencies into the corresponding wavelengths and therefore, identifying the elements. Figure A.1 shows the instrumental outline of the ICP-OES (Wang & Wan, 2015).

The ICP source produces emission spectra traits of the elements present in samples. Ideally the traits of an excitation source are such that reproducibility in the excitation condition is maintained. Sufficient line intensity for detection limits is achieved. This is helped in part, by low spectral background. ICP is but one of the available excitation sources. Others include flames, DC arcs, DC plasma, etc.

In a plasma, a noteworthy quantity of the atoms and/or molecules are ionised. A time-varying magnetic field causes a plasma to be inductively coupled. Thus, the current flows are induced in the ionised medium, resulting in resistive heating of the plasma gas, enabling it to be self-sustaining: the hot plasma ionises the incoming non-ionised gas on a continuous basis.

To produce a plasma, a water-cooled induction coil is connected to a radio frequency
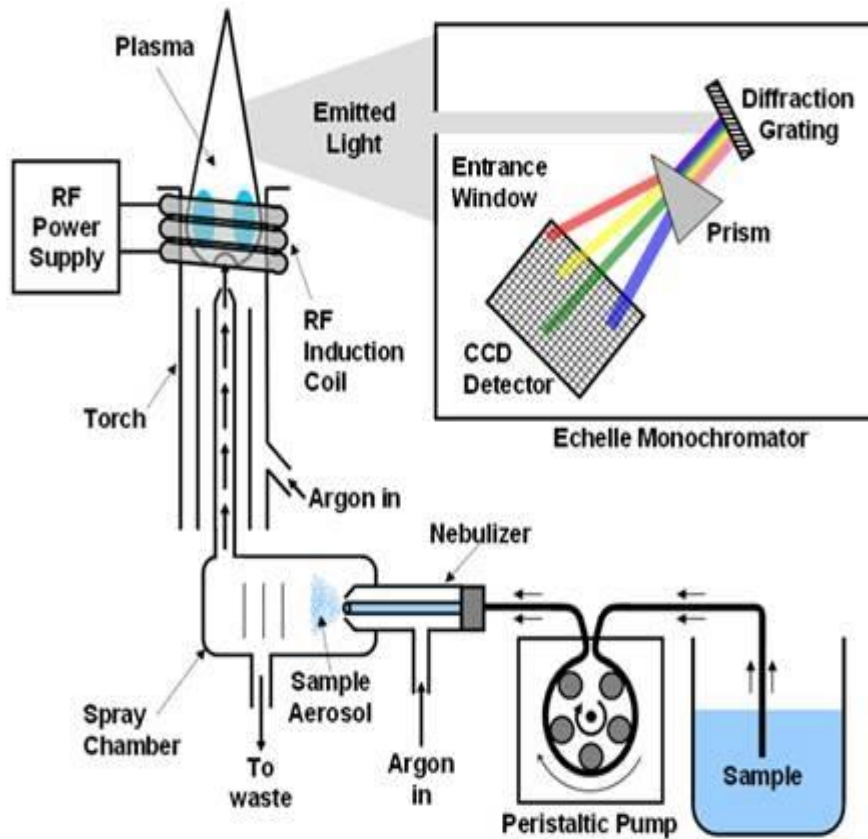

Figure A.1: ICP-OES outline.

generator inducing, a strong high-frequency magnetic field in a small volume flushed with inert noble gas. Figure A.2 illustrates this. Subsequently, the inert gas is exposed to a high-voltage Tesla discharge; igniting the plasma by nucleating electrons and other ions (Wang & Wan, 2015).

These electrons accelerate and collide with the inert gas atoms, generating a great deal of heat and more ions. A vortex flow of the inert gas cools the inside walls of the torch thus, stabilising the plasma. The high temperature and residence time of the sample allows for the complete vaporisation of the sample solvent and the breakdown of the analyte into atoms prone to excitation (Amorello *et al*, 2016).

b
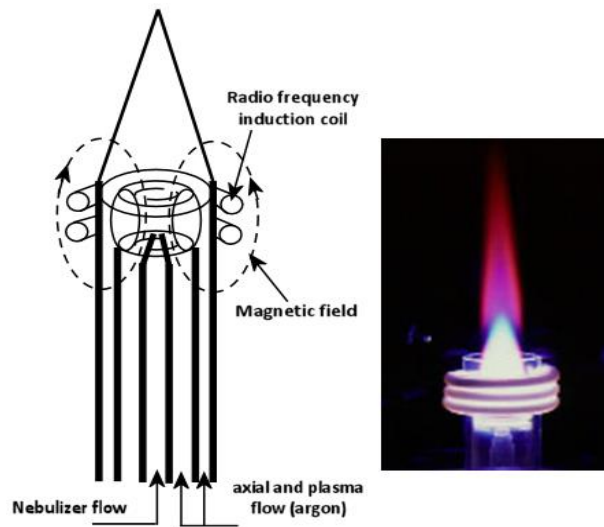
Figure A.2: ICP torch framework.

A spectrometer can isolate light from the various wavelengths corresponding to emission lines of the different analyte elements, differentiate this light from the plasma background emission. To improve resolution, a grating, a fine slit as well as an imaging system is used. On one hand, a monochromator can measure only one wavelength at a time. Thus, multi-element analysis can only be done sequentially. On the other hand, a polychromator has a secondary slit permanently fixed at each of the chosen analysis lines (Wang & Wan, 2015).

The ICP part of the machine, is the mechanism through which a sample is introduced to the plasma. The sample is inserted to the nebulizer where a piezo-electric crystal is contacted, resulting in the sample being turned to an aerosol. The argon gas can transport the resulting aerosol to the capillary injection tube. Argon in the plasma form sweeps up sample in the capillary injection tube, some of the argon gas serves as coolant. Radio frequency coils in the range of megahertz, form the plasma (Amorello, *et al*, 2016).

Nebulisation is used to introduce liquid samples. In this regard, pneumatic nebulisers are popular. Samples are fed into the nebuliser by a pump resulting in a Venturi-effect. Subsequently the sample solution is split into droplets due to the high-speed gas flow creating an aerosol. Since only a small fraction is nebulised, a great deal of the sample

c

is wasted. The larger droplets in the aerosol are removed in the spray chamber (Wang & Wan, 2015).

A.2 Standard addition method for concentration analysis

Typically, the unknown variable in analytical chemistry, is the analyte's concentration, C_x. A much more concentrated version of the analyte with a predetermined concentration, is prepared: the stock solution (C_s). A constant amount of the analyte, V_x is added to a series of equal volumetric flasks, with a volume of V_t. In addition, gradually increasing amounts of the stock solution are added to the volumetric flasks, except for one of the volumetric flasks. The flasks are then filled up to their graduated capacity with water.

The flasks are then analysed, the instrument whether it be the ICP-OES or any other concentration analysis instrument, will give a response, S. This is directly proportional to the analyte concentration, C_a, in question i.e.

$$S = K_{SAM} C_a \qquad (A.1)$$

K_{SAM} is the proportionality constant. The molarity or concentration is the ratio of the number of moles, n_a and total volume of the flask:

$$C_a = {n_a}/{V_t} \qquad (A.2)$$

In the flasks, the analyte originates from the unknown as well as the standard:

$$n_a = C_s V_s + C_x V_x \qquad (A.3)$$

Therefore:

$$S = K_{SAM} C_a = K_{SAM} \left({n_a}/{V_t}\right)$$
$$= K_{SAM} \frac{C_s V_s + C_x V_x}{V_t} = \frac{K_{SAM} C_s V_s}{V_t} + \frac{K_{SAM} C_x V_x}{V_t} \qquad (A.4)$$

This is analogous to a straight line, y = mx + b, where y = S, x = V_s, b = $\frac{K_{SAM} C_x V_x}{V_t}$ and

d

$m = \frac{K_{SAM}C_s}{V_t}$ .The concentration of the unknown may be determined by mathematical manipulation, wherein the ratio of the intercept and slope gives:

$$\frac{b}{m} = \frac{K_{SAM}C_xV_x}{V_t} \Bigg/ \frac{K_{SAM}C_s}{V_t} = \frac{C_xV_x}{C_s}$$

rearranging and solving for the unknown:

$$C_x = \frac{bC_s}{mV_x}.$$

A.3 X-ray diffraction analysis

Diffraction is heavily dependent on the availability of a periodic arrangement of radiation sources. For an example a diffraction grating is a periodic arrangement of slits. Each slit acts like a source of radiation. This emanates from Huygen's principle which states that every point on a wave front acts as a new source. If the slits have the same dimensions on each side, a periodic two-dimensional pattern is observed, otherwise a one-dimensional arrangement pattern is apparent (Katoh *et al,* 2015).

Figure A.3 depicts the situation when diffraction is considered on a diffraction grating.

For the triangle depicted on the figure, consider the resolution of the diffracted ray to its abscissa and ordinate components around the angle θ. In an analogous fashion to deviation angle in prisms, θ is the emergence angle, dd is the distance between slits and n represents the repetition of the spectrum. The hypotenuse on the triangle is equal to the grating spacing, dd. The interference is constructive if the wavelengths, nλ are integer multiples of the radiation wavelength (λ) i.e. the repetition of the spectrum, n = 1, 2, 3…

e
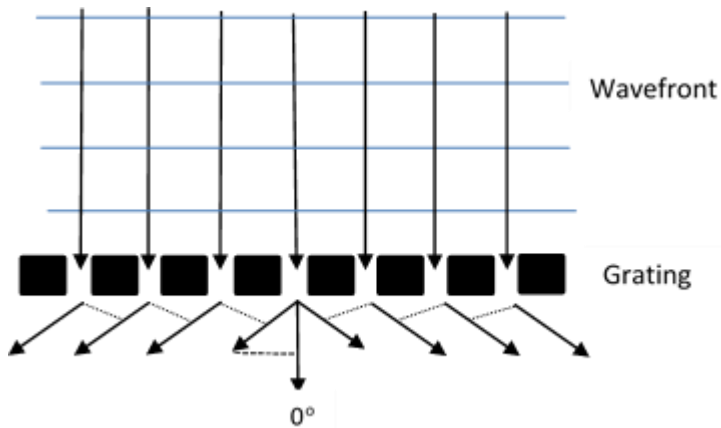
Figure A.3: Interaction of radiation with a
diffraction grating.

Using trigonometric manipulation, the wavelengths can be written in terms of grating spacing:

$$n\lambda = \mathrm{ddsin}\theta \qquad \text{(A.5)}$$

Therefore:

$$\theta \sim \frac{\lambda}{\mathrm{dd}} \qquad \text{(A.6)}$$

Hence, mathematically, the wavelength of light to be used should be the same order of magnitude as the diffraction grating spacing. The distribution of molecules and atoms in a crystalline solid has a periodic arrangement. This periodic arrangement of atoms/molecules could act as a form of diffraction grating. In the case of crystalline solids, the equivalent to the diffraction grating spacing is the interatomic spacing, which is in the order of magnitude of angstroms.

Figure A.4 shows a schematic diagram of the distribution of atoms/molecules inside a crystalline solid. Each atom/molecule acts like a coherent source of radiation. A situation where there is diffraction is considered: superposition of the wavelengths results in a pattern.

Intuitively, for diffraction to occur, the radiation rays must collide with the walls/sides of the diffracting medium at regular intervals. Hence the spacing in the medium must roughly be of the same order of magnitude as the wavelength of the radiation. In the case of crystalline solids, interatomic spacing is typically in the order of magnitude of

f
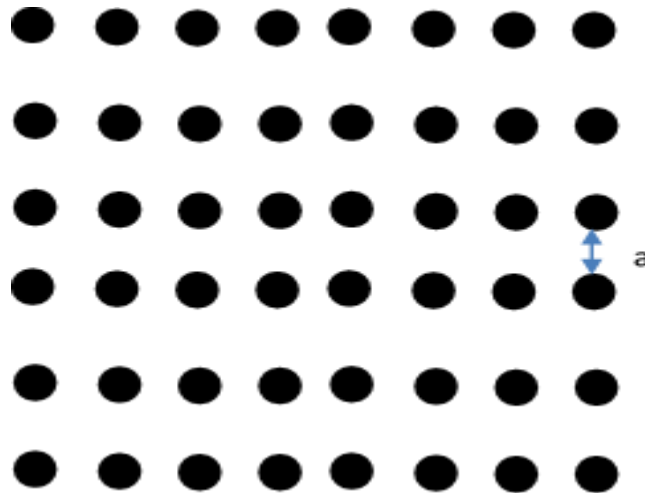
Figure A.4: Distribution of atoms/molecules in a
crystalline solid. The interatomic spacing in a unit cell
is denoted by the symbol a.

angstroms, therefore the wavelength of radiation also should be in the same order of magnitude. This explains the use of X-rays; they are in the order of magnitude of angstroms.

X-rays as all electromagnetic wave, is an oscillating electric field. Perpendicular to the electric field, is the magnetic field. When an electric field is incident on an atom, it affects the nucleus as well as the electrons on that atom. The nucleus is much heavier than the electrons. Acceleration due to the electric field, $\vec{a}$ is directly proportional to the electric field, $\vec{E}$ and inversely proportional to the mass, m with proportionality constant of electric charge, e:

$$\vec{a} = \frac{e}{m}\vec{E}. \tag{A.7}$$

Dividing by a small number is mathematically the same as multiplying by a big number, hence the acceleration of the nucleus on account of the electric field, pales in comparison to that of the electrons, such that it is reasonable to exclude it in the analysis of the effect of an electric field on an atom. Although the acceleration of the electrons is relatively more significant, they remain bounded to the nucleus. Their response to the force applied by the electric field of the x-rays, can be modelled as a simple harmonic oscillation of a spring. The external force on this spring has the

g

frequency of the x-ray radiation. Hence the oscillation will be the same as the frequency of the x-rays i.e. the electrons have the same frequency as the x-rays.

When an electron oscillates, it emits electro-magnetic radiation at various directions, which is at the same frequency. This is a hallmark of dipole radiation. Each atom acts like a source at the same frequency, as the x-ray, which are coherent. The phenomenon whereby an incident ray occurring in one direction is scattered in various directions, is known as Thompson scattering.

To determine the intensity pattern in different directions, the radiation from the periodic arrangement of sources is summed. Unlike in the case of diffraction due to a diffraction grating caused by slits, three dimensional sources are involved as opposed to just one. Bragg posited a simpler way of evaluating the three-dimensional situation: consider the scattering due to the atoms in terms of planes. Figure A. 5 shows Bragg's approximation.

The wave reflected at the first plane is at a phase difference to the wave reflected at the second plane and so on. This phase difference corresponds to the path differences. The condition for all of them to be on the same phase is:

$$2dd\sin\theta = n\lambda \qquad\qquad\text{(A.8)}$$

Analogously to diffraction grating, dd is the distance between planes. This is known as Bragg's law. $2dd\sin\theta$ is the path difference between the waves refracted from 2 consecutive planes. If the path difference is an integer multiple of the wavelength, the waves will be in phase. This is the condition for some maxima. Although a myriad of planes is possible, for brevity, one set of planes was chosen.

h
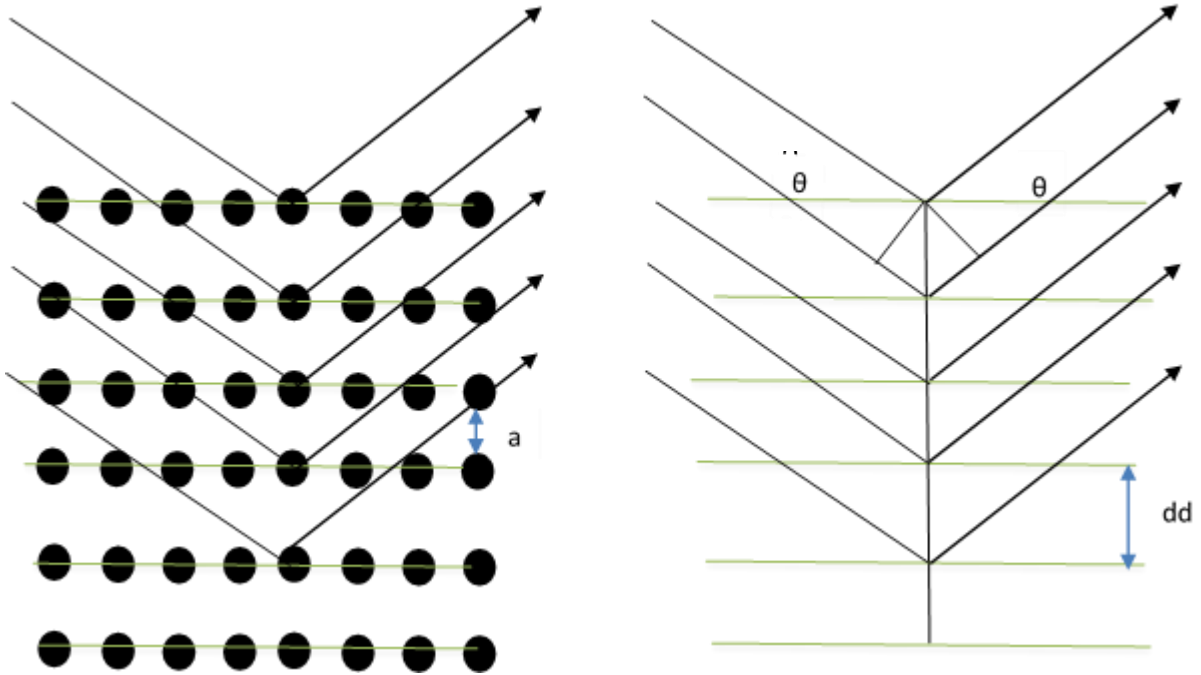
Figure A. 5: Bragg's approximation of 3-dimensional scattering of x-rays using planes. Ө is the grazing angle.

Miller indices are used to label the planes; typically they are represented as (h,k,l), where the letters refer to the intercepts with the x, y and z axis, respectively. If only planes parallel to the x-axis are chosen, the miller indices are (h,k,l) = (1,0,0). If the planes are chosen such that they only intersect the y axis, the miller indices are (h,k,l) = (0,1,0). If the intersection occurs on two out of the three axis, the miller indices are (h,k,l) = (1,1,0).

A crucial parameter in Miller indices, is the interplanar spacing. In the case of planes depicted on Figure A. 5, the interplanar spacing is identical to the interatomic spacing in a unit cell. This only ever true if only one of the miller indices is nonzero. In the general case, the interplanar spacing is the quotient of the interatomic spacing and the square root of the sum of the squares of the miller indices:

$$dd = \frac{a}{\sqrt{h^2 + k^2 + l^2}}.$$

(A.9)

i

X-ray diffraction is very useful in determining the structure of materials. An x-ray diffractometer is used for this purpose. Figure A.6 illustrates the operation of such a device.
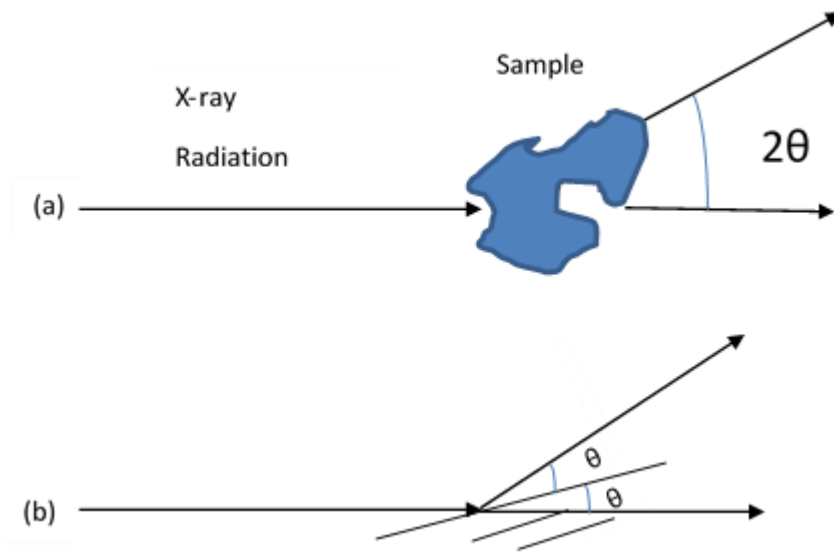

Figure A.6: Principle of operating in an x-ray diffractometer. (a) Sample. (b) Grazing angle with planes modelled as diffraction grating.

The sample can consist of either a single crystal or alternatively, many crystals. This naturally leads to the scattering of x-rays in all directions. The intensity of the scattered x-rays will vary with the direction. The diffractometer is equipped with a device that measures the intensity of the scattered x-ray as a function of the direction.

As can be seen on Figure A.6 (b), the angle of the scattered x-ray with reference to the incident x-ray, is twice the grazing angle. Mathematically, the smallest angle (2θ) between the scattered direction and incident direction, resulting in maxima i.e. satisfying Bragg's law, corresponds to miller indices where only one intercept is nonzero.

 In Bragg's law, the only variables are the order of the maxima n, and/or the value of the interplanar spacing, dd. There are many possible planes that can be drawn to represent a unit cell in crystal. These directly affect the miller indices, which from equation (e), affect dd.

j

The maxima could be 1st order, 2nd order, etc. The zeroth order maxima is in correspondence with the direction of the incident radiation, because θ = 0 in its case. The intensity of the higher order (n =2, 3…) maxima is much smaller than the intensity of the 1st order maxima. Hence generally the interpretation of xrd data is usually limited to the first order maxima i.e. n = 1:

$$2dd\sin\theta = \lambda$$
$$\therefore \sin\theta = \frac{\lambda}{dd}$$

(A.10)

The maximum value of the interplanar spacing is the interatomic spacing, a lattice constant. This is mathematically verifiable by considering equation (e) and the possible miller indices. On equation (f), when dd is smaller the RHS of the equation becomes bigger, therefore the LHS has to be bigger as well. This means that the angle θ, is bigger. The converse of this situation is necessarily true as well. The physical implication of this mathematical consequence, is that the smallest angle arises from the largest value of dd and the converse is true. This is the basis of the analysis of xrd data.

k